2005-04-27

Plasma Potential Measurements in a Colloid Thruster Plume

Thomas Robert Roy
Worcester Polytechnic Institute

i Abstract

Colloid thrusters are under consideration for NASA missions such as the Laser Interferometer Space Antenna (LISA), which requires the continuous cancellation of external disturbances (approximately 25 microNewtons over a 3-10 year mission). Emissive probes are one diagnostic for the measurement of plasma potential, which can provide valuable information on the level of space-charge neutralization in a thruster plume. Understanding how to achieve effective space-charge neutralization of the positive-droplet thruster plume is important for efficient operation and to minimize the risk of contamination. In this Thesis we describe a laboratory electrospray (colloid) source and accompanying power processing electronics developed for testing of diagnostics in colloid thruster plumes. We present results of an initial series of emissive probe measurements using floating probe and swept bias probe techniques. These measurements were carried out using a single needle emitter operating on a mixture of EMI-IM (an ionic liquid) and tributyl phosphate. For a spray operating at a discharge voltage and current of 2.0kV and 200nA respectively, a potential of 5.0V was measured using the floating probe technique with the probe located at a distance of 2.7cm from the electrospray source. The interpretation of this floating potential as the plasma potential is discussed. In a separate set of tests, we used the swept bias emissive probe technique at the same distance and measured a plasma potential of 2.0V at a discharge voltage of 2.0kV. The discharge current in this latter test was somewhat unstable and varied from approximately 250 nA to over 1000nA. Numerical integration of the Poisson equation was performed to better understand space charge limitations of a probe emitting into a low density plasma. These results are presented and some implications for the

measurements discussed. While the electrospray droplet number density was not measured, calculations to estimate this number density are also presented. Based on these estimates and our numerical calculations, the “knee” in the current voltage characteristic measured using the swept probe technique is estimated to be within 1.3 V of the actual plasma potential.

ii Acknowledgements

This work is part of an ongoing effort to characterize colloid thrusters for very exciting applications in “drag-free” satellite initiatives such as LISA. Much of the pioneering work in this field has been done by Manuel Gamero and Vlad Hruby at Busek Co, Inc. For their continuing support to Professor Blandino and me in our efforts to build up an experimental colloid facility from scratch at WPI, I owe a great deal of thanks. And more recently, great appreciation goes to Vlad for showing faith in allowing me to continue to explore this and related research full time at Busek.

Professor John Blandino has shown me much about the experimental process and has raised the bar of excellence in putting forth honest and useful work to the scientific community. For being patient and supportive in all my efforts, as well as teaching me how to be a better engineer, I owe him much. To the members—past and present—in both the computational and the experimental labs--Adrian Wheelock, Anton Spirkin, Jurg Zwhalen, Andrew Syriyali, Robert Sartoreli, Ryan Chamberlin and Jimmy Partridge—thanks for being there to make my WPI graduate experience a lot more than math and physics. Thanks to the ME staff—Barbara Edilberti, Barbara Furhman, Janice Dresser and Pam St. Louis for adding the touch of family in what can often be the overwhelming world of graduate school. And to the folks of Kilroy and Disc, I thank you for letting me play in your unique, brilliant world of irreverent humor. Thanks to the Committee members for contributions to the final stages of the development of this thesis.

I gratefully acknowledge the support of the WPI Mechanical Engineering department, in particular the contributions of Jim Johnston, Matt Shea, Travis Schrift and Matt Leland.

To my parents, Robert and Nancy Roy, for their continued faith in all of my pursuits, and to my twin sister Jennifer Roy for always being my best friend, I owe much. And finally to Bonniejean Boettcher for her continued love and support during these years and hopefully many more we can share in the future.

iii List of Tables and Figures

iv Nomenclature

A	space charge density of emitted electrons at wire surface relative to ion charge density (dimensionless)
Ac	calculated area of electrospray plume for a given axial distance, assuming a 30° half-angle
B	wire temperature relative to the plasma electron temperature (dimensionless)
C	normalization constant (dimensionless)
D_D	diameter of droplet (m)
e	electron charge (coul)
k	Boltzmann constant (J/K)
K	conductivity (Si/m)
L	length of path traveled by a droplet during time of flight measurement (m)
m_1	mass of a single main droplet (kg)
m_2	mass of a single satellite droplet (kg)
$\dot{m}_1$	mass flowrate of main droplets (kg/m^3)
$\dot{m}_2$	mass flowrate of satellite droplets (kg/m^3)
$\dot{m}_{tot}$	total mass flowrate of all droplets (kg/m^3)
n_1	main droplet number density (#/m^3)
n_2	satellite droplet number density (#/m^3)
n_o	ion number density (#/m^3)
q_r	Rayleigh limit (coul)
q_m	droplet charge (coul)
r_o	emitting wire radius (m)
t_f	time of flight (s)
T_e	temperature of electrons in plasma (K)
T_w	temperature of wire (K)
V_{acc}	acceleration voltage (V)
V_B	breakup voltage (V)
V_n	needle voltage (V)
V_s	stopping potential (V)
v_B	velocity at breakup point (m/s)
ε_o	permitivity of free space (coul^2/N-m$^{2)}$
γ	surface tension (N/m)
ρ_o	ion charge density (coul/m^3)
ρ_{ow}	space charge density of emitted electrons at wire surface (coul/m^3)
θ	radial distance relative to wire radius (dimensionless)
ξ	normalized potential relative to the emitting wire's surface (dimensionless)

ξ_p	normalized plasma potential (dimensionless)
CNT	Carbon Nanotube
ESA	European Space Agency
LISA	Laser Interferometry Space Antenna
MAXIM	Micro-Arcsecond X-Ray Imaging Mission
NIST	National Insititute of Standards and Technology
NASA	National Aeronautics Space Administration
PPU	Power Processing Unit
WPI	Worcester Polytechnic Institute

1. Introduction

1.1 Colloid Thrusters

The theory and operation of colloid thrusters have been described in the literature[1,2]. Much of the recent work with colloid thrusters has been performed at Busek Inc. (Natick, MA) which is currently under contract with NASA to develop a colloid thruster system for flight validation on the NASA ST7 mission which will fly on the European Space Agency's (ESA) SMART-2 spacecraft scheduled for launch in 2008.

The colloid thruster relies on the same process that has been used in electrosprays to produce streams of electrically charged droplets of a conducting liquid. Much of the current understanding of electrospray physics results from research in the use of electrosprays for mass spectroscopy of biological molecules. The electrospray consists of a needle, one end of which is connected to a conducting fluid reservoir, the other end of which is placed a precise distance from an electrode (referred to as the extractor electrode). In the presence of a potential difference, the magnitude of which will depend on the flowrate and liquid properties, the meniscus of the fluid will be confined to a single conical tip first theoretically explained by G.I. Taylor. From this cone, a jet is formed which breaks up as a result of fluid instabilities forming a stream of charged droplets[3]. These droplets can then be accelerated electrostatically by the electric field between the electrodes.

A brief review of the basic physics and scaling laws of colloid thruster operation is important to understand its operational modes and the key variables involved in

predicting their behavior. Much of this work has been summarized by M.Gamero[4] and others[3].

The emitted current of the colloid beam (I_B) and droplet diameter (D_D) of charged droplets emitted from an electrospray of moderate conductivity (K~1S/m) have been studied in detail by de la Mora, Chen and others[5,6,7.8]. Fernández de la Mora[5] reports the scaling laws for I_B and average D_D as:

$$I_B = f(\varepsilon)\left(\frac{QK\gamma}{\varepsilon}\right)^{\frac{1}{2}} \qquad [1.1]$$

$$\langle D_D \rangle = g(\varepsilon)\left(\frac{Q\varepsilon\varepsilon_o}{K}\right)^{\frac{1}{3}} \qquad [1.2]$$

where Q is the volumetric flowrate, ε is the dielectric constant, γ is the surface tension of the propellant and ε_o is the permittivity of free space. The functions $f(\varepsilon)$ and $g(\varepsilon)$ are dimensionless quantities that are determined experimentally and are a result of the particular colloid thruster and experimental conditions. Also experimentally determined is the minimum volumetric flowrate to result in a stable cone-jet:

$$\frac{\rho Q_{\min} K}{\gamma \varepsilon_o \varepsilon} \sim 1 \qquad [1.3]$$

where ρ is the propellant density. Using charge conservation and mass conservation, Gamero[4] uses these relations to calculate the average specific charge:

$$\left\langle \frac{q}{m} \right\rangle = \frac{I}{\rho Q} \sim \frac{f(\varepsilon)}{\rho}\sqrt{\frac{K\gamma}{Q\varepsilon}} \qquad [1.4]$$

Using Equation 1.3 Q is eliminated to yield

$$\left\langle \frac{q}{m} \right\rangle \sim \frac{f(\varepsilon)K}{\varepsilon}\sqrt{\frac{\rho}{\varepsilon_o}} \qquad [1.5]$$

Equation 1.5 demonstrates the dependence of specific charge on the propellant conductivity. The specific charge is an important characteristic of an electrospray, as it can be used to calculate the thrust and specific impulse of a stable cone-jet:

$$T \sim \sqrt{2V_A \rho f(\varepsilon)}\left(\frac{K\gamma Q^3}{\varepsilon}\right)^{\frac{1}{3}} \qquad [1.6]$$

$$I_{SP} = \frac{T}{\dot{m}g} \sim \frac{1}{g}\sqrt{\frac{2V_A f(\varepsilon)}{\rho}}\left(\frac{K\gamma}{Q\varepsilon}\right)^{\frac{1}{4}} \qquad [1.7]$$

where V_A is the acceleration voltage and g is gravitational acceleration. Using the range of flowrates that result in a stable cone-jet (Equation 1.3), the specific impulse can be shown to be proportional to the conductivity ($I_{SP} \sim K^{1/2}$). As such, a target I_{SP} can be obtained with lower accelerating potential. This allows one to avoid the operational and safety hazards of extremely large electrostatic potentials. These scaling relations have been very important to colloid thruster development in recent years, as they have enabled researchers to more effectively predict operational parameters (e.g. accelerating potential, flowrate) and propellant characteristics (e.g. conductivity, density) which will result in an effective balance of thrust and specific impulse.

For a particular propellant, several operational modes may be observed depending on net potential difference between needle and extractor and flowrate: dripping mode, cone-jet and highly stressed. The dripping mode occurs when the flowrate is too large and/or the potential difference is too small to create a field strong enough to create a stable cone. This results in most or all of the propellant dripping out of the needle.

Multiple emission sites, as well as an increase in ion emission, are also possible under certain conditions[3], but this "highly stressed regime" is not characteristic of stable, single Taylor cone emission. Although a purely ionic emission has its benefits (such as an increased Isp) it also will typically result in a lower thrust because the charge-to-mass ratio drops (Equations 1.4-1.7). The single Taylor cone emission is of particular relevance to the Laser Interferometer Space Antenna (LISA) mission, as well as this research, because it is stable, relatively well understood, and for many propellants it represents a favorable combination of efficiency and thrust.

The other major feature that distinguishes a colloid thruster from a conventional electrospray is the need for a neutralizer. Given a positive accelerating potential, the spacecraft emits a plume with a net positive charge (with respect to spacecraft ground), resulting in a buildup of a net negative charge the spacecraft. This would result in an electrostatic attraction of the emitted plume to the spacecraft. Spacecraft instrumentation, solar arrays and the thruster itself could be coated with the spent propellant which could degrade power system performance (e.g. less light would get through a covered solar array) or damage the spacecraft (some colloid propellants such as EMI-Im or EMI-BF_4 are known to react with stainless steel over time). As such a cathode neutralizer that emits electrons into the plume would prevent the spacecraft from building up any significant electrostatic charge.

In atmosphere or low earth orbit, there exist ample ambient particles to neutralize the spray. In an earth-trailing, heliocentric orbit as the proposed for the LISA mission (section 1.2), there is no ambient neutralization available. As such, neutralization of the spray is a critical to the operation of the colloid thruster. In turn, understanding the plasma potential of such an electrospray is crucial in understanding how best to effectively neutralize the colloid thruster plume, and this is the subject of this research.

1.2 Drag Free Missions

Colloid thrusters are currently under consideration for use on NASA missions requiring micro-Newton level thrust. Missions under consideration include astrophysical observatories such as the LISA for the detection of gravitational waves[9]. The mission involves three identical satellites in the formation of an equilateral triangle with relative separation of 5 million kilometers, orbiting the sun at L1 (Figure 1.1a). The objective of the mission is to use laser interferometery to measure changes in the separation between a test mass in the center of each satellite with a resolution on the order of nanometers. Several micro-Newton thrusters would operate continuously over the 5 to 10 year life of the mission to cancel the disturbance from solar radiation pressure in order to allow only the presence of gravity waves to change the position of the test masses (Figure 1.1b)[10].

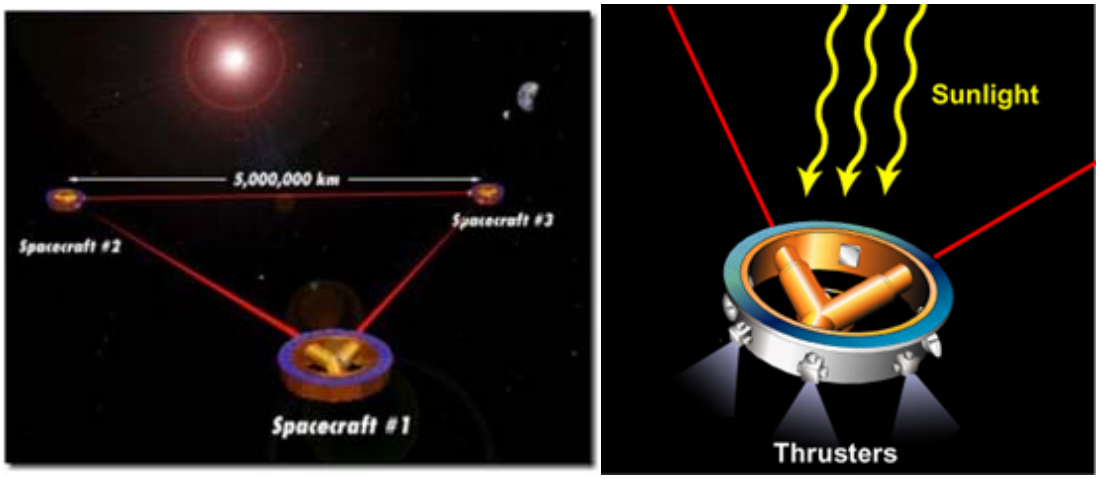

(a) (b)

Figure 1.1: (a) artist's conception of the LISA spacecraft in operation at L1. (b) micro-Newton thrusters must counteract solar pressure continuously.

An alternative thruster technology that is under consideration for the LISA Mission is the Field Emission Electric Propulsion (FEEP) thruster. Versions of this thruster operating with cesium and indium propellants have been developed in Europe over the last decade. In a FEEP system, a liquid metal in vacuum is exposed to a strong electric field, resulting in the formation of small protrusions along the liquid metal surface. As the radii of the curvature of the tips decreases, the local field strength increases until it reaches approximately 10^9 V/m, at which point the atoms in the tip ionize and are accelerated via the electric field[9]. The FEEP plume may be effectively neutralized by field emission array (FEA) cathodes[11,12]. Micro-Newton thrusters such as colloid and FEEP present unique challenges to their study in the laboratory, primarily as a result of their inherently low thrust and beam current[9].

LISA is just one of several "Drag Free" missions under consideration within NASA's Office of Space Science. Another example of precision interferometery is the Micro-Arcsecond X-Ray Imaging Mission (MAXIM), a proposed NASA X-ray observatory

with the mission goal of achieving 100 nanoarcsecond resolution, which would allow scientists an unprecedented look at high energy (i.e. X-ray-producing) events in the universe such as black holes[13]. This would be accomplished by flying a fleet of up to 33 optics spacecraft in formation with a precision of 20 nanometers, followed 500 kilometers by a detector spacecraft. The formation-keeping thrusters (six degrees of freedom) would be required to produce approximately 0.3μN to 20mN of translational (+/- x, y, z) thrust and minimum impulse bits of 20μN·s for attitude control (+/- roll, pitch and yaw)[14].

1.3 Motivation

In any electrostatic thruster, space charge in the plume can affect the beam divergence as well as the level of electron and ion/droplet current emission for a given accelerating potential. Given the extreme precision, durability and longevity required of station-keeping thrusters for missions like LISA, excessive build-up of space charge is unacceptable and must be neutralized if colloid thrusters are to be considered a viable candidate. Complete spacecraft neutralization involves both the removal of excess negative charge on the spacecraft as well as control of the space charge in the plume, and it is the latter case that is the primary focus of this work.

To effectively neutralize a plume, it is essential to understand the physical characteristics and charge distribution within the plume. For example, a highly dense plume, or plasma, would require significantly more current from a neutralizing cathode than a diffuse plume. The plume divergence may also impact the operating parameters (which control the energy of the emitted electrons) of the neutralizing cathodes as well as their number

and placement. Plasma potential measurements provide a high fidelity means of assessing the space charge within the plume. Such measurements can be obtained using standard emissive probe techniques[15,5,11,17] and have in fact been used to study the plasma potential in indium FEEP thruster plumes[12].

An emissive probe consists of a thermionically emitting filament in which the floating potential is closely related to the local plasma potential. Mapping of the plasma potential provides information on the effectiveness of the space-charge neutralization process as well as the structure of axial and radial electric fields within the plume, which can be compared with simulation results.

Because micro-Newton thrusters operate with such a low beam current (at least three orders of magnitude less than ion or Hall thrusters), space-charge effects are not sufficient to preclude ion emission even without a neutralizer[18]. Therefore, the neutralizer is required only for overall current neutralization to prevent spacecraft charging. If operation is in LEO or in a laboratory vacuum chamber, sufficient electrons exist either from the ambient plasma or from secondary electron emission from tank walls to enable operation without a neutralizer even for overall charge control. For an earth-trailing trajectory such as that of LISA, a neutralizer will be required to maintain overall neutrality as well as to minimize the possibility of beam divergence due to space-charge (although this effect may be minimal).

Because micro-Newton thrusters can be operated without a neutralizer in the laboratory, the measurement of plasma potential provides a critical insight into the performance sensitivity to changes in neutralizer position and/or operating parameters. Particle simulation is used to aid interpretation of the data, and guide further testing.

1.4 Review of Plasma Potential Measurement Experiments with Emissive Probes

The goal of this research is to measure the plasma potential of a colloid electrospray, and emissive probes are used to provide a means of measurement. When the probe is more positive than the plasma, most of the emitted electrons will have insufficient energy to escape the potential well and are reflected back; conversely, when the probe is more negative than the plasma, the electrons can escape into the plasma.

The use of a floating, strongly emitting probe[16] is a proven technique used to characterize the plumes of similar thrusters[11], and it is convenient to implement. As a result of the increase in heater power to a thermionically-emitting filament, more electrons are emitted causing the probe potential to float more positive until electrons no longer have enough energy to escape the potential well and the probe floating potential will reach with a steady state value near the plasma potential. If the plasma density is too low, the emission will be space charge limited and not enough electrons will be emitted to allow the probe potential to float up to the plasma potential.

The goal of this research is to measure the plasma potential in the colloid plume of an electrospray, and the emissive probe is used to provide the means of measurement. Emissive probes rely on thermionic emission of electrons from a fine tungsten wire that is

heated, and an interpretation of their current-voltage characteristic to determine the plasma potential. When the probe potential is higher than (more positive) the surrounding plasma, the emitted electrons will be reflected back into the probe (probe current is unchanged); a potential lower (more negative) than the plasma will allow the electrons to escape, resulting in measurable change in current from the probe. Whether the current is negative or positive depends on the sign convention adopted[15, 17].

Kemp and Sellen[16] discuss several techniques that can be used to make precise plasma potential measurements with the emissive probe. One technique, the floating, strongly emitting probe, provides a direct measurement of the plasma potential, and it is more convenient a technique to implement (no data reduction or step by step measurements). It is implemented by eliminating the probe bias supply and increasing the heater power to make the filament increasingly emissive while recording the probe potential. The floating potential just above the knee in a characteristic curve indicates the plasma potential (Figure 1.2).

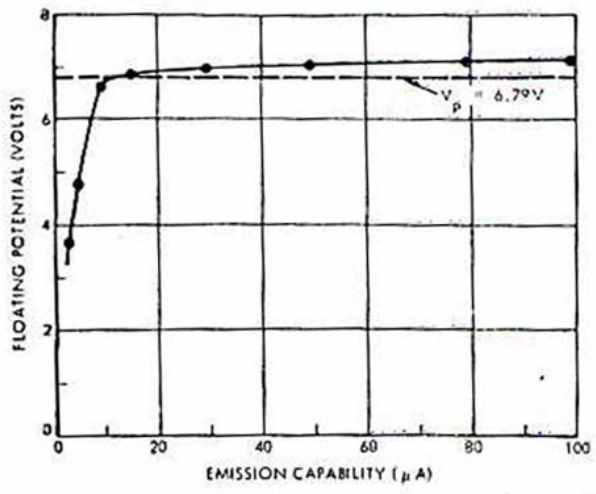

Figure 1.2: Emissive probe floating potential vs. emission limited current as originally reported by Kemp and Sellen[16].

Another technique, which we refer to as the voltage sweep technique, is to vary the probe potential while measuring the current through the probe circuit to ground. A semi log plot of this I-V characteristic should reveal two straight lines corresponding to nearly constant electron emission below the plasma potential and an exponentially decreasing electron current (Maxwell-Boltzmann cutoff) above the plasma potential. The intersection (or 'knee') of these two lines should correspond to the plasma potential (Figure 1.3)

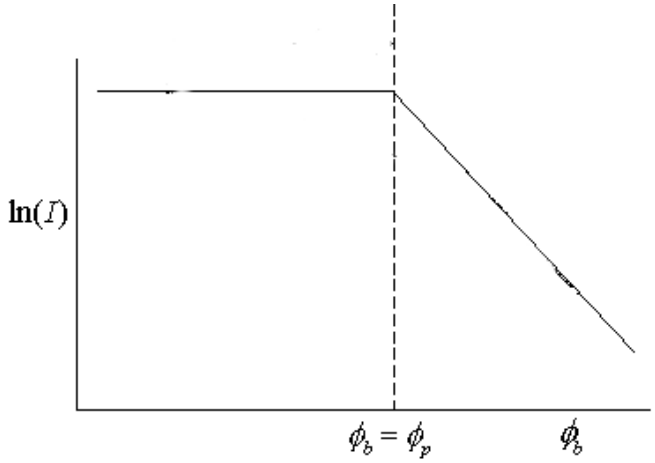

Figure 1.3: Sketch of a voltage sweep technique characteristic curve of the current drawn by the emissive probe plotted against the probe bias potential.

Emissive probes show this sharp knee in the I-V characteristic in plasma densities approximately 10^7 to 10^{10} ions-cm^{-3}. In lower densities, the knee becomes less sharp as space charge effects dominate in high-emission/low-ambient density environments (Figure 1.4).

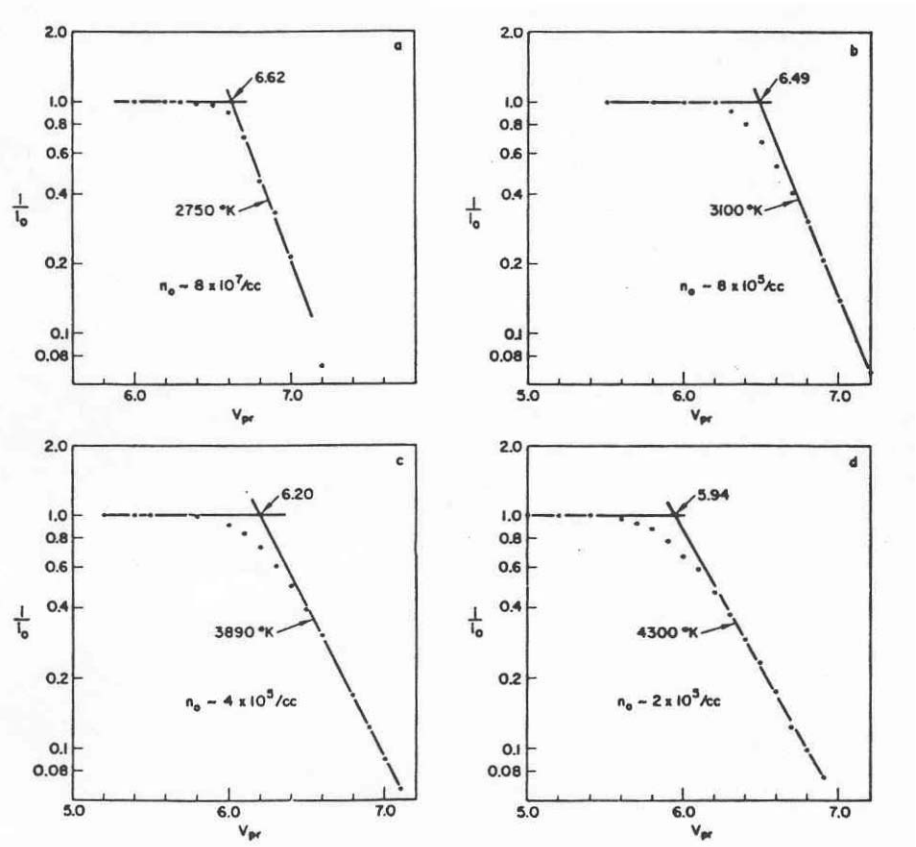

Figure 1.4. Emissive probe characteristics with increased rounding of the knee as the surrounding plasma density is reduced, originally reported by Kemp and Sellen[16].

Schuss and Parker[19] also discuss emissive probe behavior in this space-charge-limited regime† and their results, in combination with the analytical model developed by Kemp and Sellen[16], are used to interpret the results (Chapter 4) of the two emissive probe techniques described above. When the electrons emitted from an emitting probe enter the surrounding plasma, some electrons will have sufficient energy to escape the potential well and into the plasma, and other electrons will not have sufficient energy to escape into the plasma. The distance from the emitting surface at which this potential 'cutoff' occurs is dependant upon the probe radius, the number of electrons emitted (electron

† The Schuss and Parker model assumes a long (ignore end effects) cylindrical probe is immersed in a plasma with no magnetic field. The plasma electron distribution is Maxwellian where the plasma electron energy is much larger than the plasma ion energy..

current), the electron energy or temperature (T_e) and the density of the surrounding plasma (n_o). For example, Schuss and Parker find that the number of electrons (current) that can be emitted into the surrounding plasma scales with the plasma density (by holding electron temperature and probe potential constant) as $n_o^{1/2}$. This relationship is valid over five orders of magnitude of plasma density ($n=10^7 cm^{-3}$ through $10^{11} cm^{-3}$). They also find that, close to the probe's surface (say, less than 10 wire radii), the electron space charge dominates so strongly (by electrons that do not have sufficient energy to escape into the surrounding plasma), that an emitting probe in plasma behaves the same as a simple vacuum diode (or vacuum cathode) with the anode a approximately 1.9 Debye lengths away (Figure 1.5)

.

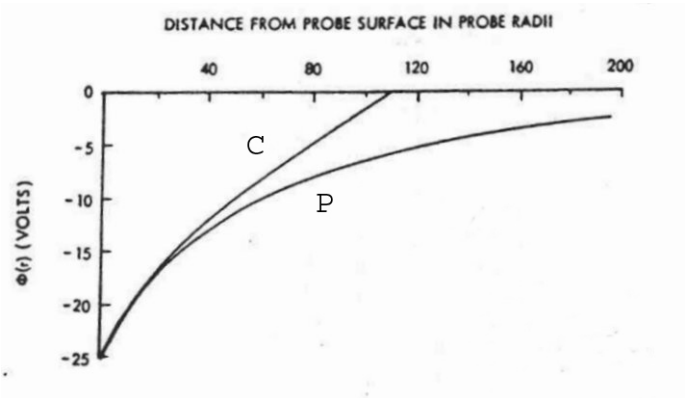

Figure 1.5: A computer solution from Schuss and Parker[16] of $\phi_{(r)}$ vs. r for an emissive probe operating space charge limited regime in a plasma (P) and in a vacuum (C).

Incorporating the distance of this virtual cathode ($1.9\lambda_D$) into their solution for the potential near the probe surface (electron space charge dominated), Schuss and Parker find the plasma Debye length (λ_D) is proportional to the ratio of electron temperature to plasma density (T_e/n_o), meaning that if two of the quantities are known, the third can be determined.

C. Mareese-Reading et al.[11] used a tungsten emissive probe (0.075mm dia, ~4mm length) to measure the plasma potential in the ion beam of an Indium FEEP thruster, so as to characterize the effectiveness of three different neutralizer cathodes. To determine the heater power required to float the probe to plasma potential, many V-I traces were taken by varying the probe bias voltage and monitoring the probe current at both axial extremes: close to the extractor (3mm) and farthest to the target (60mm). Once sufficient filament currents were identified, the strongly emitting floating probe technique was used to measure the plasma potential—the potential roughly occurs at the knee in the trace (e.g. Figure 1.3)—at different distances along the plume. The experimental results were in fair agreement with numerical predictions. When the probe was in close proximity (<5mm) to the thruster, some of the probe's emitted electrons were collected by the ion emitter tip (interpreted as additional ion current being emitted from the thruster). Because the thruster was operated in constant current mode, the thruster power supply was incorrectly compensating for additional ion emission from the thruster.

2. Experimental Setup, Diagnostics & Procedures

In this Chapter we present a description of the experimental apparatus and test configurations employed in this work, as well as the procedures for conducting each test.

2.1 Experimental Setup and Facilities

The facility and apparatus used for these tests consisted primarily of the vacuum system, emissive probe, probe positioning system, electrospray source, field emission cathode neutralizer, power processing unit (PPU) and data acquisition system. These are described in the following paragraphs.

2.1.1 Vacuum System

The probe measurements were performed in an 18-inch diameter, 30-inch tall stainless steel vacuum chamber. This chamber is equipped with a 6-inch diffusion pump backed by a 17 cfm mechanical pump as well as a liquid nitrogen baffle. The system is capable of an ultimate pressure in the low 10^{-6} Torr range. During measurements the pressure was approximately 3 x 10^{-5} Torr. The vacuum chamber rests on a stainless steel collar along which are mounted flanges with various electrical feedthroughs. The vacuum facility can be seen in Figure 2.1.Visible in this Figure is the chamber, diffusion pump, PPU, and camera setup from an early configuration.

Figure 2.1: Vacuum facility.

2.1.2 Probe Positioning System

A compact, two degree-of-freedom (r,θ) probe positioning system specifically designed for this chamber was used. The positioning system uses two stepper motors and is controlled through LabVIEW. Further details about the program and the rest of the system can be found in the report of the MQP under which this was developed[20].

The positioning system moves an aluminum rail along a track in the radial (r) direction. A probe support bracket can be mounted at different positions along the track, depending on the experimental configuration. The probe leads are fed through the bottom of the bracket to a BNC feedthrough on the collar of the chamber. A beam target, which consists of an aluminum foil coated metal plate measuring 12" x 12", is also mounted at varying positions on the track, depending on the experimental configuration (Figure 2.2).

Measurement of beam current incident on the target provides independent confirmation (independent of the PPU) that the beam is on during operation.

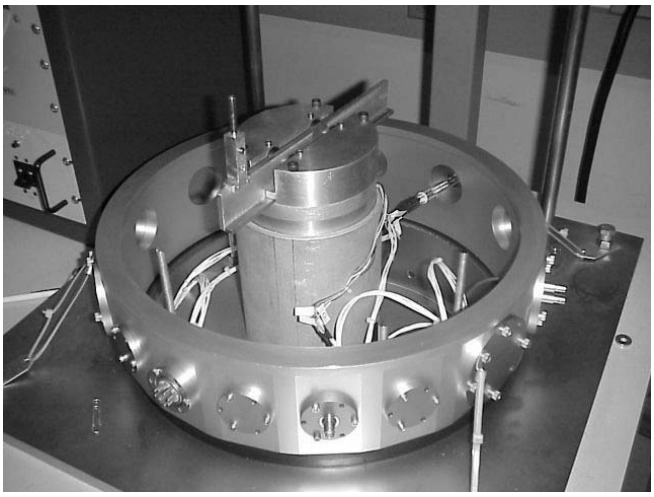

Figure 2.2: Two degree-of-freedom (r,θ) probe positioning system (target not shown).

2.1.3 Electrospray Source

The colloid thruster consists of two parts: a colloid emitter or electrospray, and a neutralizer. The electrospray consisted of a needle and an extractor electrode. In the mode of operation used in this work, the electrospray emits positively charged droplets (and possibly ions as well). A complete thruster such as would be used on a spacecraft also includes a neutralizer. In this work, a Busek-manufactured carbon nanotube field emission cathode neutralizer was used (Section 2.1.4).

The electrospray is shown in Figure 2.3, which shows the primary components. A Delrin adaptor flange (mounted to a QF-50 flange on the chamber wall) provides electrical isolation and mechanical stability. The needle runs along a center hole (1/16" diameter). The pressurized side of the flange (exposed to atmosphere) features a modified capillary

connector (Upchurch Scientific) that provides a vacuum seal, allowing the propellant reservoir to be stored outside the vacuum chamber. The vacuum side (in the chamber) secures the emitting end of the needle. The needle is centered with a Delrin disk with a hole in the center. Quarter-inch nylon standoffs (mounted by #2-56 screws) separate the needle feedthrough from the extractor electrode.

Two Delrin adaptors were constructed for these tests: Adaptor 1 (long) and Adaptor 2 (short). The long adaptor is designed to extend beyond the mounting flange into the chamber, allowing for (a) small distance (0.33cm) from the probe and (b) the ability to mount the carbon nanotube (CNT) neutralizer cathode to directly to the electrospray. The long adaptor is fitted with an electrical isolation shield for the CNT cathode neutralizer (to prevent shorting between the grounded extractor and the cathode). The long adaptor can be seen in Figure 2.4. Detailed drawings of Adaptor 1, Adaptor 2, the extractor, needle feedthrough, and cathode shield can be found in Appendix A.

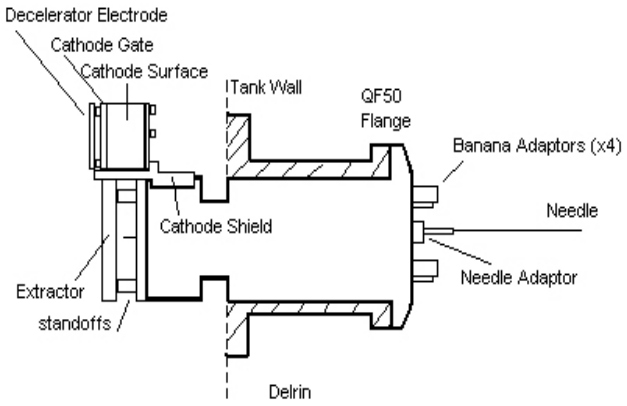

Figure 2.3: Diagram (not to scale) of Adaptor 1

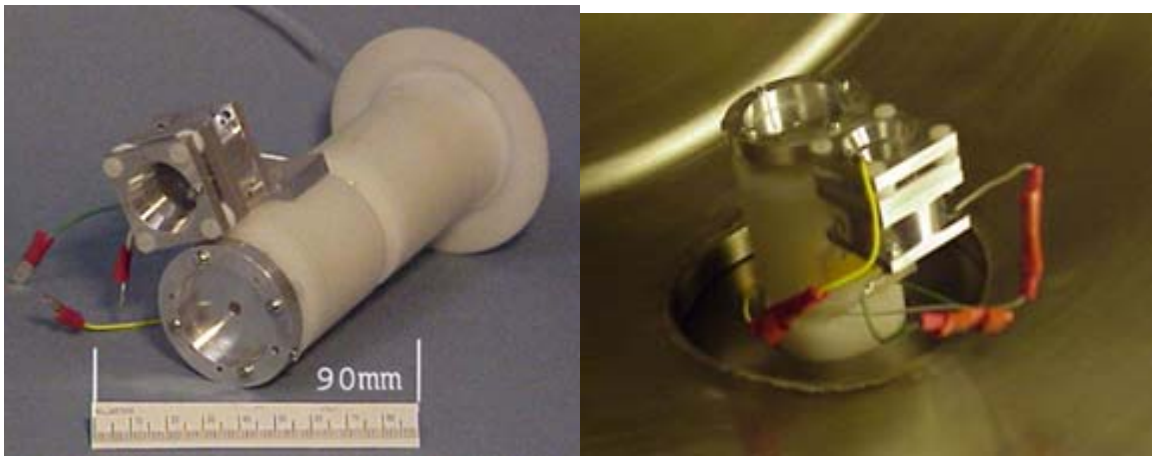

Figure 2.4: Images of Adaptor 1 with neutralizer assembly. The left photo is the electrospray with mounted CNT cathode; the photo at right is a view of the thruster from within the chamber.

Adaptor 2 was made using a shorter length of Delrin, also designed to mount on a QF50 cross flange which in turn is mounted on the vacuum chamber (windows are mounted on the other two ports in the cross to view glass flanges to enable viewing). The electrospray was imaged using a high-resolution monochrome Pulnix-1325 camera connected to an IMAQ PCI-1428 image capture board. Magnification of the electrospray was accomplished with a Meiji UNIMAC Macrozoom lens (0.7 – 4.5 X).

The extractor electrode is mounted 0.64cm from the emitting end of the needle. The needle is electrically connected to the PPU via an alligator clip, while the rest of the components are connected via o-ring-sealed banana adaptors. Adaptor 1 features four electrical feedthroughs: one for the emitter (extractor) and three for the cathode neutralizer (CNT surface, the gate, and the decelerator electrode). As there is no space for the cathode to attach near the emission site when the QF-50 cross is used (to allow visualization), the cathode was not used at all in that configuration and there is only a need for one electrical feedthrough in Adaptor 2, for the extractor.

The needle emitter is a 24” (60.96cm), Type 304 stainless steel tube with 0.009” (230µm) OD and 0.004” (100 µm) ID. The end of the needle is faced off using a modified lathe (at Busek) and chamfered to aid in the formation of a stable electrospray cone-jet (Figure 2.5). Other materials commonly used in electrospray emission studies are silica capillaries as well as platinum needles. Stainless steel was chosen for its relatively low cost, durability, and conductivity (allowing a convenient means by which to apply power to the needle outside the vacuum tank). Stainless steel is known to corrode when used in an electrospray with ionic liquid propellants, and therefore does not last as long as the relatively chemically neutral Platinum or silica capillaries. Platinum, however, is expensive and not very durable. Silica also does not corrode as much as stainless steel in an electrospray, but it is not conducting, and therefore requires coating to supply power. Given the short-time duration of these experiments, in addition to considerations of cost and durability, stainless steel was chosen.

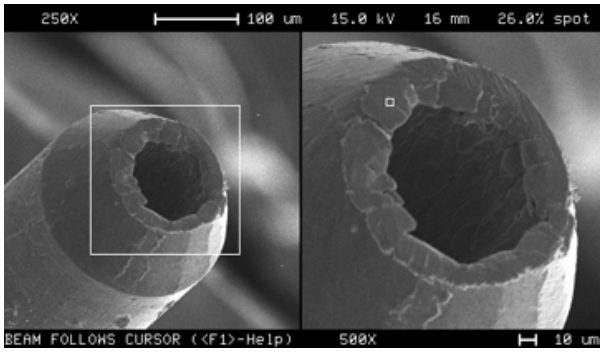

Figure 2.5: SEM image of needle emitter (250x on left, 500x on right) showing 60° chamfer edge, taken at Busek.

The propellant is fed directly to the needle from a small, sealed Pyrex reservoir external to the tank. A stainless steel tee (Upchurch) feeds the needle into the reservoir as well as connects to a gas-vacuum line (for pressurizing the reservoir). An Upchurch Silica

Sealtight Kit is used form a gas-tight seal around the needle, which is fed through the tee into the reservoir.

The propellant used was 2.9% (by weight) ionic liquid "EMI-Im" 1-ethyl-3-methylimidazolium bis (trifluormethylsulfonyl)imide ($C_8H_{11}F_6N_3O_4S_2$) in a solution of Tributyl Phosphate ($C_{12}H_{27}O_4P$), or "TBP". This was chosen for its low vapor pressure (4.3 milliTorr at 20°C)[2], and low viscosity. Electrosprays formed from highly viscous liquids like glycerol are poorly understood, in that they exhibit a mixed ion-droplet electrospray usually characteristic of more highly conductive propellants. Little is known about the physical mechanisms governing the breakup into an electrospray[18]. Also, glycerol's viscosity is highly temperature-dependant and strict temperature control is required to prevent erratic flowrate variations, and therefore current and thrust variations[18]. The conductivity of pure TBP, as well as TBP mixed with salts, is too low (dielectric constant of 8.9 at 25°C)[2] to achieve the desired thrust efficiency of interest for colloid thrusters[2]. In combination with the ionic liquid EMI-Im, the electrical conductivity of a TBP based solution is on the order of $2x10^{-2}$ (Si/m), and produces a sufficiently energetic spray at reasonable accelerating voltages and efficiency[2,18]. EMI-Im solutions have been extensively studied[2,18,21,22,23], and their properties and behavior are relatively well understood compared to other ionic liquid solutions. Pure EMI-Im, although typically possessing a conductivity two orders of magnitude higher[2,18] was prohibitively expensive for these tests. Also, there is published data available for the 2.9% mixture[18], allowing us to compare findings. Further, the purpose of this work was to characterize the plasma potential, so the propellant only needs to be sufficiently conductive to form a cone-jet.

The conductivity of our solution was determined to be 1.55 x 10^{-2} K (Si/m), obtained by measuring the resistance across a column of the solution in a silica capillary tube. By measuring the resistance across a fluid column of known length and cross sectional area, the conductivity can be determined. In the course of the work, the propellant reservoir was contaminated with a backflow of pump oil and a new batch had to be mixed. The new propellant mixture had a conductivity of 1.32 x 10^{-2} K (this value is used for all work after 10/7/03, which includes all cases except FP1).

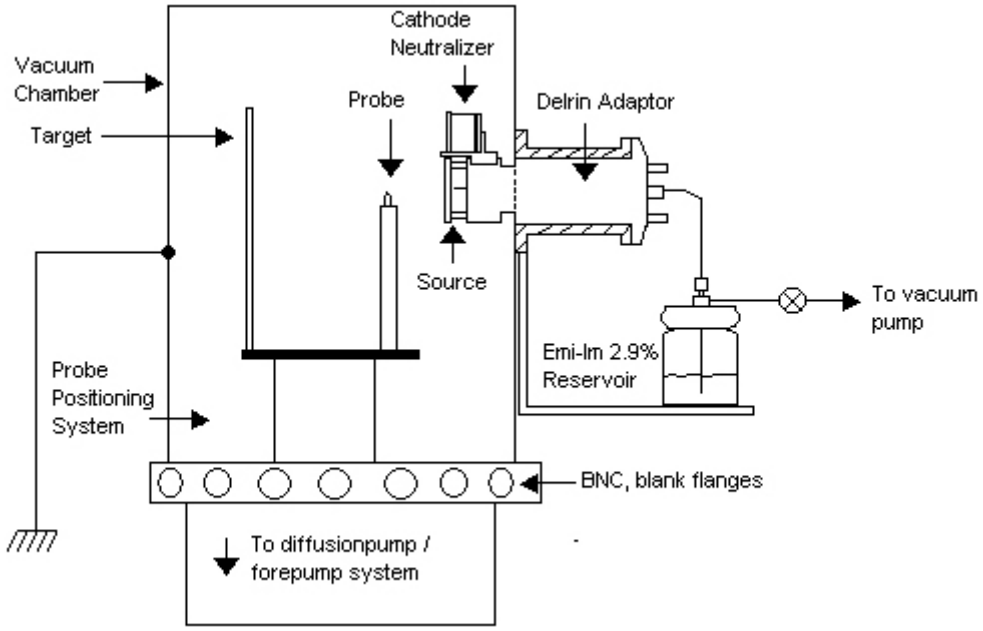

Figure 2.6: Experimental arrangement of the colloid source and targets.

2.1.4 Cathode Neutralizer

The cathode neutralizer originally selected for use in these tests was a Busek Serial Number FEAC-X20-05, which is a field emission cathode based on Busek-grown multi-wall carbon nanotubes (CNT). Multi-wall nanotubes refer to the many concentric tubes

grown within each other, allowing for a multitude of sharp tips at which electrons may be emitted[24,25]. These nanotubes are deposited on an emitter substrate, which is electrically isolated from the base on which it is mounted. A gate is mounted over this CNT emitter, and is at the same potential of the mounting base. The gate (which is grounded to thruster common) is at a higher potential than the negatively biased CNT surface. This potential difference produces the electric field needed to accelerate the electrons emitted from the CNT surface[23].

To decouple the kinetic energy of the emitted electrons from the potential difference needed to establish emission, an electrically isolated decelerator electrode was mounted over the gate, which can be connected to thruster common. There are three surfaces of interest in the electrons path: the carbon nanotube surface, the gate electrode, and the decelerator electrode (Figure 2.7). The cathode typically operates with the CNT surface at a negative potential (with respect to thruster common) in order to induce electron emission. The positive potential of the gate is therefore positive with respect to the CNT surface as mentioned earlier. This potential difference accelerates the electrons and establishes the emitted current density.

Because the gate potential is set relative to the CNT surface, the potential difference between these two surfaces (and hence emitted current density) remains unchanged as the CNT potential relative to thruster common is adjusted. On the other hand, the kinetic energy of the emitted electrons is set by the overall potential difference between the CNT surface and thruster common (decel electrode). Because the two potentials, that of the

CNT surface and that of the gate electrode are controlled separately, the kinetic energy of the electrons downstream of the decel electrode and the emitted current density can be adjusted independently. Lowering the kinetic energy of the electron stream should improve the space charge neutralization within the plume since the electrons are less likely to travel through (and past) the plume with minimal interaction. The configuration is shown in Figure 2.7.

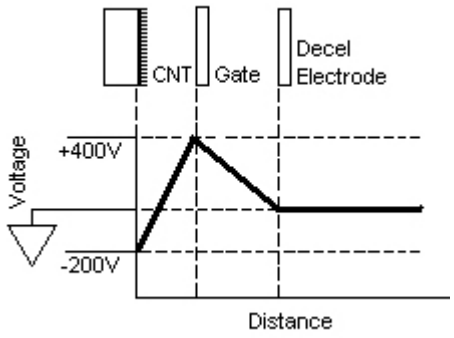

Figure 2.7: Potential energy diagram of cathode emitter similar to electrospray diagram.

The FEAC-X20-05 has been designed for 0.5mA output and was tested up to 1.8×10^{-5} Torr. The current-voltage characteristic for this device was measured by Busek prior to delivery, and is shown below in Figure 2.8.

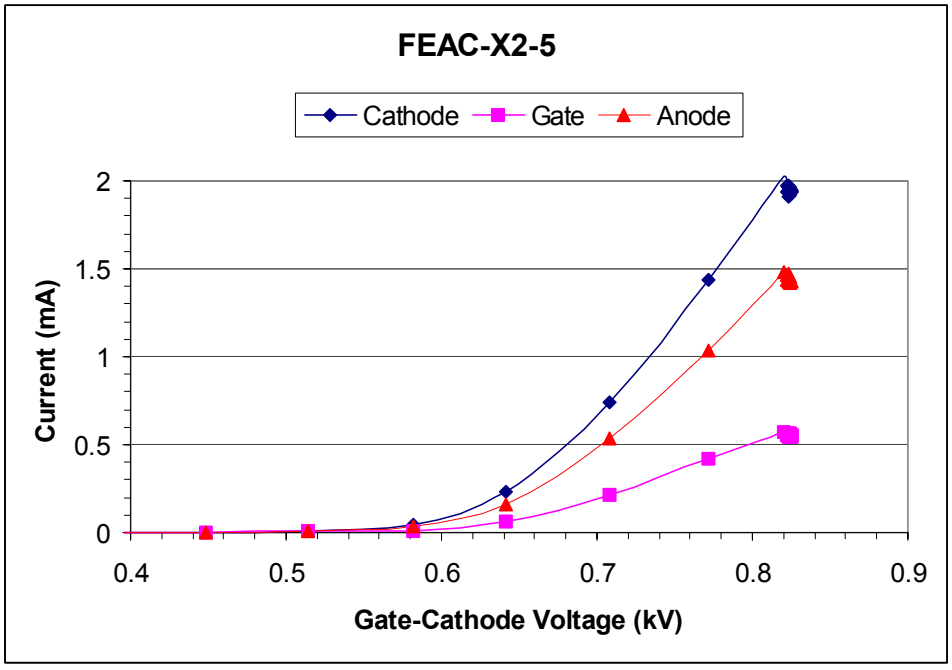

Figure 2.8: Current-voltage operating characteristics for cathode FEAC-X2-5 tested in vacuum of 1.8 x 10^{-5} Torr. (Plot courtesy of Busek Co.)

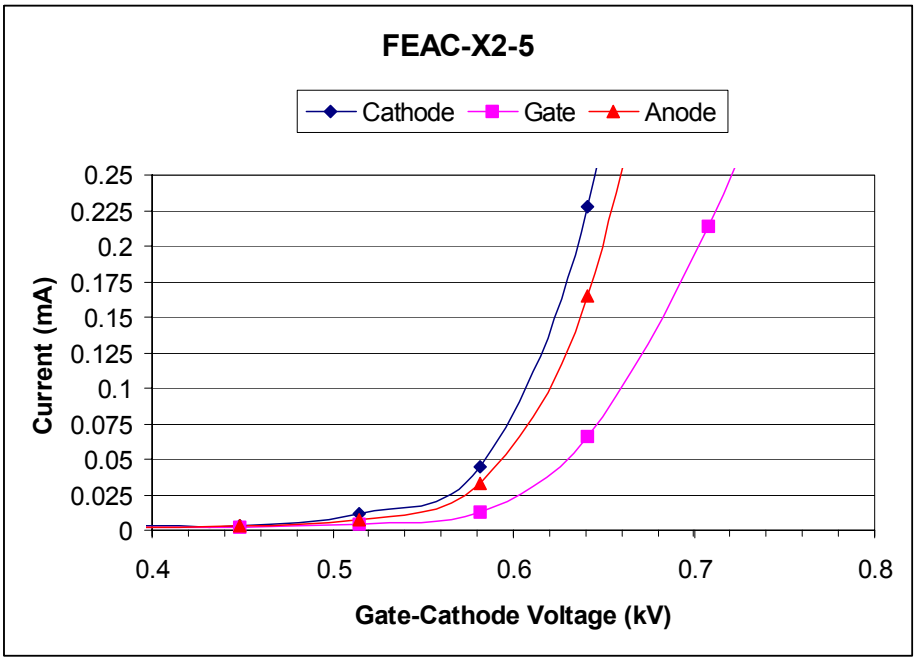

Figure 2.9: Current-voltage plots for cathode FEAC-X2-5. Same plot as in Figure 2.8 but with low current region magnified.

2.1.5 Power Processing Unit (PPU) and Data Acquisition

The Power Processing Unit provides power output, signal conditioning and diagnostic telemetry for the Cathode Surface, Cathode Gate, Needle Emitter, Extractor and Cathode Decelerating Electrode.

Figure 2.10 shows a functional block diagram of the PPU, while Figure 2.11 shows the actual PPU interior. A complete electrical schematic of the PPU can be found in Appendix B.

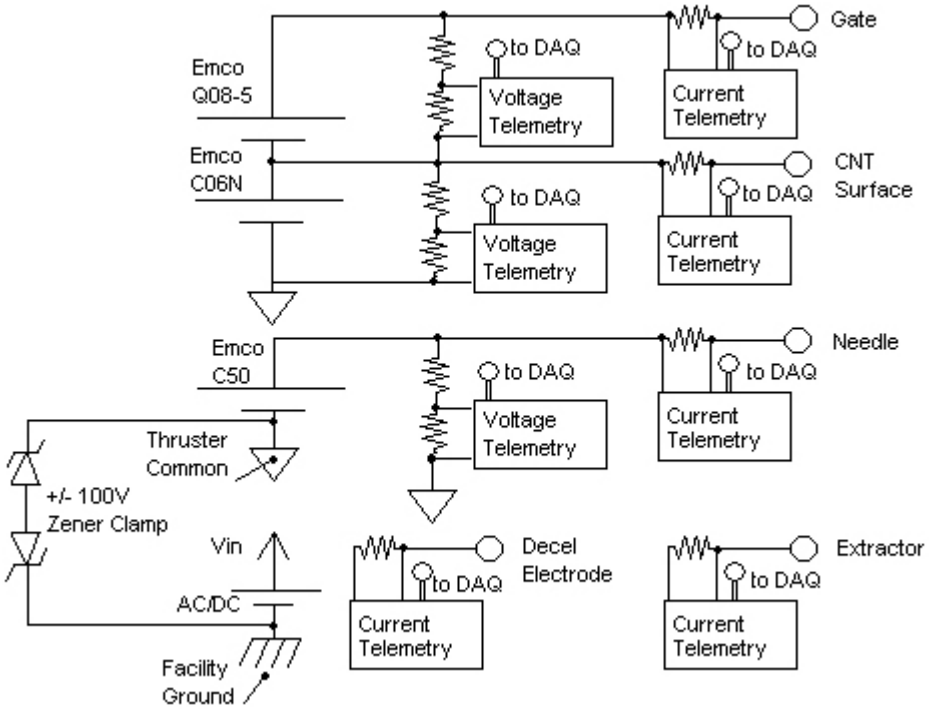

Figure 2.10: Functional Diagram of the PPU.

The primary purpose of the PPU is to provide power to each of the components of the thruster (needle, extractor, cathode, and gate), while simultaneously providing voltage and current telemetry directly to the data acquisition system that receives the analog input

signals and converts them to a digital form allowing data storage. Two reference potentials are used to specify voltages: Facility Ground ("ground") and Thruster Common ("common"). Ground is simply "true" ground or "earth" ground. This is the reference for the data acquisition card. Common is isolated from ground, and each component of the thruster is referenced to this point. Having an isolated thruster common allows the thruster to electrically float, as well as allows the measurement of the thruster floating potential under particular experimental conditions (e.g. charging due to lack of neutralization from the cathode). This technique was useful in studies of similar FEEP thrusters[11]. Common is isolated from ground and is permitted to vary by as much as ± 100V before being shunted by Zener clamping diodes (to protect the DAQ system).

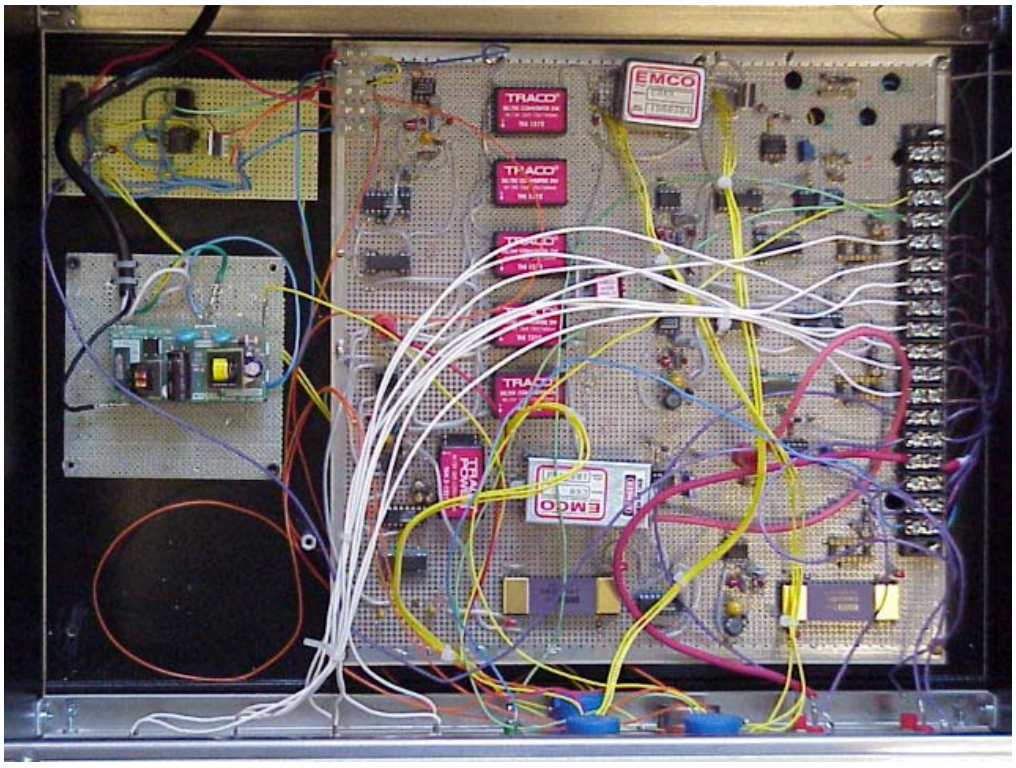

Figure 2.11: Photo of PPU internal layout. Visible are the TRACO converters, EMCO converters, AC/DC power converter, as well as the ISO121 isolation amplifiers and outputs.

DC/DC Converters take an input DC voltage, and convert it to a different output voltage: the output can be isolated from the input if desired. An example of a converter used only for isolation is the TRACO 1212, which takes an input DC voltage of 12V (relative to ground, in the PPU) and produces an output of 12V (relative to common). This provides power to some of the other integrated circuits, which are referenced to common, and must be isolated from ground. An example of using a converter for both isolation and a change in voltage is the EMCO converter. The needle and CNT are powered by the C50 (Vout = Vin x 1kV, 5kV max) and C06N (Vout = Vin x –120V, -600V max), respectively. The Cathode Gate is powered by the EMCO Q08-5, the output of which is referenced not to common but to the CNT (C06N) output. For example, if the CNT is set to –200V (with respect to common), and the Gate is set to +300V (with respect to the C06N output), the Gate is really at +100V (with respect to common). The extractor and decelerator electrode are connected to common, and therefore need no DC/DC converters to provide a bias.

At their most fundamental level, an operational amplifier changes its output in an attempt to make the potential difference between its inputs as close to zero as possible. Their outputs, then, in the proper configuration, can indicate the magnitude of a voltage. In the PPU, the LF411 op-amp measures the voltage across a high-impedance (~100MΩ) voltage divider. The combination of voltage divider and LF411 provides the voltage measurement for the needle, CNT and gate as shown in Figure 2.11.

To measure the current, the voltage drop is measured across a small (~1kΩ) resistor in series with the DC/DC converter output. A small resistor is used so as to not seriously

burden the converters, and thereby reduce the output voltage to the thruster. Small changes in current (~10nA) create very small voltage drops across such small resistors (10nA through a 1kΩ resistor creates 10μV). In order to measure these small potentials in the DAQ system, we must amplify the voltage to a readable range for the data acquisition card (~1 to 10V) without creating significant electrical noise. This is made possible by the specialized configuration of several op-amps known as an instrumentation amplifier. In this case, the INA110 was used to measure the currents through the three PPU powered circuits (needle, CNT surface, and gate) as well as the currents through unpowered circuits connected to Common (extractor and decelerator electrodes). For these last two, the currents result from charged droplets, ions, or electrons impinging on the electrode surfaces.

The outputs of these voltages from both the LF411 and the INA110 are still referenced to common, and must be sent to the DAQ system, in which all signals are referenced to ground. An isolation amplifier uses a particular arrangement of op-amps to take an input signal with respect to one reference point and output the same potential with respect to a different reference. In the PPU, the ISO121 (for the high voltage needle) and the ISO122 (for the lower voltages) was used to provide this isolation (impedance between common and ground is ~1TΩ).

The voltage and current monitor circuits produce an output signal that is linearly related to the input, and as such the behavior of each can be characterized by a slope and a y-intercept (the y-axis being the circuit output and the x-axis being the actual quantity being measured). Although the output can be predicted in principle, the IC's, transistors,

resistors and capacitors used in the circuits each have a finite, albeit small, error. To test that each circuit is working, and to truly quantify the slope and y-intercept, one must calibrate each circuit by comparing the known inputs (voltage or current) with the output of the circuit. The circuit configuration for calibrating the needle current can be seen in Figure 2.12a. The voltage divider used here was R1 = 3GΩ, R2 = 1GΩ (V2 = Vin*R2/(R1+R2) = Vin/4). These values were chosen to reduce the EMCO C50 output voltage to within the limits of the measurement devices (the Fluke multimeter and Keithly electrometer are limited to 1kV and 200V, respectively). The resistors were also chosen to drive the current to values one would expect to measure in a single electrospray, approximately several hundred nanoAmperes (2kV / 4GΩ = 500nA). The gate and CNT circuitry provided voltages well below the Fluke limit, so a voltage divider was not used in those cases, and typically a resistor on the order of 1 GΩ was used to drive the current to the appropriate range.

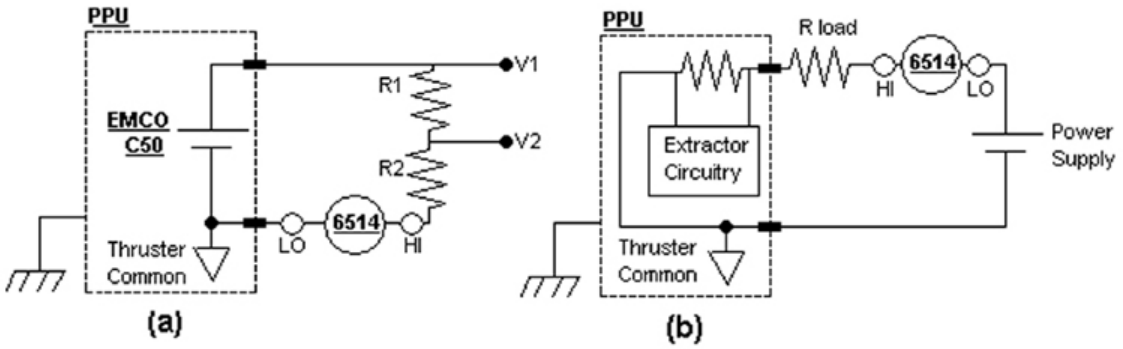

Figure 2.7: Calibration circuit for (a) Needle current and voltage, and (b) Extractor current.

Calibration for the extractor and decelerator electrode was slightly different. To induce a particular current on the other channels, a resistor in-series with the converter output was used. Because there is no converter driving the extractor and decelerator channels (these

are unpowered), an external power supply and in-series resistor was necessary in order to adequately simulate an incident current from the electrodes in the 10-100nA range (Figure 2.12b).

The output of each telemetry channel is the raw data that that the DAQ card and LabVIEW program record. This raw data is plotted against the "actual" signal as measured by an external factory calibrated device (either a Fluke 83III multimeter or the Keithley 6514 electrometer). Sample data for the needle current is shown in Figure 2.13. A complete list of the resulting slope and y-intercepts resulting from calibrations of each channel can be seen in Table 2.1. Multiple calibrations for a particular channel were needed as components were replaced or repaired in the PPU.

Table 2.1: A listing of each of the calibrations for each of the telemetry channels. The units listed in the Channel Description column represent the "y" axis, while the "x" axis is Volts in all cases.

PPU Channel	Channel Description	Curve Fit	Units	Date
0	Needle Voltage	y= -546.8(x) -191.4	V	07/02/03
1	Needle Current	y= 409.5(x) -49.82	nA	07/02/03
2	Extractor Current	y= -97.48(x) -108.3	nA	06/25/03
3	CNT Voltage	y= -106.4(x) - 36.47	V	07/16/03
4	CNT Current	y= 9757.3(x) -306.4	nA	07/16/03
5	Gate Voltage	y= -107.18(x) +31.18	V	09/19/04
6	Gate Current	y=9789.9(x) -586.85	nA	07/16/03
7	Decel Current	y=-166.1(x) +35.52	nA	07/02/03

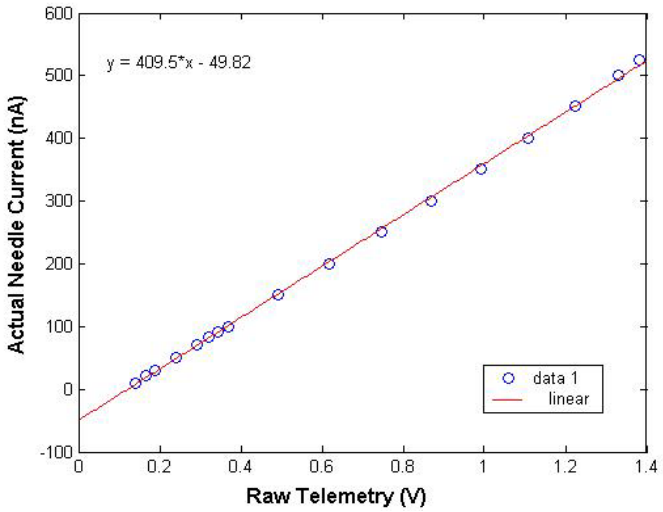

Figure 2.8: Needle current calibration curve. Linear fit is typical of all telemetry channels over ranges of interest.

Common and ground are isolated from each other throughout the PPU, but it is important to note the points for possible current leakage from Thruster Common to Facility Ground: (a) the zener clamp (10GΩ), (b) the TRACO DC/DC converters (1GΩ), and (c) the isolation amplifiers (100TΩ barrier impedance). The impedance of each of these devices is greater than 1GΩ, so unless the two grounds are jumped together, the leakage between the two grounds is minimal (i.e. on the order of 100V / 1GΩ = 1nA).

2.2 Emissive Probe Techniques

This work uses the two techniques discussed previously in the literature review: the strongly emitting floating probe technique and the voltage sweep technique. The procedure for each technique shall be discussed in detail.

2.2.1 Procedure 1: Strongly Emitting Floating Probe

This series of tests used the floating point in strong emission method: the probe emission was varied via heater power, while the probe potential and other diagnostic telemetry

were monitored. This experiment did not use a neutralizer cathode, and all voltages are referenced to facility ground.

In our experiments, we implemented the floating probe technique in the following manner. First the vacuum chamber was pumped down, then once a vacuum on the order of 10 or 20 microTorr was achieved, we placed the end of the needle in the propellant reservoir. At the same time, we activate the DAQ system and began recording telemetry at 1 sample per second. At the same time, a NIST-certified stopwatch was activated as an external reference for the DAQ system. This allowed external observations to be correlated to the data (e.g. at 1335 seconds the flowrate was briefly interrupted, which should correspond to a drop in electrospray current around data point #1335).

The needle voltage was then turned to approximately 2kV, and the telemetry—needle current, target current, depending on the experimental configuration—is observed to establish a stable electrospray. Once a stable spray is established, the filament power is slowly increased. Occasionally, a filament would burn out (indicated primarily by probe current going to zero), and it would be replaced, allowing the experiment to continue after approximately 30 minutes (most of this time is taken by re-evacuating the chamber). Typically, the probe is usually increased to a power level below the observed threshold of filament burnout (under 8W) and then the power is decreased.

Three different experimental configurations were used: configuration A for case FP1 (Floating Probe test 1), configuration B for case FP2 and configuration C for case FP3.

Configuration A is shown in Figure 2.14. The heater power supply, PS(H), an Operating Technical Electronics, Inc (OTE) HY3005-3 (dual output 35Vmax) was electrically isolated with an isolation transformer rated at 1.5kV. A1 is an OTE DM-568C multimeter, and R1=R2=100Ω. A2 is a Keithley 6514 electrometer. The probe and target (30.48 cm x 30.48 cm) are on the same moving track (section 2.1.2), and their distance is kept fixed. Vp is a Fluke 83III digital multimeter used to measure probe potential. The distance between probe and target is 18.85 cm. The distances listed (0.33, 2.71 and 5.25) cm correspond to the distance between the probe and the edge of the extractor electrode. These distances were selected to bring the probe as closely as possible to the electrospray: it was assumed that the closer (axially) the probe is to the electrospray source, where the concentration of droplets is higher (due to less spray divergence), the greater chance of observing a difference in probe behavior in the presence and absence of the electrospray. The distance between the outer edge of the extractor to the tip of the emitter needle is 0.64 cm. The electrospray source consists of the long Delrin piece mounted to a QF50 flange. The PPU collected voltage signals from the needle and current signals were collected from the needle and extractor. Target and probe telemetry were obtained by manually recording data from the digital displays of the devices used.

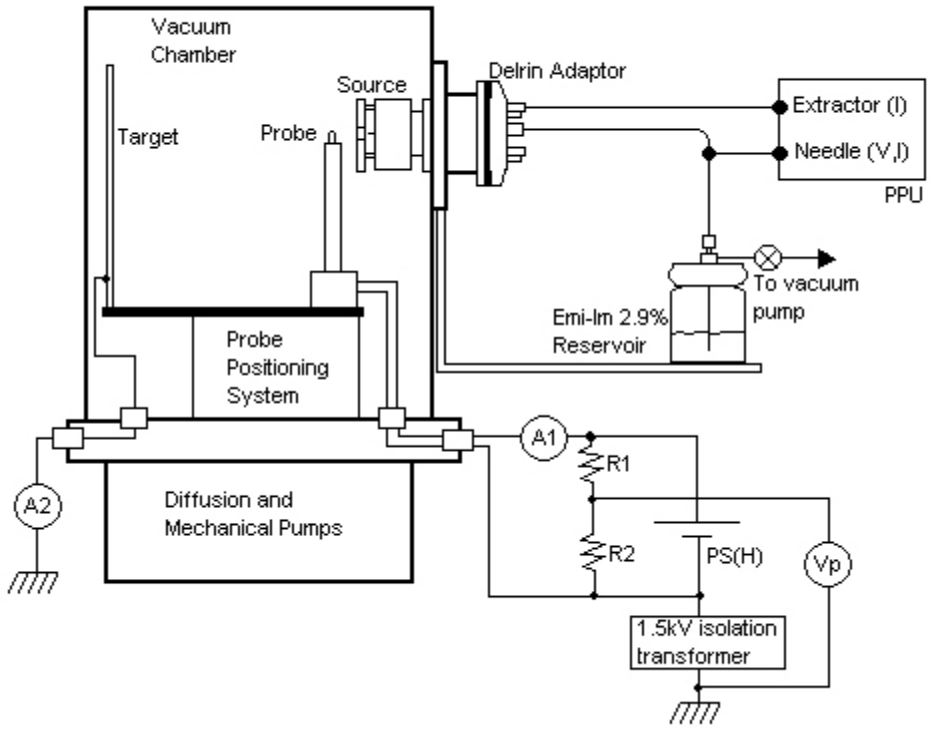

Figure 2.14: Sketch of experimental configuration A, employing the strongly emitting method of measuring plasma potential.

Configuration B is shown in Figure 2.15. The primary difference between A and B was the electrospray mounting, featuring the short Delrin piece previously described mounted to a QF50 cross. Window ports are mounted to the sides of the cross are to enable viewing of the cross interior. This configuration facilitated visual confirmation of the electrospray while repeating the same floating probe measurements used in configuration A. Other improvements to the configuration included PPU data collection of the Probe voltage via a 1/30 voltage divider (R3 and R4 are 10MΩ and 33kΩ , respectively) and target current (via the Keithly 2V analog output).

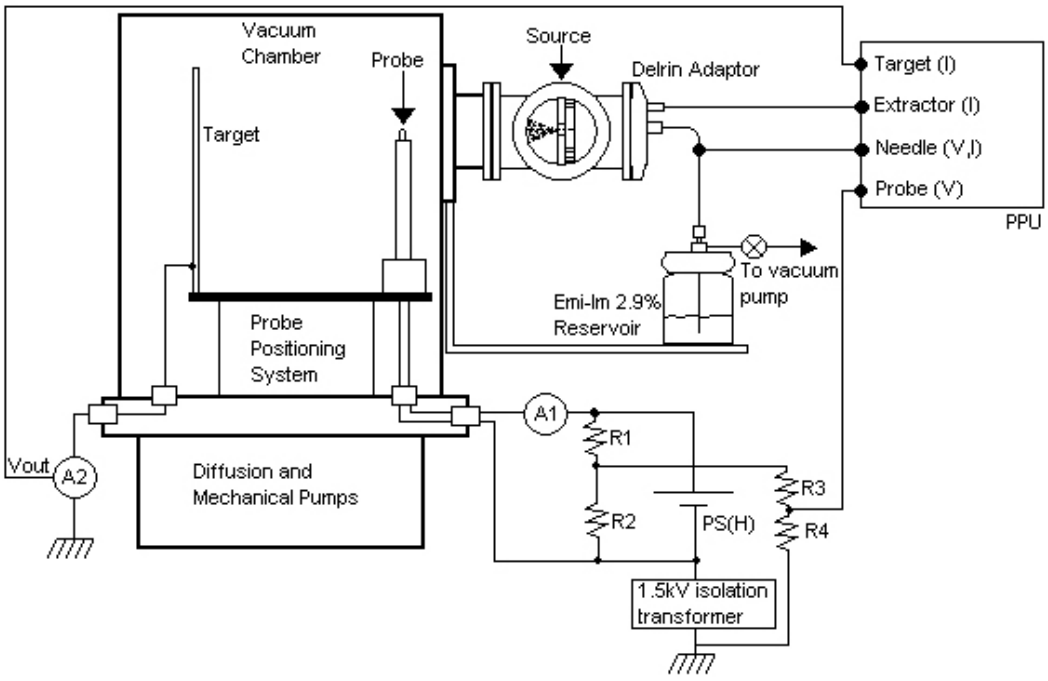

Figure 2.15: Sketch of experimental configuration B, employing the strongly emitting method of measuring plasma potential.

In an effort to combine visual confirmation of the electrospray (characteristic of configuration B) while maintaining the shortest possible distance between the probe and the electrospray (characteristic of configuration A), we created experimental configuration C. This configuration was characterized by a probe mount with a 90-degree bend that, in combination with the automated probe positioning system, allows the probe to be moved axially upstream of the electrospray plume to within approximately 2cm of the source. Configuration C is shown in Figure 2.16.

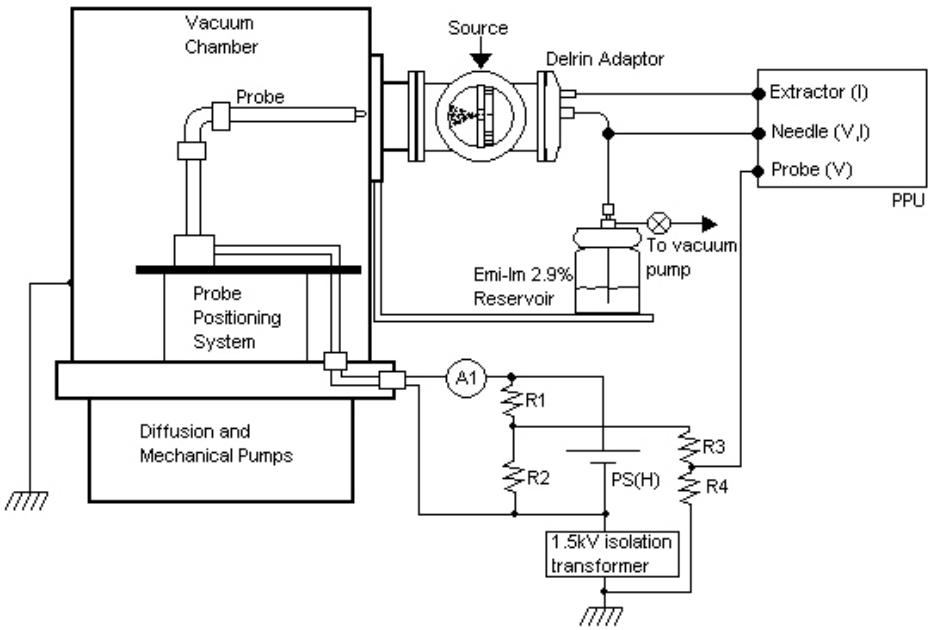

Figure 2.16: Experimental configuration C, allowing both visual confirmation of the electrospray as well as probe testing in the axial range of interest (< 5cm).

2.2.2 Procedure 2: Sweeping Probe Voltage

An alternative technique in determining the plasma potential involved sweeping the probe voltage. Instead of increasing heater power, we kept the heater power at a value sufficiently high to ensure emission, and varied the probe potential while monitoring the net current to facility ground.

Figure 2.17 shows configuration D, used in the first two tests (VS1, VS2) using the sweeping voltage technique. The heater power supply was isolated from facility ground via an isolation transformer as in the floating probe technique. The heater voltage was indicated via an internal digital readout on the supply. Ammeter A1 is an OTE DM-568C DMM, A2 is a Fluke 83III DMM, and A3 is a Keithly 6514 Electrometer. R1 and R2 are

100Ω (25W). PS1 and PS2 are the Instek GPR-3060 (Vmax=35V) and the Kepco ATE 55-100 M (55V / 10A max). These power supplies were connected in series (range 0 to +90V) in case VS1. In case VS2, PS2 was replaced with a Kepco APH2000M power supply enabling the range –300 to +35V. Once data was collected in configuration D, as in the floating probe technique, we wished to visually confirm the active electrospray. As such, we incorporated configuration C in the final case, VS3.

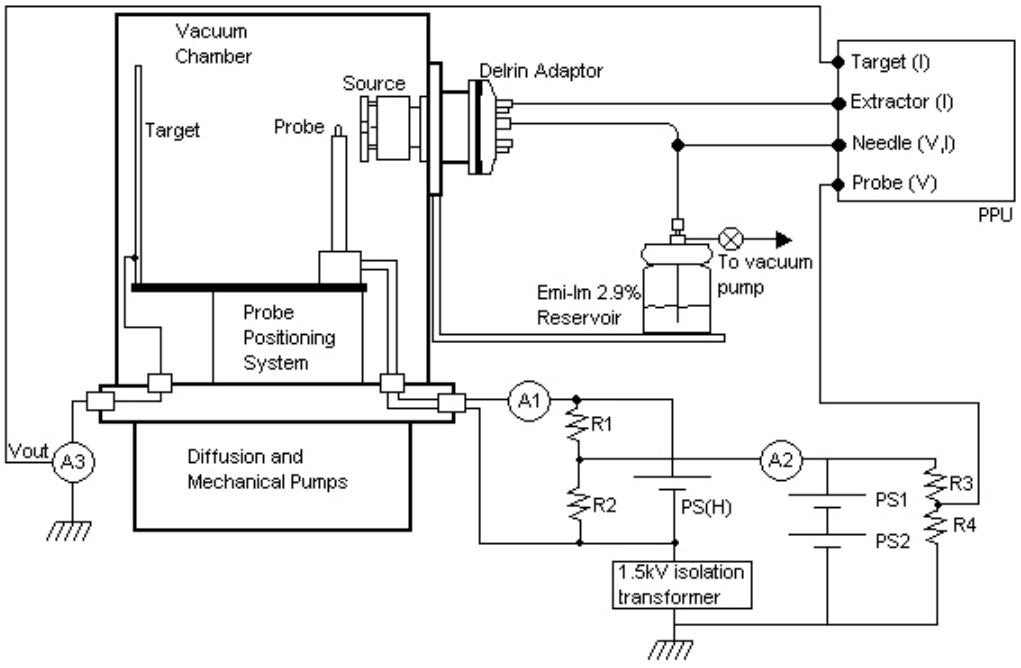

Figure 2.17: Experimental configuration D.

3. Results of Emissive Probe Measurements

This chapter presents results from the emissive probe measurements completed as part of this thesis. We begin with a survey of the sensitivity of the devices used to collect data, followed by an explanation of the error analysis in each experimental. We then discuss each of the experiments, using electrospray performance and probe data to understand the results.

3.1 Probe Measurement Results and Analysis

Two techniques were used to determine plasma potential: the strongly emitting floating probe, and the sweeping probe voltage. The experiments were initially performed using a beam target, as this provided us with a means to verify that the currents from the needle, extractor and probe summed consistently. These experiments were followed by an alternative facility configuration that enabled visual confirmation of the electrospray, although this configuration precluded target telemetry. The discussion begins with the results of tests with the strongly emitting floating probe—first in the configuration with the target telemetry, secondly in the configuration that provided visual confirmation of the electrospray operation. We then discuss the results from tests in which the probe potential was varied. The latter tests were performed in several experimental configurations.

3.1.1: Strongly Emitting Probe

The strongly emitting probe theory and general application has been discussed in the previous chapter, as were the experimental configurations associated with each test. Here

we discuss the test results obtained employing configuration A (Case FP1a, FP1b, FP1c) and configuration B (Case FP2).

3.1.1.1: Strongly Emitting Probe—Case FP1

As discussed in other research[16,11], the use of a strongly emitting probe (where the emitted current is much greater than the collected current) can provide an effective means of measuring the plasma potential. Space-charge limitations can be a significant factor if the plasma density is low[16,11]. In such a case the space charge "cloud" surrounding the emitting probe limits how much current can be extracted. If this limitation occurs before the probe has emitted sufficiently to float up to the surrounding plasma potential, the diagnostic will be ineffective.

The plasma densities in a colloid plume are expected to be low. Measurements of the plasma potential of the FEEP, a comparable electrostatic thruster in terms of thrust produced, have been made[12], but the similarities of these two technologies are limited: for example, the FEEP beam current is orders of magnitude larger than that of a single needle colloid thruster (~100μA vs.~100nA, respectively). Because the beam current is so much lower, it was decided to first measure the emissive probe floating potential with the electrospray turned off (in the limit of zero plasma density) and then to compare this with values measured with the electrospray turned on.

The first test results[27] can be seen in Figure 3.1, using the floating probe method and the test configuration A (Figure 2.14). The probe floating potential is plotted versus the heater circuit power (which is a measure of the emission capability of the filament). The lower curve (blue diamonds) represents the case with no electrospray present. In the absence of ambient plasma, the second change in slope (occurring at approximately 1.4W) is believed to correspond to the point where the emission becomes space charge limited and therefore only increases slightly with increasing heater power. In Figure 1.2, Kemp and Sellen's measurement of a floating probe in a dense ($10^9 cm^{-3}$) plasma shows a similar behavior, albeit at much lower emission capability (several dozen μA vs. several nA in our filament).

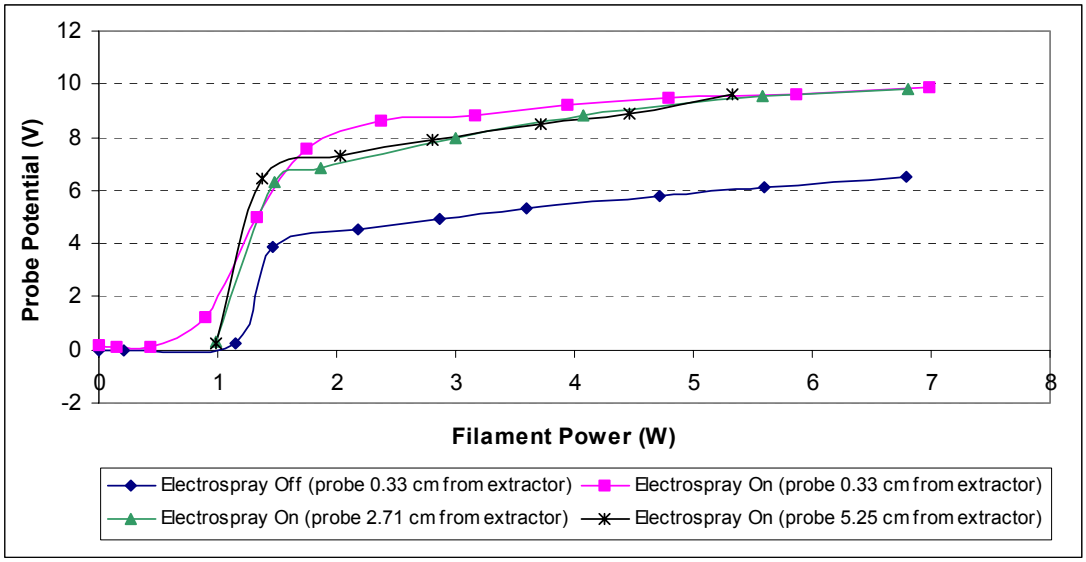

Figure 3.1: Case FP1, Floating Probe potential vs. Heater filament power. Probe potential uncertainty is estimated to be within ±10mV. Filament power uncertainty is estimated to be ±0.92W for the electrospray off and ±0.69W, ±79W and ±0.83W for Case FP1a, FP1b, and FP1c, respectively.

The plotted values of the floating probe potential correspond to the voltage needed to sustain the emission current through the load line impedance (in the voltmeter). These measurements were taken using the Fluke 83-III digital multimeter with an internal

impedance of 10MΩ. At a filament power of 2W, the floating potential is approximately 4.4V. For a load resistance of 10MΩ, the emitted current is 440nA.

At the same location (0.33 cm from the extractor), with the electrospray turned on, the probe floating potential increases to 8.3V. Positive ions or droplets (as well as any secondary electrons from the target) reaching the filament will result in an added current to the load line circuit. Considering again the point corresponding to a filament heater power of 2W, the corresponding load current is 830nA. The additional 390 nA would have to come from either 1) the ion/droplet current, 2) secondary electron emission from the filament or 3) additional emitted (thermionic) electrons.

The electrospray current for this test was less than 300nA (Figure 3.2), which eliminates the first possibility. As for the second possibility, it is unlikely that secondary electrons would account for such a large relative increase in current: at only 300nA, the ions/droplets are not expected to be sufficiently energetic. In addition, considering the relatively small cross section the probe presents to the spray (0.003cm^2, with relevant cross section geometry found in Table 3.1), the secondary emission yield would have to be very large. The last possibility is the most likely: if the emission is in fact space-charge limited in the case with no electrospray turned on, then the increase in current with the spray on may indicate the local space-charge has been altered due to the presence of the ion/droplets.

Table 3.1: Values showing the calculation of wire cross section. The final column represents the percentage of the filament area vs. spray cross-section area.

probe distance (cm)	spray x-sect radius (cm)	A-spray (cm^2)	A-wire (cm^2)	wire % of spray area
0.33	0.191	0.114	0.003	2.631
2.71	1.565	7.691	0.003	0.039
5.25	3.031	28.863	0.003	0.010

The three curves with the electrospray on correspond to three different distances from the extractor surface. There is little variation that can be resolved with the collected data. One possible cause for this behavior is that the plasma potential distribution has leveled out at these distances from the emitter. Comparable work[12] with a FEEP thruster suggests that the difference between the closest and furthest position is large enough where some variation should be evident. As such, it is more likely the lack of variation is due to the probe emission being space charge limited. This would mean the probe potential could not float up to the plasma potential.

In evaluating the results of the test above, it is critical to understand in some detail the plume being generated. As such, in this section we describe measurements made to characterize the performance of the electrospray source.

We monitored the current and voltage of system components when the electrospray was on for three distances between the probe and electrospray: 0.33cm (Case FP1a, Figure 3.2), 2.71cm (Case FP1b, Figure 3.3), and 5.25cm (Case FP1c, Figure 3.4). The sign convention is as follows: positive droplet (or ion) emission (electron collection) corresponds to a positive current; positive droplet (or ion) collection (electron emission) is corresponds to a negative current. This is true for all currents except the target current, for which a positive current corresponds to positive droplet (or ion) collection. In each of these cases, the heater power was varied with time. The behavior of the electrospray was monitored and is plotted over the same time period as the probe heater power for comparison. We divide case 1 into three time periods: Period 1 (0 to 225s), Period 2 (226 to 310s), and Period 3 (311 to 750 s).

In the first period, the needle current is –90nA: we believe leakage current in the current monitoring telemetry exists on the order of 100nA or more, which has made electrospray emission at such a low current difficult to measure. The telemetry measures higher current values (~1uA) more accurately, as such current measurements below several hundred nanoAmperes (a significant fraction of 1 μA) are unreliable due to leakage current through some element of the current monitoring circuit. As this current-monitoring circuit is the only one that is suspect, and it is the only such circuit connected to high (~kV) voltage, it is likely the circuit wasn't properly isolated.

The –10nA the extractor measures indicates the extractor is intercepting +10nA of the emitted ion current. The target current is +60nA, indicating the collection of positively charged droplets or ions. Summing the extractor and target currents is an "independent" means of checking the measured needle current, which in this case must be (according to this independent check) greater than or equal to 70nA (given the beam divergence, as well as the distance of the target, it is likely that at least some of the spray hit the walls of the tank). Further, it is likely the electrospray current is much higher, as the target is expected to only measure a fraction of the current, as additional current may have been collected by the probe. Recall the target current has been our primary indication of an active electrospray in this experimental configuration, given the reliability of the electrometer and the simplicity of the circuit. As such, the target and extractor currents are consistent with the reported needle current (~300nA).

Period 2 is characterized by a fluctuation that is correlated between the needle, extractor and target currents. For all three to be affected simultaneously, it is likely that they share the same cause. One possible cause is an interruption in propellant flow (e.g. a bubble's passing), which would result in a temporary change in electrospray emission, impacting the extractor and target, which are "downstream" of the source. If a bubble passes, the electrospray emission decreases (less propellant to carry the current), meaning less (positive) current. We see instead an increase in positive current, meaning either more droplets are emitted or more electrons are being absorbed (electrically the two possibilities are indistinguishable). Such a significant jump in electrospray emission is possible as a result of flowrate changes. The tank pressure would not indicate such a change in flowrate, as the presence and absence of flowrate didn't alter the ion gauge reading at all. If this fluctuation is not a result of increased droplet emission, it most likely was caused by electron absorption as a result of the emissive probe.

It is during this period that the emissive probe "turned on", and began to emit electrons. This is confirmed by the rest of the telemetry. The probe voltage rises significantly during this period, and the extractor current indicates electron absorption as well. The target indicates electron collection as well. The needle voltage (not reported here) remained unchanged at 2kV, so although the current is "masked" by the emitting probe, the electrospray remains active, even during the increased electron absorption characterizing the needle current during Period 3.

Period 3 shows a positive electrospray current, followed by a negative extractor current and a positive target current. The positive electrospray current can be attributed again to the probe's electron emission—the approximately 330nA increase in electrospray current (between Period 1 and Period 3) is comparable to the 390nA increase driving the floating probe voltage change in the cases of the electrospray on and off at this distance of 0.33cm (Figure 3.2). If the electrospray is responsible for drawing more electrons out of the probe (and thereby raising the potential), it makes sense that the additional 390nA emitted from the probe would show up with the electrospray current. The unaccounted 60nA are partly accounted for with a 20nA "drop" in droplet collection indicated by the target current: the remaining 40nA could have been collected by the chamber walls. Given that the extractor is in front of the needle, it's possible it could have intercepted many of the electrons, but the measured extractor current isn't consistent with this. The extractor current may have been malfunctioning, or the electrons found a path to ground through the plume emitted by the needle electrospray (this latter case is consistent with the measurement because increased electron absorption in the needle would appear as a rise in positive current).

Theoretically, at each point in time, the measured currents should all sum: the emitted current from the electrospray should be roughly equal to the amount of current intercepted by the extractor and the target. Because of the unknown elements involved in the beam current telemetry (i.e. the –90nA needle current cannot be real if the target current indicates a positive spray), summing the currents cannot be a meaningful exercise. The most likely problem is that the needle current, and possibly the extractor

current are not correct, however the data generally indicate an emitting electrospray, which is in this case 0.33cm away from probe.

During the period of "known" stable emission, the heater power was increased at regular intervals, and the probe voltage floated proportionally with the power until approximately 4W. After this point, the probe potential stops increasing significantly at roughly 9V—this is the same floating potential measured at 2.71cm (case FP1b, Figure 3.3) and 5.25cm (Case FP1c, Figure 3.4).

One element of Case FP1b and FP1c telemetry worth noting is that when the probe stops emitting (indicated primarily by the heater power), the needle current returns to –100nA. This is consistent with the electrospray remaining on during probe emission despite a masked current signal. Also, in Case FP1c, during time period 280 to 320, there is a significant rise in needle droplet emission, mirrored by a proportional increase in current collection at the extractor, leading us to interpret the fluctuation as an increase in electrospray emission. Because the target current was recorded manually (via the digital display on the Keithly 6514 electrometer) a corresponding fluctuation in the target current over these 40 sec could easily have been missed.

It is important to note that electrospray current and extractor currents were recorded by the PPU-DAQ card-computer and therefore are synchronized. The remaining data channels were not recorded by the DAQ card. To ensure that the events (both recorded by LabVIEW and recorded by the experimenter) were synchronized to the same timestamp,

a calibrated (NIST-traceable) stopwatch was activated at the start of each test, so an "external" event (such as increasing the heater power) occurring at, say, 300 seconds would be plotted at the appropriate time interview in LabVIEW-recorded data. Each loop in LabVIEW was approximately 1000ms, but a bug in the program was discovered which indicated the loops occurred at smaller time intervals, so that over time, the small error would sum large time discrepancies over the course of a run. As such, every 100 seconds (recorded by the stopwatch), the CNT voltage was varied to 200V (for less than 1 second), and the change in time was manually matched in post-experimental analysis. This reduced the timestamp error to approximately 2-3 seconds, given human error in the manual stopwatch recording process.

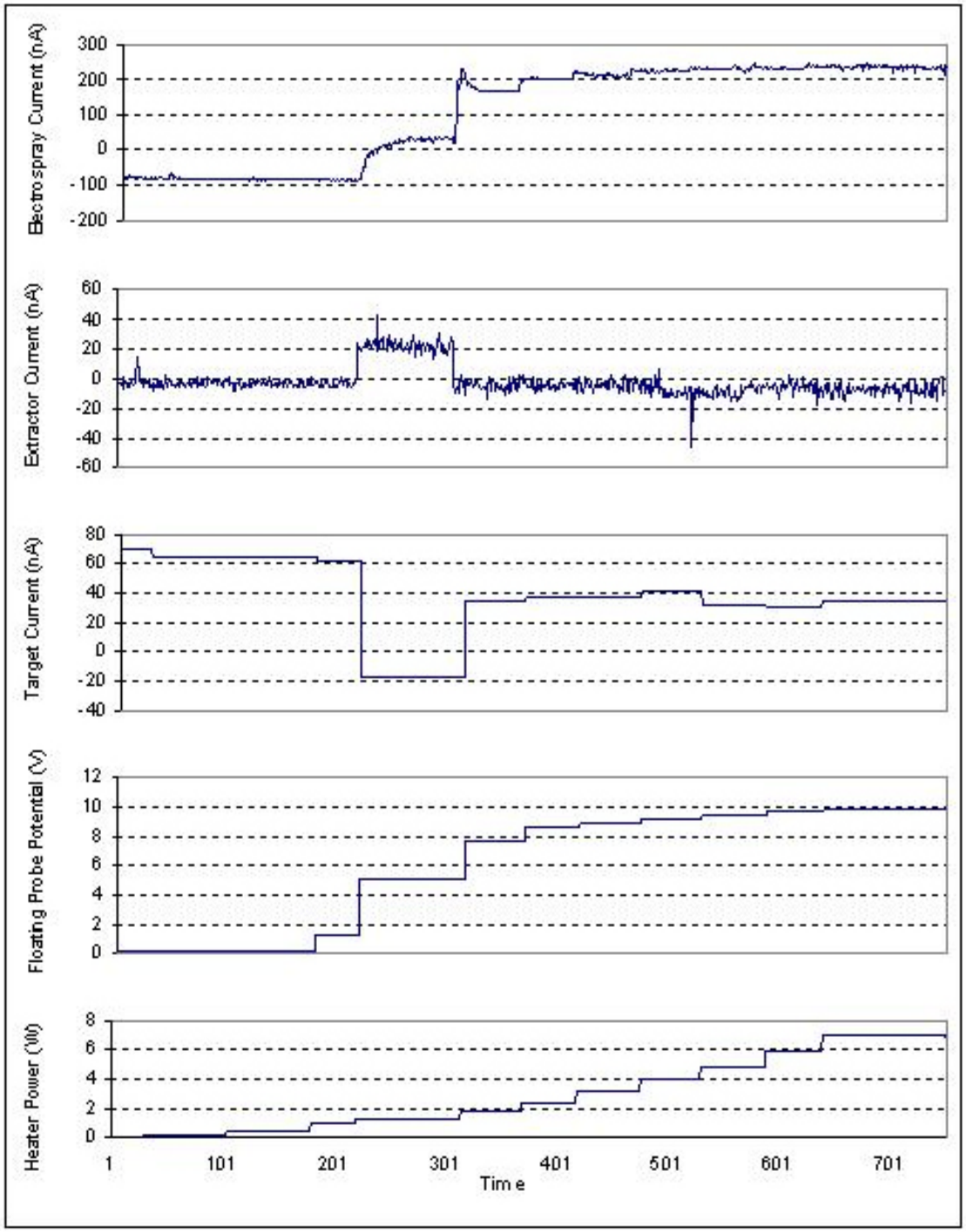

Figure 3.2: Telemetry collected during strongly emitting floating probe test Case FP1a. Heater power uncertainty is ±0.69W, probe potential is ±10mV, target current is ±20nA. The extractor current uncertainty is estimated to be ±0.43nA, the needle current uncertainty within ±3.61nA and the needle voltage within ±9.63V.

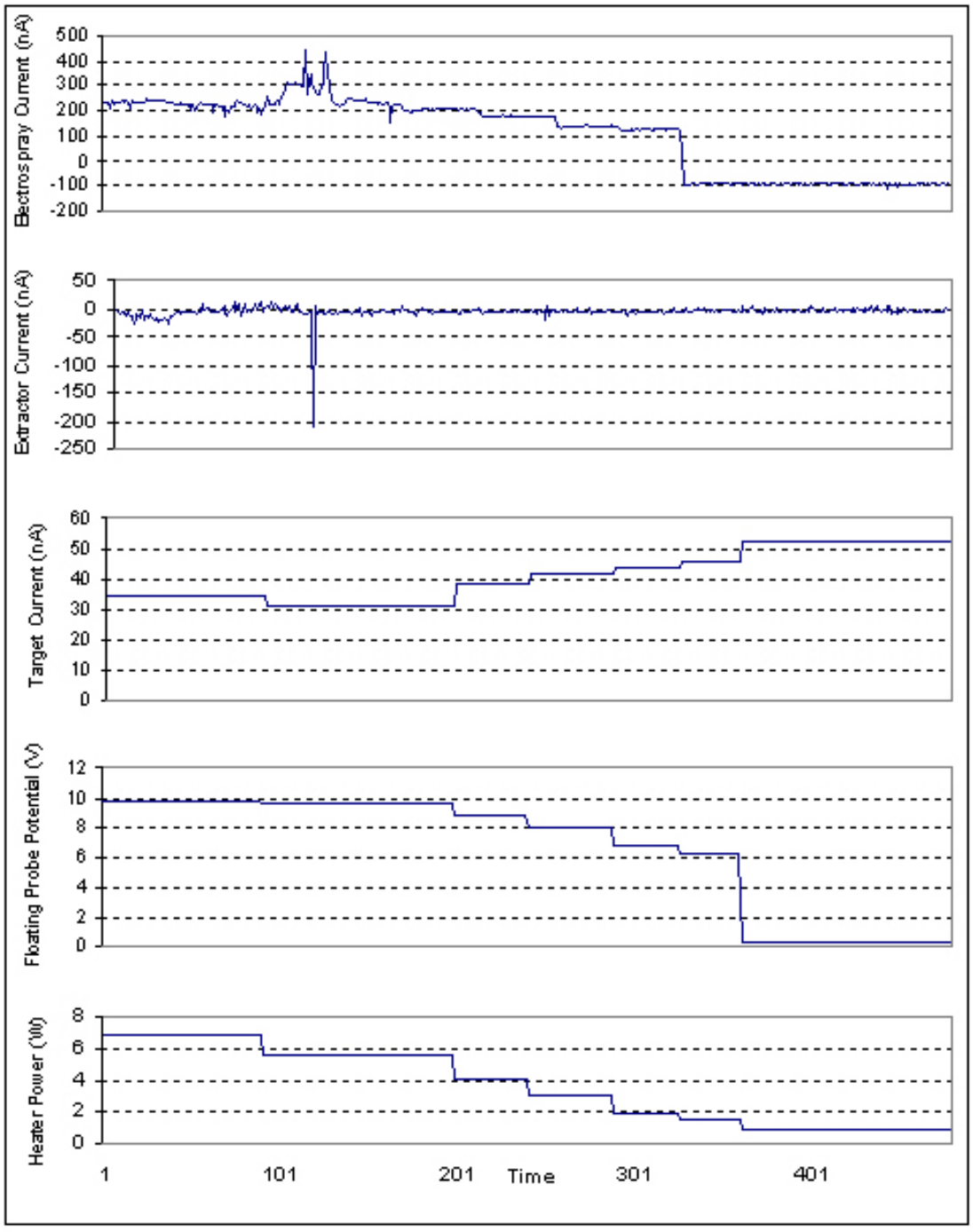

Figure 3.3: Telemetry collected during strongly emitting floating probe test Case FP1b. Heater power uncertainty is ±0.79W, probe potential is ±10mV, target current is ±20nA. The extractor current uncertainty is estimated to be ±0.43nA, the needle current uncertainty within ±3.61nA and the needle voltage within ±9.63V.

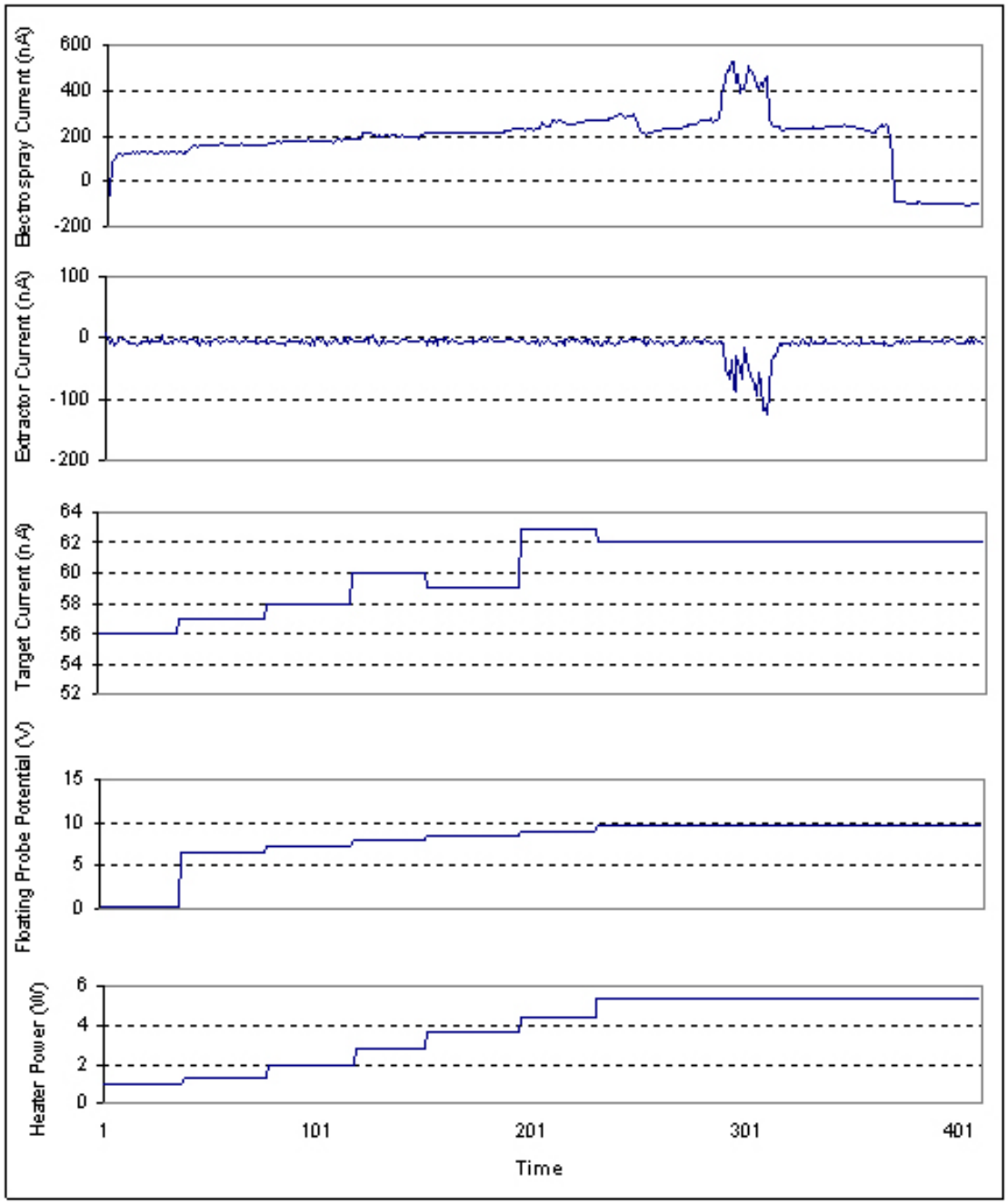

Figure 3.4: Telemetry collected during strongly emitting floating probe test Case FP1c. Heater power uncertainty is ±0.83W, probe potential is ±10mV, target current is ±20nA. The extractor current uncertainty is estimated to be ±0.43nA, the needle current uncertainty within ±3.61nA and the needle voltage within ±9.63V.

3.3.1.2: Strongly Emitting Probe—Case FP2

The previous Case FP1 data was collected close to the electrospray source (1-5cm). Although the target current and needle current were indiciative of an actively emitting

electrospray, there was no visual confirmation of (a) the presence of an electrospray and (b) the type of emission present (single jet from a stable Taylor cone or multiple jet emission characteristic of the highly stressed regime). Visual confirmation would provide an increase in confidence in the results such as those collected in Case FP1.

Case FP2 was a repeat of the previously discussed floating probe test, and we employed configuration B (Figure 2.15). This configuration employs the QF50 cross and magnifying lense for visual inspection of the electrospray, as well as the same probe configuration in Case FP1. The distance between the emitter and the probe is 14 cm. Figure 3.5 shows the results of the results of the floating probe test. The telemetry (Figure 3.6) is consistent with an active electrospray and the results are reasonable. It is clear that there no significant difference between the P-V data collected with the electrospray on vs. the data collected with the electrospray off.

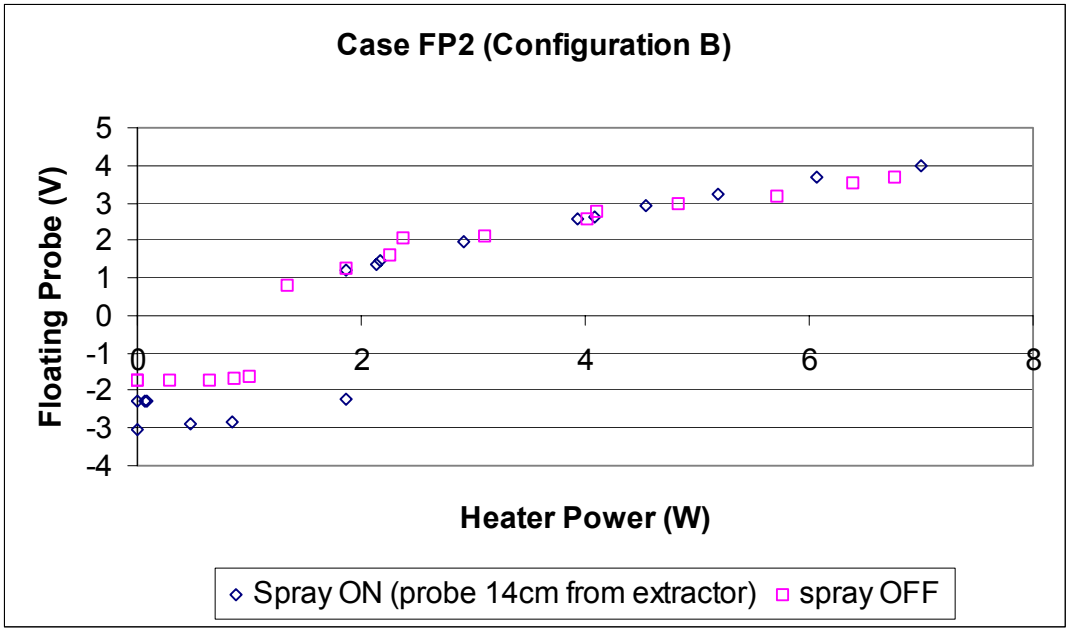

Figure 3.5: Case FP2 incorporating the floating probe technique in experimental configuration B. Probe potential uncertainty is ±0.24V and filament heater power uncertainty is within approximately ±0.83W.

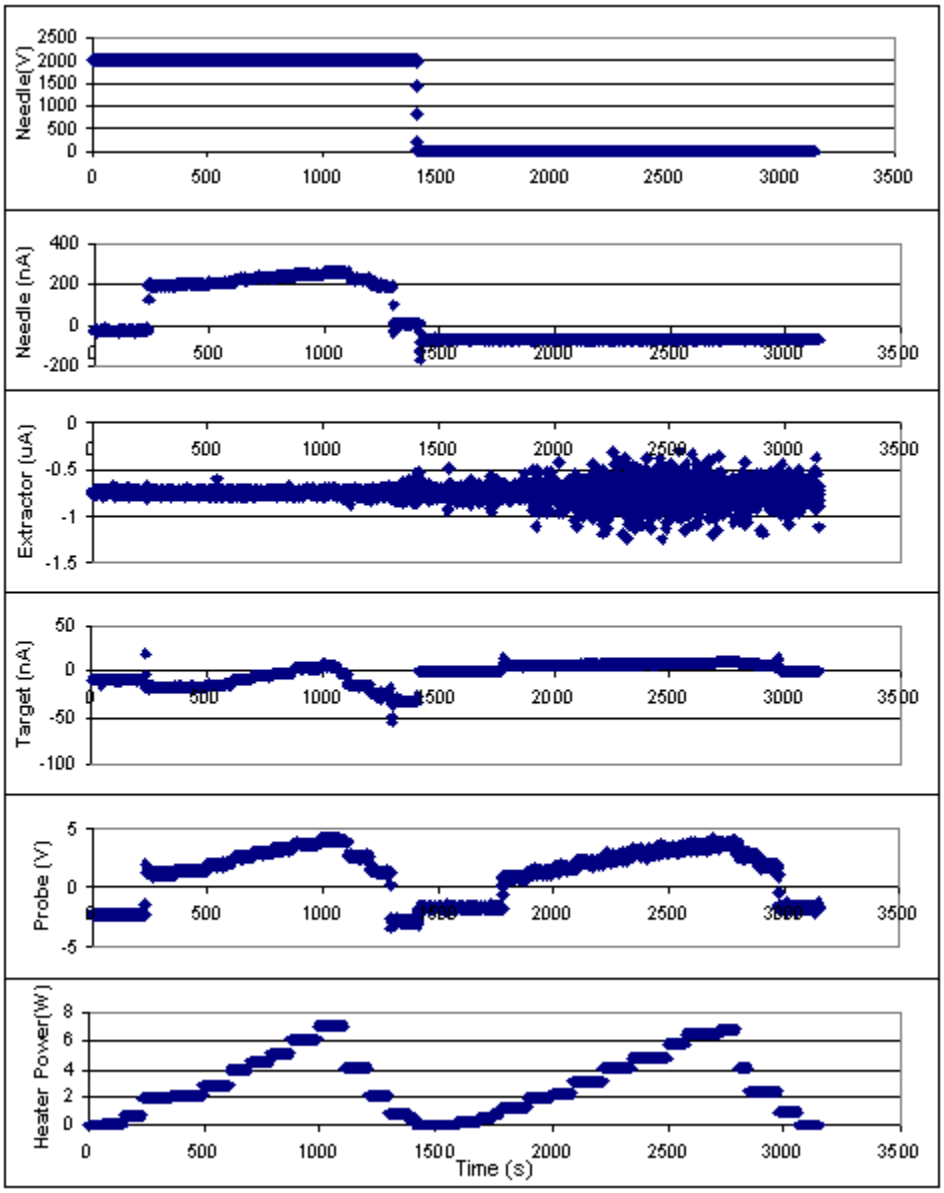

Figure 3.6: Telemetry channels from Case FP2. Heater power uncertainty is approximately ±0.83W, probe potential is accurate to ±0.24V, target current is ±30nA and electrospray and extractor currents are accurate to ±3.61nA and ±0.43nA, respectively.

The electrospray telemetry, visual confirmation/photos of the electrospray, and reasonable shape of the P-V curve seem to indicate a typical electrospray. We believe the similarity in the curves is a result of there not being a dense enough plume to make a difference in the telemetry. This is likely because probe is located at an axial distance where the electrospray is too diffuse to make any signficant difference in probe potential

characteristics. The next logical step, then, was to repeat the test, allowing for visual confirmation, but at an axial distance comparable to those used in Case FP1. Configuration C (Figure 2.16) was designed, built and tested for this reason.

3.3.1.3. Strongly Emitting Probe—Case FP3

Configuration C employs the automated positioning system (section 2.1.2). The closest approach to the extractor plate was approximately 2.7cm. In order to reach that far into the Q50 cross, the probe stand had to withdraw 10 cm back into the vacuum chamber in order to open and close the bell jar. Because the probe had to be brought so far back, and given the physical limitations of the sliding stand (given that it was designed to maximize configuration A or B), there was no room for the target.

Even if the beam target had not needed to be removed for this set of tests, there are two factors which would have compropmised its effectiveness in this configuration. First, the grounded probe mount (stainless steel) is directly along the axial path of the electrospray, and would interfere with the portion of the electrospray that passes the probe. Second, given the roughly 30-deg half angle of the spray, the spray would be partially blocked by the grounded tank walls at an axial distance of 4cm (Figure 2.16). Note the total path through the QF50 port, from the extractor to the vacuum chamber is 13.1cm.

The floating probe data for this case can be seen in Figure 3.7. The experimental configuration (electrical) can be seen in Figure 2.16. As in Case FP1, there is a 10M-ohm impedance path to ground. With the electrospray off, the probe potential hits a plateau at approximately 2.5V, corresponding to a current emission of aproximately 250nA. The case with the electrospray on has a plateau of approximately 6 volts (corresponding to approximately 600nA). The approximately 350nA increase in current draw is consistent with the current increase in Case FP1 (which was 390nA). The electrospray in this case was stable, and images of the electrospray can be seen in Figure 3.8.

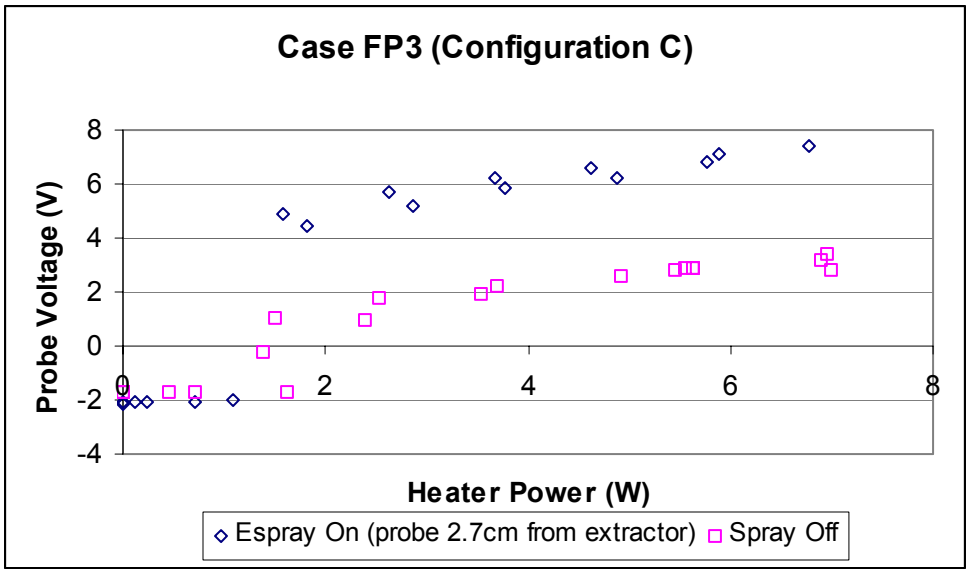

Figure 3.7: Case FP3 incorporating the floating probe technique in experimental configuration C. Probe potential uncertainty at approximately ±0.24V and filament power uncertainty is at ±0.75W.

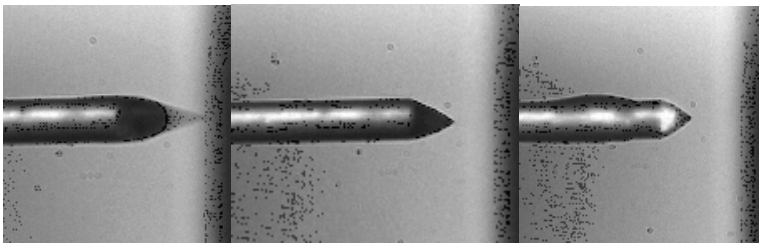

Figure 3.8: Images of the active electrospray taken during Case FP3.

The telemetry from this test can be seen in Figure 3.9. There is no extractor current listed here because it was discovered the extractor was in physical contact with the electrospray chamber and therefore shorted to ground. Because the path to ground bypassed the current measurement circuitry in the PPU, there is no measurement corresponding to that telemetry channel—but because the extractor needed to be grounded, the rest of the telemetry channels and data were unaffected.

Of note in Figure 3.9 are Needle Current and Probe Voltage, at approximately 1350 seconds. The slight drop-off in the needle current is mirrored by the probe voltage. Recall that a reduction in positive needle current is associated with a decrease in emitted electrospray. Given this relationship, and the direct correspondence of the fluctuations, it is likely that the drop in probe potential is a result in the drop in electrospray density. This fluctuation occurred at a period of constant probe power output (note the probe voltage reported in these graphs are manually recorded and therefore do not capture rapid fluctuations). It is important to note that when the heater power reaches approximately 2W, the probe potential increases significantly, in both the case with the electrospray on and off. Although the potential to which the probe jumps is different in both cases (due to the presence of the electrospray), the “minimum emission power” for the probe remains the same in both cases.

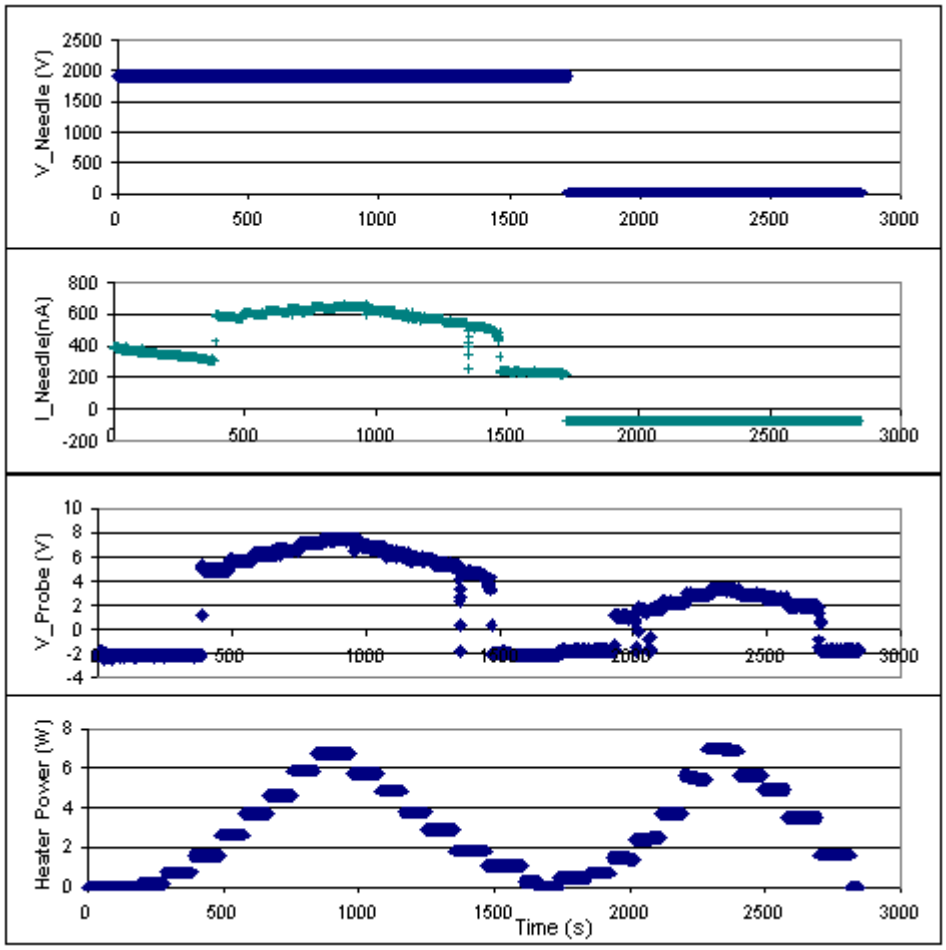

Figure 3.9: Telemetry channels from Case FP3 floating probe test. Heater power uncertainty is ±0.75W, floating potential is at ±0.24V and electrospray and electrospray and extractor currents are accurate to ±3.61nA and ±0.43nA, respectively.

3.1.2: Sweeping Probe Voltage

In a further effort to characterize the plasma potential, we pursued a second method to measure the plasma potential, which involves measuring the current-voltage characteristic of an emitting probe. As discussed in Chapter 2, when using this technique, space charge effects become evident in a rounding of the characteristic near the "knee."

3.1.2.1. Sweeping Probe Voltage—Case VS1

The results of Case VS1, incorporating experimental configuration D (the probe is approximately 7.5cm from the edge of the extractor electrode), are shown in Figure 3.10. The data is presented in a semi-log plot because the Boltzman factor for the density results in a linear function on a semi-log plot (which is why straight lines are fit in order to find the knee). It is difficult to determine any distinctly different behavior of the emitting probe in the presence or absence of an electrospray. The needle voltage was set to the typical 2.0kV and the needle current was stable at approximately 100nA. The "knee" in the current-voltage characteristic was not captured over the range of probe voltages used. Rather, only the right hand side of the I-V characteristic seems to have been captured in this plot. As such, detailed reporting of the electrospray is not shown.

It is important to also note that the distance between the probe and the electrospray in configuration D is roughly comparable (approximately 50% greater distance) to those in case FP1 and FP3. These cases showed a marked difference in probe behavior due to the activation of the electrospray: in this test, we see little or no difference. Given the limited range of the voltage sweep, it is likely that the characteristic "cutoff" point in the I-V characteristic occurs at a potential below those tested in Case VS1.

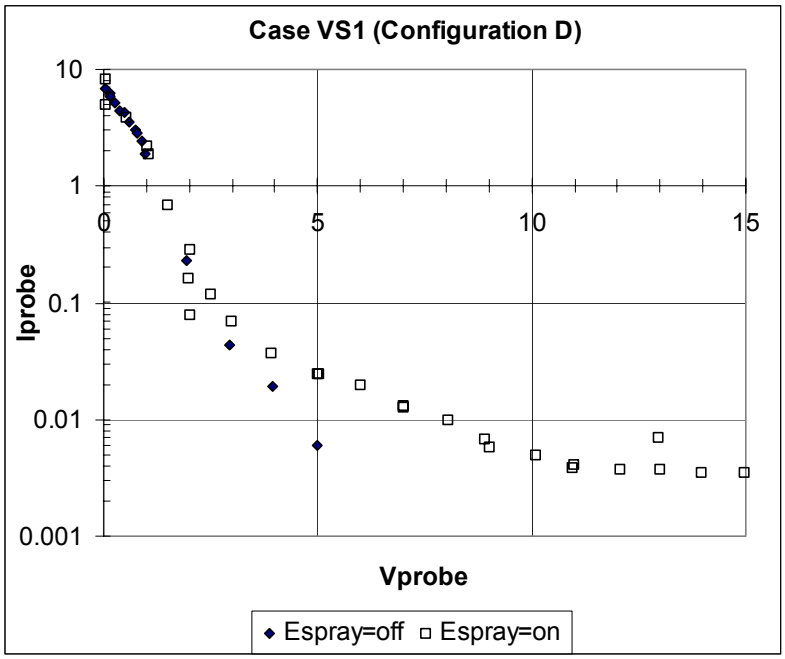

Figure 3.10: Case VS1 in experimental configuration D (probe distance from extractor electrode is approximately 7.5cm). Probe current (μA) uncertainty is within ±20nA, probe potential uncertainty is within ±0.24V.

3.1.2.2. Sweeping Probe Voltage—Case VS2

Case VS2, incorporating experimental configuration D (probe distance from extractor electrode is approximately 7.5cm), uses the sweeping voltage technique in a simple test to determine a rough baseline as to where the "knee" would occur in this system. As such we used the case with the electrospray off in order to reduce the number of variables. We used a different power supply (APH 2000M) for PS1 that enables a much larger range (–300V to +35V). This range was selected because the data in VS1 seemed to indicate the "cutoff" would occur at a negative potential. A typical voltage sweeping I-V characteristic (section 2.2.1) is characterized by the behavior seen in case VS1 but *above* the plasma potential, thereby indicating the need for a larger voltage range.

The results of the larger sweep (Case VS2) can be seen in Figure 3.11, which does indeed indicate a negative cutoff of approximately –4.4V. The trend lines used were exponential fits using the Microsoft Excel software, and are intended to be a rough visual aid only, to highlight the point at which the V-I trace begins to change from an asymptotic value to a nearly constant, negative slope to the right of the knee.

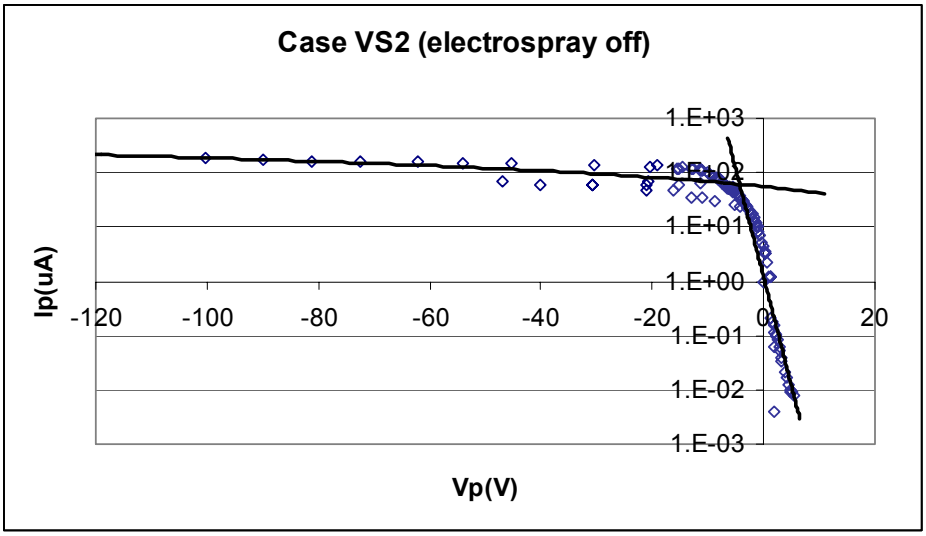

Figure 3.11: Case VS2, with the electrospray off (probe distance from extractor electrode is approximately 7.5cm). The cutoff point occurs at approximately –4.4V. Probe current uncertainty is within ±20nA, probe potential uncertainty is within ±0.24V.

In addition to providing a starting prediction as to where the "knee" would occur with an active electrospray, case VS2 shows similar behavior to case VS1 within the overlapping range of the two tests (0 to +7V).

3.1.2.3. Sweeping Probe Voltage—Case VS3

We repeated the sweeping voltage test a third time, VS3, but this time with the spray on in experimental configuration C, which featured the 90-degree probe mount which allowed visual confirmation of an active electrospray as well as a short distance (approximately 2.7cm) between the probe and the electrospray. Figure 3.12 shows the

results of the sweeping probe test comparing the I-V characteristics of the probe with the electrospray on and off. The data is again presented in a semilog plot, and we again highlight the "knee" of the two components of each I-V characteristic using exponential trend lines in the same way as we did with case VS2. With the electrospray turned off, we see a value similar to that found in VS2 (approximately –3V where case VS2 was approximately –4.4V). With the electrospray turned on, however, the "knee" is a more positive voltage, approximately 2V.

As in the floating probe experiments (FP1, FP2, FP3), we would expect the presence of a positive electrospray to draw more current from an emitting probe, and we observe this in case VS3. The 5V difference corresponds to approximately 479nA more current being drawn from the emitting probe in the presence of the electrospray: the path to ground for the current measurement is 10.43MΩ (given a total of 10.33MΩ in R3 and R4 and a 10kΩ output impedance from the 2V analog output of the Keithly 6514—the path impedance through the isolation transformer and the PPU is on the order of GΩ). The 479nA is on the order of the current increase in probe emission observed for the floating probe experiment at close (approximately 2cm) range.

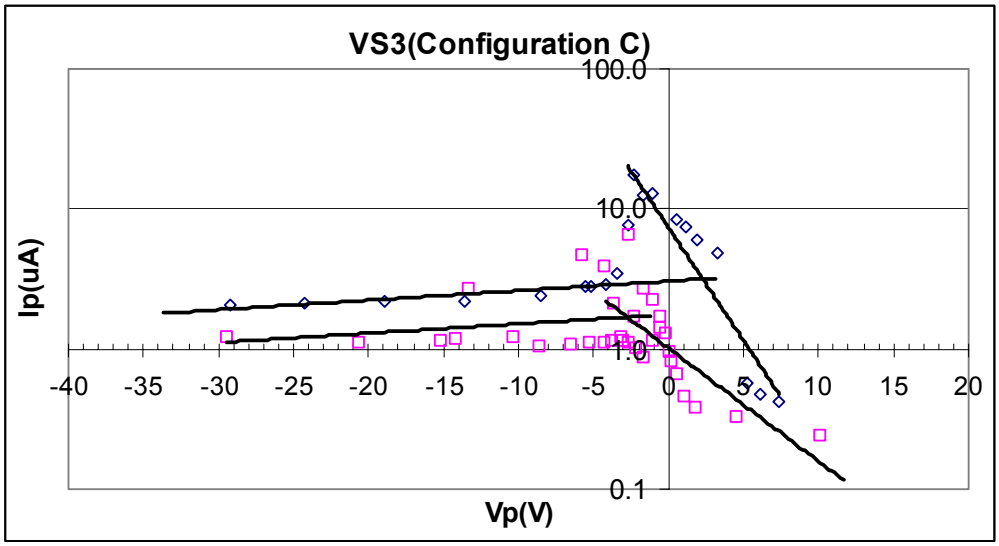

Figure 3.12: Case VS3 V-I characteristic. The pink squares represent the spray turned off, and the blue diamonds represent the spray turned on (probe is 2.7cm from electrospray). Probe current uncertainty is within ±20nA, probe potential uncertainty is within ±0.24V.

At a probe potential of approximately -3V, there is a significant spike in current drawn from the probe both when the electrospray is on and off. This is visible in the I-V characteristic, as well as the electrospray performance data (Figure 3.13). Unstable flowrate (due to bubbles or a corroded tip) into the needle likely contributed to the erratic behavior. We assume a proportional relationship between flowrate and emission current throughout these tests and observe a rough correlation between the two: for example once the electrospray is turned off (needle voltage goes to zero, flowrate stops), the needle current levels off and falls to zero as well.

A second factor that may have contributed to the erratic electrospray current could be changes in the electrospray regime (e.g. from mainly droplet mode to mixed mode to purely ionic in the "highly stressed" regime): images of the different emission cones can be seen in Figure 3.14. Although regime change could partly be influenced by flowrate change, it is also possible that changes in the electrostatic field between the needle and

the extractor were the cause. Once propellant collected on the extractor (which we observed), the propellant would go to the same potential as the extractor. As buildup occurs, the extractor in essence becomes contorted, some parts being closer to the needle—as a result of the deposition—and others being further away—because they are otherwise untouched. The more contaminated the area, the more propellant is deposited, and the more the Taylor cone is stressed.

A third potential contributing factor to the erratic behavior could be the probe: the fluctuations of the needle current seem to directly correlate to those of the probe current. This masking has been observed in earlier tests, and increases in probe emission could impact the needle and therefore affect the needle current. Such increased electron absorption would result in an increase in positive current in the needle telemetry.

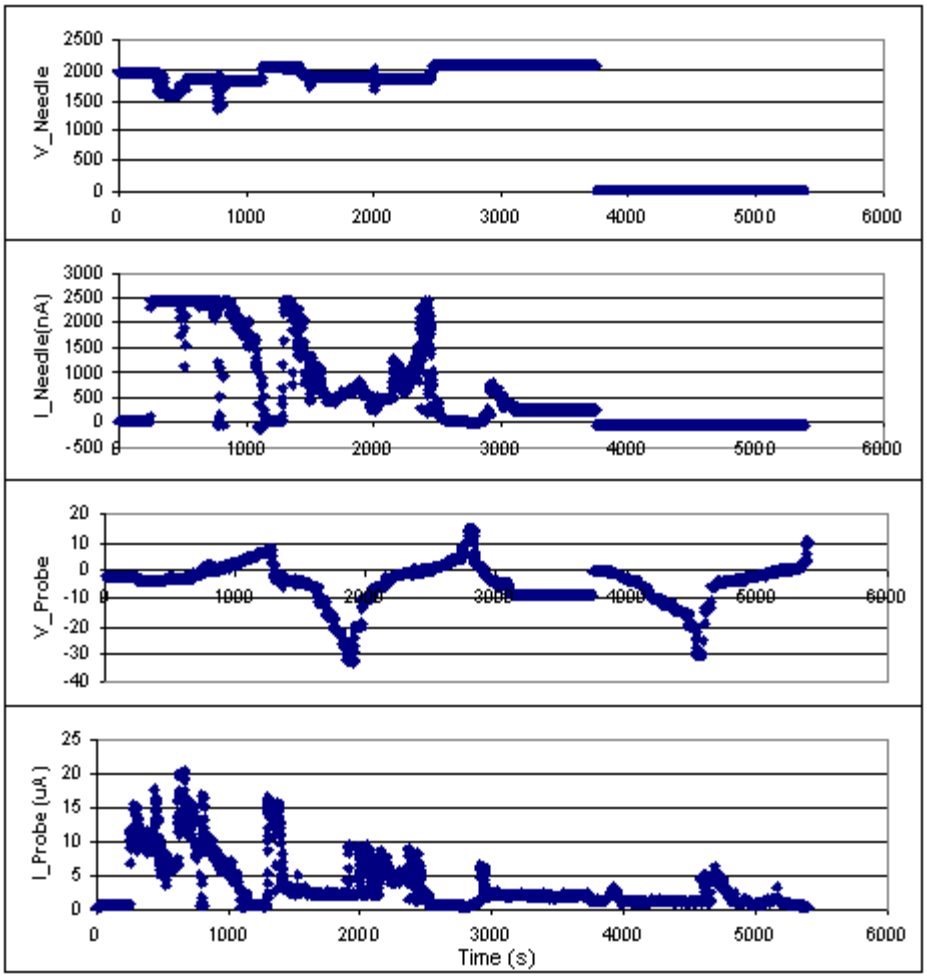

Figure 3.13: Telemetry from case VS3 (configuration C). Needle voltage uncertainty is ±9.63V, needle current uncertainty is ±3.61nA, probe potential uncertainty is within ±0.24V and probe current uncertainty is within ±20nA.

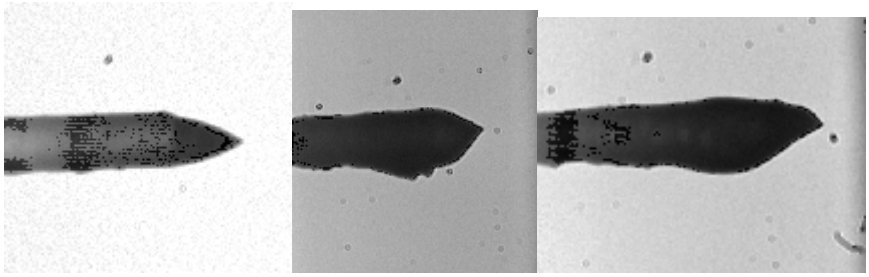

Figure 3.14: Images taken of the emission site during case VS3. Note the formation of the Taylor cone in the middle and right images, indicative of a highly stressed emission.

To help interpret the results of both the floating probe (FP1, FP2, FP3) and voltage sweep (VS1, VS2, VS3) experiments, Chapter 4 presents a numerical analysis of the space-charge limited emission of a probe into a given ambient density following the method developed by Kemp and Sellen[16]. By investigating the sheath surrounding a probe emitting in the space charge limited (SCL) regime, it is possible to estimate the difference in potential between the plasma and the probe floating potential for a given plasma density, electron temperature, wire temperature and emission level. Estimates of the plasma density based on published data for similar electrosprays is also presented in Chapter 4.

3.2 Uncertainty and Error Analysis

The experimental uncertainty, the bounds with which data is reported shall be discussed for each of the sources of data: (1) digital readout from a meter (e.g. Keithley current measurement), (2) readout of a meter directly into the PPU/DAQ system (e.g. Keithly 2V analog output), (3) the product of two or more direct meter measurements (e.g. heater power), and (4) data recorded through the data acquisition system (e.g. needle current). A summary of each of the configurations, the channels recorded, and the methods used to record them, can be found in Table 3.2. Note the data source type is listed in parenthesis after each data source. Also, the resolution and accuracy for a given data range for the Keithly 6514 and the Fluke 83III are summarized in Appendix C. These devices have not been recalibrated, and therefore the calibrations used are those from the factory.

Table 3.2 Configuration and Channel Summary

Configuration	A	B	C	D
Tests	**FP1**	**FP2**	**FP3, VS3**	**VS1, VS2**
Target Current	6514 (1)	6514 (2)	N/A	Fluke 83III (1)
Probe Voltage	Fluke 83III (1)	1/30 Voltage divider out to PPU (4)	1/30 Voltage divider out to PPU (4)	1/30 Voltage divider out to PPU (4)
Probe Current	N/A	N/A	6514 (1)	6514 (1)
Needle Voltage	PPU telemetry (4)	PPU telemetry (4)	PPU telemetry (4)	PPU telemetry (4)
Needle Current	PPU telemetry (4)	PPU telemetry (4)	PPU telemetry (4)	PPU telemetry (4)
Extractor Current	PPU telemetry (4)	PPU telemetry (4)	PPU telemetry (4)	PPU telemetry (4)
Heater Power	HY3005-3 & DMM568-C (3)	HY3005-3 & DMM568-C (3)	HY3005-3 & DMM568-C (3)	HY3005-3 & DMM568-C (3)

Direct Meter Measurements (1)

The Keithley Electrometer (model #6514) was used to directly measure the current of the target. There was no analog output used, so the data was manually recorded from the digital readout. For the typical 20μA range used, the accuracy limit is 0.1% of the displayed value, or within ±20nA. The Fluke 83III was also used in this way, and is accurate to 0.40% of the value measured, or ±8nA for the typical 2μA maximum value of the target current. For the simple measurement of probe voltage (FP1), the accuracy is 0.10% of the displayed value, or within ±10mV for a typical 10V measurement.

Direct Meter Measurements Output to PPU (2)

The Keithly 6514 2V analog output was used to improve data acquisition for the floating probe tests. For the 2μA range used, one μA of measured current corresponds to one volt output. The uncertainty here incorporates contributions both from the uncertainty of the 2V analog output circuitry, as well as from the 6025E card. There was no calibration performed on this channel. The (12 bit) 6025E card has a precision of 4.88mV (±10V →

20V / 2^{12} = 4.88mV). Neither the precision or the accuracy of the 6025E card was independently verified, and this value relies on the accuracy of both the factory calibration as well as the 2V output via which the data is recorded. The 2V analog output is accurate to ±15% of the displayed value, which is the dominant contribution and which we shall take as the uncertainty in this measurement.

Product of two Direct Measurements (3)

The power supply voltage indicator (HY3005-3) is listed as having an accuracy of ±1% for 2 displayed digits. The digital multimeter used to provide a current measurement (DM568-C) does not have a published listing for accuracy. However, we performed a simple test to compare the accuracy of the unknown multimeter with the known NIST-certified Fluke 83III multimeter. The maximum discrepancy in the current monitor mode between the Fluke and the DM was 6mA of the Fluke's displayed value. The maximum discrepancy in the voltage monitor mode between the Fluke and the DM was 0.6V. Using the known uncertainty for the current and voltage, we can use a standard technique to estimate the uncertainty in the power:

$$\sigma_P^2 = P^2\left(\frac{\sigma_V^2}{V^2} + \frac{\sigma_I^2}{I^2}\right), \qquad [3.1]$$

where σ_P^2 is the uncertainty of the power and σ_V^2 and σ_I^2 are the uncertainties associated with the voltage and current measurements, respectively. As the power uncertainty varies with each datum, we conservatively use the maximum calculated uncertainty (corresponding to the largest value of power) as the uncertainty for power. As such we

estimate the uncertainty for the power in the experiments: ±0.82W (FP1-spray off), ±0.69W (FP1a), ±0.79 (FP1b), ±0.83W (FP1c), ±0.75W (FP3), ±0.29W (VS3).

Data Acquisition System-PPU (4)

The telemetry represented by this data type is the needle current, the needle voltage, the extractor current and the probe voltage divider.

Each telemetry channel in the PPU includes a variety of resistors, capacitors and integrated circuits each contributing to the overall measurement uncertainty (section 2.1.5). In the calibration of each channel, the Fluke and Keithley, both with known accuracy and resolution, are used to compare the "actual" value to the "reported" (PPU) value (section 2.1.5 e.g. Figure 2.13). The "least-squares" method was used to create a linear fit to the data. Contained in this linear fit "scatter" is the uncertainty in the PPU and signal conditioning electronics as well as the NI 6025E data acquisition PCI card. This scatter also encompasses the known accuracy limitations of the Fluke 83III and the Keithley 6514 (given that each device for the ranges used is accurate to within 0.1% of the maximum displayed value, this makes a very small contribution to the uncertainty). Therefore the calibration fit provides a means by which to consider all the individual contributions to the total uncertainty.

A conservative, if not crude, estimate for the uncertainty in this data type then is to use the largest difference between a calibration data point and the linear fit. The relevant PPU

channels and the associated largest difference from calibration data are listed in Table 3.3.

Table 3.3: Summary of PPU Channel Uncertainty

Channel	Maximum Difference	Range	Average Difference	Final Uncertainty
Extractor Current	0.430nA	5-100nA	0.315nA	± 0.43nA
Needle Current	3.61nA	5-2000nA	1.34nA	± 3.61nA
Needle Voltage	9.63V	10-2000V	3.13V	± 9.63V
Probe Voltage	0.24V	-30-20V	0.060V	± 0.24V

The second column in Table 3.3 refers to the largest difference between the individual calibration data point and the linear fit. This largest value is (by definition) larger than the average difference between the individual data points and the linear fit. The final uncertainty is crudely estmiated to be within this maximum difference (in the positive and negative direction).

As a means of characterizing the quality of the fit, the r-squared value was also calculated. The r-squared value represents how much of the measured data (in this case, the reported PPU values) falls outside the linear fit. A value of 1 implies complete correlation (via the linear fit), where a value for 0 implies no correlation. For example, an r-squared value of 0.99 means that 99% of the data variation is accounted for by the linear fit. As a means by which to help characterize the quality of the fits, then, the r-squared value has been calculated for relevant PPU telemetry, namely the needle current (r^2=0.9995), needle voltage (r^2=1.0000), and the extractor current (r^2=0.9999). The linear

fit for each channel has a high degree (over 99%) of correlation between the “actual” (Keithly-measured or Fluke-measured) value and the “reported” (PPU) value.

4. Space Charge Current Limit on Emissive Probe

This Chapter presents the analysis performed to estimate how close our plasma potential measurement can get to the actual potential. This information is used to help in understanding the results presented earlier and possible limitation in the use of emissive probes to study colloid plumes. We begin with a discussion of plasma shielding (or sheaths), and how the density of surrounding plasma impacts the emissive characteristics of a plasma probe. We use this to build a mathematical model, based on the work of Kemp and Sellen[16], to predict the potential through the sheath as a function of probe emission strength and plasma density. We then perform an analysis of our experimental work to relate our observations to predicted probe performance.

4.1 Plasma Potential in the Sheath

Chen describes a plasma as "a quasineutral gas of charged and neutral particles which exhibits collective behavior"[26]. The movements of charged particles create changes in local charge that create currents, electric and magnetic fields. These fields can limit the effects of local phenomena, acting like a shield. An example of this phenomenon is Debye shielding. If one were to put a negatively charged sphere in a plasma, positive charges would immediately surround the sphere: in an ideal case (e.g. no thermal motion), there would be just enough positive charges in the surrounding plasma cloud to match the charges in the sphere. The Debye length,

$$\lambda_D \equiv \left(\frac{\varepsilon_o K T_e}{n e^2} \right)^{\frac{1}{2}}, \qquad [4.1]$$

is a measure of the thickness of this ion cloud layer, where ε_o is the permeativity of a vacuum, K is the Boltzmann constant, T_e is the electron temperature, n is the plasma

density and *e* is the electron charge. A plasma sheath is a region adjacent to a surface immersed in a plasma characterized by a gradient in the plasma potential as well as a charge imbalance. The potential gradient (electric field) can act as a barrier to particle motion, depending on the energy and charge of a particle. If an electrode in a plasma is electrically floating, the magnitude of this potential barrier changes so that the number of arriving (or escaping) electrons and ions are roughly the same, thereby maintaining charge neutrality on the electrode.

To illustrate, consider a one dimensional plasma confined by two electrically floating walls. Given their greater mobility, more electrons will hit the walls than ions, leaving the plasma with a net positive charge and the walls with a net negative charge (a biased wall will result in a sheath in which particles will arrive at different rates). The floating wall potential then adjusts to equalize the incident ion and electron fluxes: in this case, the wall will float more positive until it approaches the plasma potential. The wall, then, is analogous to the spherical negative charge in the Debye shielding phenomenon described above. As such, the wall's negative potential will be contained to within a few Debye lengths along any part of the wall that is in contact with the plasma[26].

When the potential of an emissive probe is sufficiently higher than the surrounding plasma, the emitted electrons will be reflected back into the probe (since this results in no net emission, no current will be observed). When an emissive probe emits electrons and has a potential lower than the surrounding plasma, electrons will be absorbed into the plasma and appear to the probe as positive ions arriving. The potential that an emitted

electron sees in the surrounding plasma (due to the space charge) will determine if the electrons are subject to a favorable or adverse potential gradient or electric field. An excessive buildup of negative space charge around an electron-emitting probe will limit emission, and the emission is said to be "space charge limited." The level of emission that can be sustained before this limit depends on the ion density in the surrounding plasma. If the plasma is not sufficiently dense to absorb enough electrons, the escaping current from the probe is reduced as the probe bias approaches the plasma potential (Figure 4.1). The onset of space charge limited emission is characterized by an electric field (potential gradient) of zero at the emitter surface.

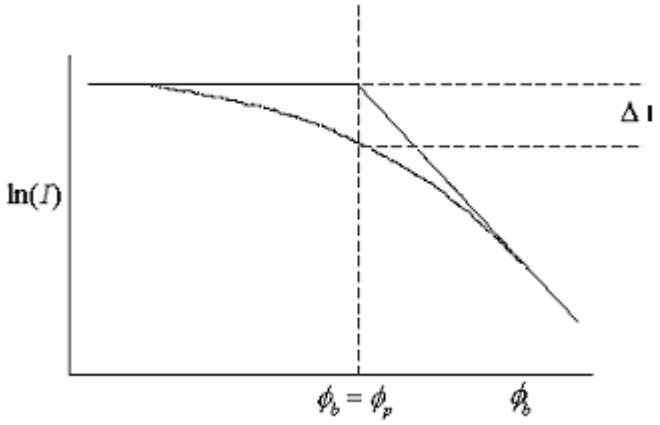

Figure 4.1: Sketch of characteristic I-V curve of voltage sweep technique: the current difference between the SCL case and an non-SCL case is illustrated.

Kemp and Sellen[16] describe the potential distributions around an emissive wire immersed in a plasma. Their method uses a normalized Poisson equation in cylindrical coordinates, which we verify. The Poisson Equation, in cylindrical coordinates, can be written as

$$\nabla^2 V = \frac{1}{r}\frac{\delta}{\delta r}\left(r\frac{\delta V}{\delta r}\right) + \frac{1}{r^2}\frac{\partial^2 V}{\partial \vartheta^2} + \frac{\partial^2 V}{\partial z^2} = -\frac{\rho}{\varepsilon_o}, \qquad [4.2]$$

where V is the potential, ρ is the density and ε_o is the permitivity of a vacuum. Assuming radial symmetry and neglecting all but radial electron motion, we obtain

$$\nabla^2 V = \frac{1}{r}\frac{\delta}{\delta r}\left(r\frac{\delta V}{\delta r}\right) = -\frac{\rho}{\varepsilon_o}. \qquad [4.3]$$

The density term, ρ, is rewritten in terms of the three ion populations:

$$\nabla^2 V = \frac{1}{r}\frac{\partial}{\partial r}\left(r\frac{\partial V}{\partial r}\right) = -\frac{e}{\varepsilon_o}\left(n_i - n_e - n_{ep}\right), \qquad [4.4]$$

where n_i corresponds to the ambient plasma ions, n_e corresponds to the ambiet plasma electrons, and n_{ep} corresponds to the electrons emitted from the emissive probe. For the plasma ions we assume the kinetic energy is much greater than the potential drop through the sheath[16], so their number density remains constant (n_i=n_o). For the ambient plasma electrons we assume Boltzmann statistics:

$$n_{e(r)} = n_o \exp\left(\frac{e\left(V - V_p\right)}{kT_e}\right). \qquad [4.5]$$

Regarding the electrons emitted by the probe, we assume a zero potential at the injection point, meaning all the energy is kinetic (KE = (½)kT_w). Combining this assumption with the conservation of mechanical energy (Eq 4.6) and the conservation of charge (Eq 4.7), we can write the density of electrons emitted by the probe (Eq 4.8).

$$\frac{1}{2}kT_w = \frac{1}{2}mv_{e(r)}^2 - eV_{(r)}, \text{ with } v_{ew} = \sqrt{kT_w / m_e} \text{ at r=r}_o \qquad [4.6]$$

$$i = const = en_{ep(r)}v_{e(r)}2\pi rl = en_{ep\_w}v_{e\_w}2\pi r_o l \qquad [4.7]$$

$$n_{ep(r)} = \frac{n_{ep\_w}r_o}{r\sqrt{\frac{2eV}{kT_w}+1}} \qquad [4.8]$$

We substitute each of these values (Eq 4.6-4.8) into Eq 4.4:

$$\nabla^2 V = \frac{1}{r}\frac{\partial}{\partial r}\left(r\frac{\partial V}{\partial r}\right) = \frac{-\rho_o}{\varepsilon_o}\left[1 - \exp\left(\frac{-e(V_p - V)}{kT_e}\right) - \frac{\rho_{ow} r_o}{\rho_o r\sqrt{\frac{2eV}{kT_w} + 1}}\right], \qquad [4.9]$$

given $\rho_o = en_o$ and $\rho_{ow} = en_{ep\_w}$.

The inclusion of plasma electrons, in addition to the plasma ions and emitted electrons from the probe, follows the model developed in the work of Kemp and Sellen. Originally, our experiments were to have included a neutralizer cathode that would have produced a population of plasma electrons more typical of electrostatic thruster plumes. The numerical analysis of the space charge limited emission through the sheath was intended to model this case. The numerical results presented in this chapter include a plasma electron density term even though the cathode ended up not being used in our experiments. Because of this we expect the point at which emission strength becomes space charge limited (for a given plasma density and sheath potential drop) in our experiments to be higher than predicted by these calculations. The absence of a plasma electron population should allow more probe electrons to be extracted before the space charge limit is reached.

A second difference will correspond to the shape of the potential variation through the sheath. In the model, the density of emitted electrons falls off while the plasma electron approaches a constant value (equal to the ion density) far from the probe. This insures that the potential asymptotically approaches the plasma potential with increasing distance from the probe. In the absence of plasma electrons, the potential will not approach a constant value, suggesting the sheath will extend to adjacent surfaces in the chamber.

Therefore, in light of the fact a neutralizer cathode was not used in these experiments, the results from the numerical sheath calculations should be interpreted as establishing the limit at which space charge rounding in the probe I-V characteristic is likely to occur for colloid thruster plumes in which an plume electron population is present.

For convenience we wish to non-dimensionalize our form of the Poisson equation using the following parameters: $\xi\left(\equiv\frac{eV}{kT_w}\right)$ is the normalized potential; ξ_p is the normalized plasma potential; $\theta\left(\equiv\frac{r}{r_o}\right)$ is the normalized radial position; $B\left(\equiv\frac{T_w}{T_e}\right)$ is the ratio of the wire temperature to the plasma electron temperature; $C\left(\equiv\frac{e\rho_o r_o^{\,2}}{kT_w\varepsilon_o}\right)$ is a normalization constant, and $A\left(\equiv\frac{\rho_{ow}}{\rho_o}\right)$ is the ratio of space charge density of at the wire surface due to emitted electrons relative to the ion space charge density.

Parameter A is related to thermionic emission strength i/l by writing the current (in amps) as

$$i = j2\pi r_o l\,, \qquad [4.10]$$

where i is the current, j is the current density of emitted electrons, l is the filament length and r_o is the wire radius. The current density j can also be expressed $j = en_e v_e$. Kemp and Sellen assume electrons are injected with the kinetic energy equal to the

thermal energy of the electrons at the filament temperature, $E = \frac{1}{2} kT_w$ which allows us to write the electron velocity as $v_e = \sqrt{\frac{kT_w}{m_e}}$. Substituting, we can re-write Equation 4.7 as

$$\frac{i}{l} = en_e 2\pi r_o \sqrt{\frac{kT_w}{m_e}}. \qquad [4.11]$$

In terms of the parameter $A = \frac{\rho_{ow}}{\rho_o} = \frac{en_e}{en_o}$, we can rewrite the above as

$$\frac{i}{l} = An_o r_o 2\pi \sqrt{\frac{kT_w}{m_e}} = A\left(n_o r_o\right) 1.9596 \bullet 10^{-13}, \qquad [4.12]$$

with n_o (m^{-3}) and r_o (m). This allows us to convert calculated, non-dimensional values of A into the more convenient units of amps per meter.

Given the non-dimensional parameters described above, the Poisson equation can continue to be developed. The left hand side of Equation 4.9 is written in terms of $\xi\left(\equiv \frac{eV}{kT_w}\right)$ and $\theta\left(\equiv \frac{r}{r_o}\right)$ resulting in:

$$\frac{kT_w}{er_o^2}\left(\frac{\partial^2 \xi}{\partial \theta^2} + \frac{1}{\theta}\frac{\delta \xi}{\delta \theta}\right) = \frac{-\rho_o}{\varepsilon_o}\left[1 - \exp\left(-\frac{T_w}{T_e}(\xi_p - \xi)\right) - \frac{\rho_{ow}}{\rho_o}\frac{1}{\theta\sqrt{2\xi + 1}}\right], \qquad [4.13]$$

given $\frac{dV}{dr} = \frac{kT_w}{er_o}\frac{d\xi}{d\theta}$ and $\frac{d^2V}{dr^2} = \frac{kT_w}{er_o^2}\frac{d^2\xi}{d\theta^2}$. We further refine Eq 4.13 by substituting the above definitions for A, B and C to obtain the final non-dimensionalized Poisson Equation:

$$\frac{\partial^2 \xi}{\partial \theta^2} + \frac{\delta \xi}{\theta \delta \theta} = -C\left\{1 - \exp[-B(\xi_p - \xi)] - \frac{A}{\theta\sqrt{2\xi + 1}}\right\}. \qquad [4.14]$$

At the onset of space charge limited emission, without the formation of the virtual cathode, the electric field at the wire surface will be zero. At a great enough distance from the emitting wire, the potential ξ will not change but be asymptotic to ξ_p. As such, we write the following boundary conditions:

$$\theta = 1 \begin{cases} \xi = 0 \\ \dfrac{\delta\xi}{\delta\theta} = 0 \end{cases}, \quad \lim_{\theta\to\infty} \xi = \xi_{p.} \qquad [4.15]$$

Equation 4.14 is solved for ξ and a bisection method† is used to determine the value for A (related to the thermionic emission strength i/l via Equation 4.12) that satisfies the boundary conditions. We pick a value for Parameter A, integrate along θ, and then check if Equation 4.14 is satisfied: if it is not, the guess for A is modified. Figure 4.2 shows a sample solution.

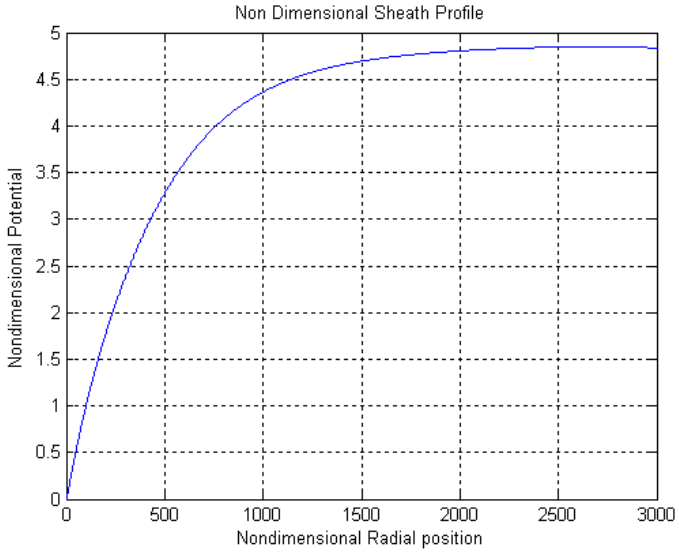

Figure 4.2: Typical results showing the solution to ξ. Note θ (theta) begins at the nonzero point equivalent to $r = r_o$. For the case shown, ξ_p=5, $n_o = 10^5 cm^{-3}$, r_o=0.00381cm, T_w=T_e=2500K and i/l = 7.95μA/cm.

† Personal communication from Prof. J. Blandino to T.Roy. Code sent via email sent January 1, 2005. The code is listed in Appendix E.

We first seek to check our solution to the non-dimensional Poisson Equation by confirming that our results very closely match those of Kemp and Sellen[16]. After we confirmed the consistency of our calculations, we modified some of their parameters to more closely reflect our experimental conditions. For example, Kemp and Sellen use a 25μm diameter tungsten filament and we have a 75μm diameter filament. We assume $T_w=T_e=2500K$ for the sake of comparison as Kemp and Sellen assume this temperature in their calculations. This temperature is consistent with the fact that no tungsten filaments melted during these tests (melting point of Tungsten is 3695K).

Each appropriate solution of the potential yields a value for A, which becomes one point of the implicit function A (ξ_p, C) which physically represents the emission strength and potential fall through the sheath for a given filament temperature, electron temperature, wire radius, and plasma density. The emission strength (i/l) of the wire (of radius r_o), corresponding to the onset of the space charge limited regime (e.g. onset of rounding in Figure 1.4), is plotted as a function of various ion number densities (n_o) and normalized sheath potential drops in Figure 4.3. Since the probe is taken to be at a potential of zero, the normalized plasma potential ξ_p (in Figure 4.2) represents the potential drop across the sheath that is created from the difference between the probe bias potential and the surrounding plasma potential (which can be visualized in the plot of Figure 4.2 above).

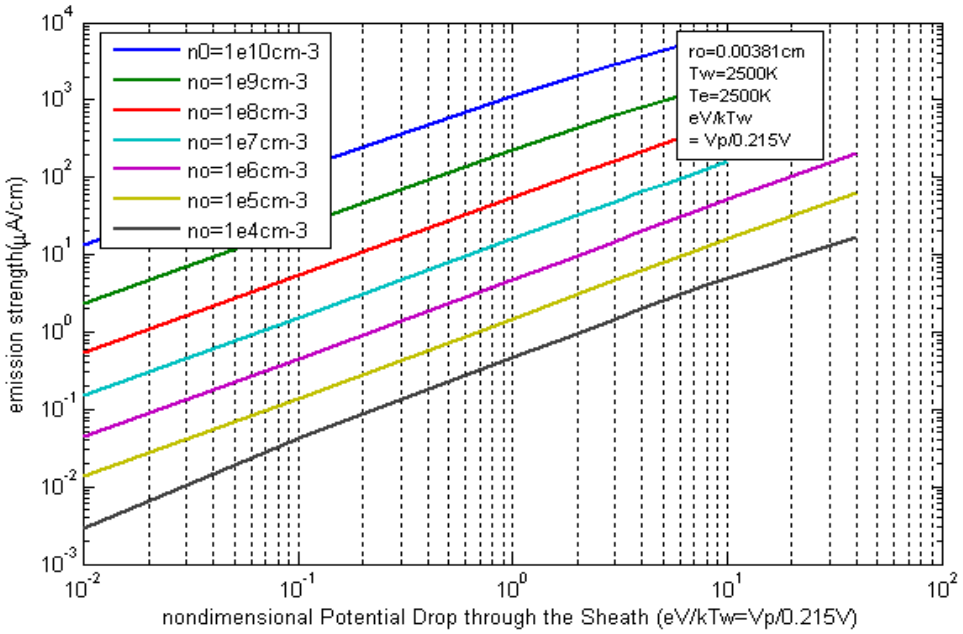

Figure 4.3: Space charge limited emission from probe as a function of potential difference and surrounding plasma density.

It is useful to discuss a lower limit in plasma density for the effective use of an emissive probe (assuming r_o=0.00381cm and T_W=T_e=2500K). This lower limit is due to space charge rounding of the probe's characteristic I-V curve (e.g. Figure 1.3), where the magnitude of the rounding (Figure 4.4) represents how close a measurement can get to the "actual" plasma potential (which is the knee in the I-V curve).

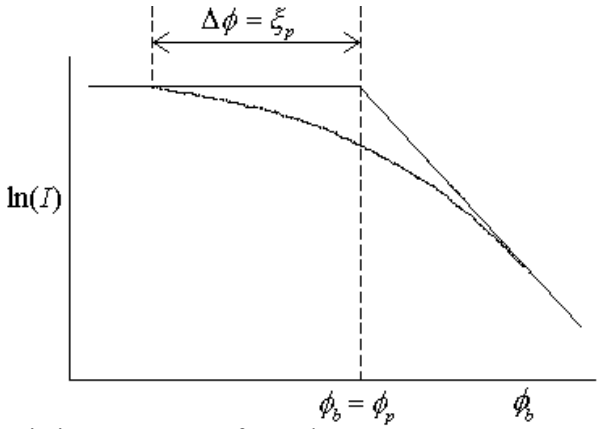

Figure 4.4: Characteristic I-V curve of a voltage sweep measurement of the plasma potential (occurring at the "knee" in the plot), illustrating the potential drop across the sheath.

So for an accuracy in potential measurement of ~0.01V (ξ_p=0.01V/0.215V=0.047), at a minimum useful emission strength of 1μA/cm (Kemp and Sellen[16] report emission below 1μA/cm isn't very useful) the lower limit in plasma density would be 10^7 ions/cm^3 (Figure 4.3). This emission strength yields ~0.1V accuracy at a plasma density of 10^5 ions/cm^3, and ~1V accuracy at a plasma density of 10^4 ions/cm^3.

In the next section (4.1.2) we estimate ion density for the different tests, which we estimate to range from 10^3ions/cm^3 to10^6ions/cm^3 for our experimental environment. The emitting probe technique is limited by low plasma densities, and this limitation begins to become apparent at densities as low as 10^5cm^{-3}.

4.2 Estimated Values for Experimental Plume Parameters

The density of ions, or in our case droplets, is not measured directly. In this section we estimate the density of positively charged droplets by applying mass and charge conservation and using published data for similar electrosprays. The mass flowrate, which is the product of mass density and volumetric flowrate, can be used to estimate the number density of droplets in the plume. Assuming the plume can consists of two droplet populations, the number density of each population can be expressed as

$$n_1 = \frac{\dot{m}_1}{m_1 v_1 A_c}, n_2 = \frac{\dot{m}_2}{m_2 v_2 A_c}, \qquad [4.16]$$

where $\dot{m}$ is the mass flowrate, m is the mass of a droplet, v is the velocity of the droplet, and A_c is the cross sectional area along the electrospray plume under consideration. Subscript 1 refers to the main population; subscript 2 refers to the satellite droplets. Main and satellite droplets for this fluid have been observed via the time of flight (TOF)

technique by Gamero and Hruby[18]. Since only A_c is directly measured in our work, the remaining factors must be calculated using indirect measurements. In this estimation, we use the data from previous work by Gamero-Cataño and Hruby[18], who used time-of-flight and energy analysis techniques to characterize the main and satellite droplets for electrospray solutions of the same composition and electrospray current of the same order of magnitude. Their measurements included the total flowrate, total current, needle potential and specific charge of the main and satellite droplets. Their measurements were sufficient to calculate the remaining factors data[18] (see Appendix E for the calculations as completed using Maple v.6).

To understand how the droplet velocity, which appears in Equation 4.16, is determined, it is critical to understand the energy and potential changes that occur at the different stages of the electrospray process. Figure 4.5 shows an energy diagram that qualitatively represents the energy of the droplets at key points in their path from needle to a collector or target. The important positions are distinguished by vertical dotted lines labeled N (needle), T (transition region), B (breakup point), E (extractor), and C (collector). The horizontal dashed lines represent the electric potential energy at different points along the droplet path.

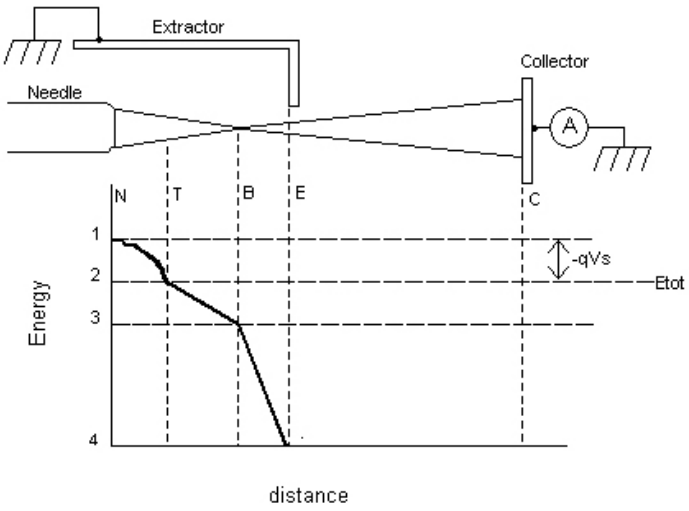

Figure 4.5: Energy diagram illustrating potential energy along droplet path.

At V_N, the fluid has an energy associated with the needle potential (V_N) with respect to facility ground. In the first part of the cone (V_N to V_T), internal electric fields grow with increasing proximity to the extractor electrode. Based on the model by Gamero,[18] as the liquid moves closer to the extractor, the charge from the inner part of the cone is drawn to the surface until the vast majority of the current is transmitted via convected surface charge. This 'charge transition' results in an irreversible energy loss and potential drop, as none of the energy loss is used to accelerate the liquid. In the terminology of Gamero[18], the irreversible losses define the "stopping potential", $V_s = V_N - V_T$. After this point, energy changes are reversible, and the total mechanical energy remains constant. The potential difference between the needle and the point after which all remaining voltage drop is available for acceleration of the fluid (through reversible processes) is aptly named the acceleration potential. The acceleration potential is equal to the difference between the initial potential V_N and the stopping potential, V_S:

$$V_{acc} = V_N - V_s. \qquad [4.17]$$

After the droplets are accelerated, the velocity of the particles can be changed by the collector potential: if the collector is also grounded, the droplet velocity will remain the same; if the collector potential is raised, the droplets will have a lower velocity when they reach the collector; if the collector is brought to the same potential as that associated with point V_S, no current will reach the collector and the droplets are essentially stopped. The stopping potential (and therefore the accelerating potential) is then determined by noting the collector potential at which the collector current diminishes to zero. Once the acceleration potential is determined, one can determine the droplet velocity that is required in order to determine the density (where density is a function of mass flowrate, velocity, particle mass and cross sectional area).

When an electrospray is active, then interrupted at a particular time, the beam is "cut off" from the needle and travels to the collector. The collector current is recorded as a function of time. The resulting time-of-flight wave allows one to calculate the specific charge of the droplets as a function of the velocity of the droplets (length traveled divided by time-of-flight, t_f) and V_{acc}. Specific charge (q/m), time of flight (t_f) and V_{acc} are related by

$$\frac{q}{m} = \frac{1}{2(V_n - V_s)}\left(\frac{L}{t_f}\right)^2, \qquad [4.18]$$

where L is the length of the path of the time of flight. The squared term is of course the droplet velocity. Equation 4.19, then allows one to calculate the velocity from a data set including V_n, V_s, and $\frac{q}{m}$. The following calculations are only meant to be an approximation, as our needle currents were on the order of 300nA and our mass flowrate

was unfortunately not measured. The data are comparable, however, in that the propellants were the same, and the acceleration potential was within 15%. The most relevant published electrospray data is the TBP1 (which matches our solution—2.9% EMI-Im by weight in TBP) solution with the flowrate of 1.16 x 10^{-12} and total current of 54nA described by Gamero[18]. Using this data we calculate v_1 = 352m/s and v_2 = 667m/s.

Gamero used combined TOF and data from a capacitance based, charge detection mass spectrometer to determine droplet specific charge and diameter. In his measurement of specific charge and droplet diameter he studied two different mixtures under several flowrates. His TOF data was more extensive; he studied three additional mixtures under several flowrates each. Assuming we have the same droplet specific mass as his TBP1 mixture, we estimated the droplet mass flow by solving the two following equations simultaneously:

$$I = \dot{m}_1 \left(\frac{q}{m} \right)_1 + \dot{m}_2 \left(\frac{q}{m} \right)_2 \qquad [4.19]$$

$$\dot{m}_{tot} = \dot{m}_1 + \dot{m}_2 \,, \qquad [4.20]$$

Resulting in values of $\dot{m}_1$ = 1.11x10^{-9}kg/s and $\dot{m}_2$ = 2.39 x 10^{-11}kg/s. The plume is assumed to be conical with a 30 degree half angle[18]. Based on this assumption, and based on our measured axial distance between the electrospray origin and the probe for 5.25cm, we calculate the cross sectional area to be 0.00289m^2.

In determining the mass, we use values for $\frac{q}{m}$ and q from Gamero's published data[18]. The charge-to-mass ratio is experimentally determined, however the charge itself is not

measured for this particular fluid (TBP1, in Gamero's data set), so q had to be calculated indirectly. The charge for the droplet is given by Equation 4.21 below[28]. Note that in order to calculate the charge, the droplet diameter must be determined. Equation 4.22 relates droplet diameter to droplet charge† , thereby allowing us to simultaneously solve two equations with two unknowns. We determine D = 2.67 x 10^{-7}m and q_m = 4.28 x 10^{-16}C, resulting in a calculated droplet mass of 9.78 x 10^{-18} kg.

$$q_m \approx 0.7q_r = 0.7\left(\pi\sqrt{8\gamma\varepsilon_o D^3}\right) \quad [4.21]$$

$$D = \left(\frac{m}{q}\frac{6}{\rho\pi}q\right)^{1/3} \quad [4.22]$$

The calculations determining the droplet diameter and charge were verified using additional data sets (for solutions of TBP2 and TBP4) where values for charge and droplet diameter were experimentally determined by Gamero[18].

Recall Equation 4.16, where number density is a function of mass flowrate, cross-sectional area, droplet mass and droplet velocity. As we have just determined each of these factors, the main droplet density can then be approximated as n_1 = 1.11x10^8m^{-3}, (1.11x10^2 droplets/cm^3) and the satellite droplet density as n_2=3.45x10^7m^{-3} (34.5 droplets/cm^3). Given the greater number and larger charge of the main droplets, as well as for simplicity, we consider only the main droplets. The distance between each particle in an even distribution (a good approximation of average distance in a statistically random distribution) is known as the characteristic length, which is given as $L_c = n^{-1/3}$, or in this

† Personal communication between M.Gamero and T.Roy at Busek in October 2003 in which Gamero related an observation that the droplet charge was approximately 70% of the Rayleigh limit, q_r. The Rayleigh limit is the maximum charge a droplet can hold before it breaks apart.

case it is 2.1 mm for the main droplets. The relevance to our calculations summarized in Figure 4.3 is that we have approximated the density of our experimental electrospray, which gives us enough information (in addition to observed probe emission strength) to estimate the potential drop across the sheath.

This information is critical in assessing whether the low droplet density will influence the probe emission (and therefore enable some measurement of the plasma potential). Our density estimate implies the space charge limitations would be so great (extrapolating from Figure 4.3), that there would be little difference between the presence or absence of our electrospray in a plasma potential measurement. We also note that the electric potential at the droplet surface, which falls off as r^{-1}, is reduced by 90% at a distance of 1.3μm (~50 droplet radii). So at the typical 2.1mm separation, the charge potential, reduced by 99.993%, would not exert a significant electrostatic influence over other droplets. Our data (Figures 3.1, 3.7 and 3.12) seem to indicate a marked increase in current leaving the probe in the presence of the electrospray. As such, either our data is inaccurate, or our density estimate is inaccurate. In Chapter 3 we estimated the uncertainty in our measurements, and it is important to recognize the uncertainty in the previous calculation.

The previous set of density calculations was done with a self-consistent and comparable data set[18] to provide estimates of our electrospray density, charge and droplet diameter. These estimates can be improved. In particular, the total mass flowrate in the above calculation ($\dot{m}$ =1.132x10^{-9}kg/s) is a function of specific charge and emitted current—

because we did not measure specific charge, it's difficult to estimate the uncertainty in the mass flowrate. An alternative estimation of the mass flowrate takes advantage of experimental observations to obtain a more reliable estimate. Each of the experimental configurations in this work employed a Pyrex reservoir in which the capillary needle was dipped. We present the mass flowrate in terms of pressure drop across the needle[30]:

$$\Delta P = f\left(\frac{L_N}{d}\right)\frac{v^2}{2}\rho, \qquad [4.23]$$

where ρ is the density, v is the velocity of fluid, L_N is the length of the needle, and d is the diameter of the needle. The friction factor for laminar flow (assuming the fluid is incompressible, constant viscosity, neglecting end effects, axial symmetry and $Re <$ 2000) as[30]:

$$f = \frac{64}{R_e} = \frac{64\mu}{\rho v d}, \qquad [4.24]$$

where Re is the Reynolds number and μ is the viscosity of the liquid. Substituting the friction factor in Equation 4.23, we obtain[30]:

$$\Delta P = \left(\frac{32\mu}{\rho d}\right)\frac{L}{d}\rho v. \qquad [4.25]$$

Given the substitutions for mass flowrate ($\dot{m} = \rho v A$) and the area ($A = \pi d^2/4$), we can put the pressure drop in terms of the mass flowrate, or:

$$\dot{m} = \frac{\Delta P \rho \pi d^4}{128\mu L}. \qquad [4.26]$$

The pressure drop in the propellant reservoir was typically on the order of one atmosphere (1.01325x10^5 Pa), the needle diameter was d = 100μm, L = 0.6096m, ρ = 976kg-m^{-3}, μ = 0.00359Pa-s^{-1}. The fluid properties are those for pure TBP taken from Gamero[18]. The mixture used in our test had the same 2.9% (by weight) concentration of EMI-Im in TBP as was used by Gamero[18]. We obtain a mass flowrate of 1.109x10^{-7} kg/s,

roughly two orders of magnitude larger than used in the calculation. Incorporating this value in the calculation for density, we obtain a density (note the other calculations are identical, as they are not a function of mass flowrate) of 1.377×10^{11} ions/m^3 or 1.4×10^5 ions/cm^3. We further improve the density calculations by using the average needle current for each of the tests, instead of a typical distance of 5.25cm (the density decreases as the spray diverges with axial distance from the source). Because the electrospray density diverges with axial distance, which varies for each test, the density and other relevant parameters are calculated separately for each test (Table 4.1). The density is the final factor required to utilize Kemp and Sellen's model (Figure 4.3) to estimate the limits on the emissive probe because of space charge effects given the electrospray conditions. We shall discuss the individual tests and space charge limitations in more detail later (Chapter 5), but recall that Kemp and Sellen suggest diminished accuracy of plasma potential measurements for densities lower than 10^5ions/cm^3 and emission levels 5μA/cm and below, both of which characterize our experimental conditions.

Table 4.1*:* Summary of tests and electrospray characteristics.

Test	I/L (μA/cm)	density	potential drop (nonD)	potential drop (V)	Vp (measured)
FP1A	5	3.45E+06	0.8	0.172	8.3
FP1B	5	5.15E+04	6.0	1.29	7.5
FP1C	5	1.34E+04	10.0	2.15	7.0
FP3	5	5.08E+04	6.0	1.29	5.0
VS3	5	5.01E+04	6.0	1.29	2.0

Aside from low ion density, the electrospray droplet distribution is disperse enough so as not to behave as a plasma in the sense that the electrostatic influence between droplets is very small. Let's examine case FP1A. This density results in an estimated characteristic length of 66.2 μm. The electric potential at the droplet surface, which falls off as r^{-1}, is

reduced by 90% at a distance of 13.4 μm (~50 droplet radii). So at the typical 66.2 μm separation, the charge potential, reduced by 99.79%, would not exert a significant electrostatic influence over other droplets. The rest of the test cases involve even less electrostatic influence between droplets. Again, as these numbers are based on the droplet diameter, which is itself a function of specific charge, there is a significant amount of uncertainty in this estimation. Indeed the mass flowrate predicted in the first estimate (based on the specific charge in Gamero's comparable data[18]) varied from the second estimate (based on the pressure drop across the needle) by 22%. Even if we pass this uncertainty to the calculations for droplet diameter, however, our results for the radius at which the charge drops by 90% will scarcely be changed (droplet diameter << characteristic length).

Additional information about the sheath can be obtained from a known plasma density. The solution in Figure 4.2 represents a measure of the sheath size. We take a standard point of comparison of varied solutions to the Poisson Equation. This is the point (expressed as a multiple of probe radii) at which the calculated potential reaches 90% of the potential drop through the sheath, which is representative of the sheath size. The sheath size is inversely proportional to the density of the surrounding plasma, as summarized in Table 4.2.

Table 4.2: Summary of calculated sheath radii for various plasma densities.

Plasma Density	Avg # Probe Radii @ 90%	Sheath Radii (cm)
$n_o = 10^{10} cm^{-3}$	30	0.11
$n_o = 10^{9} cm^{-3}$	100	0.38
$n_o = 10^{8} cm^{-3}$	250	0.95
$n_o = 10^{7} cm^{-3}$	350	1.33
$n_o = 10^{6} cm^{-3}$	850	3.24
$n_o = 10^{5} cm^{-3}$	1200	4.57
$n_o = 10^{4} cm^{-3}$	4000	15.24

The length of each filament is approximately 0.4cm, in a looped configuration, with approximately 0.1cm separating each side of the loop. As such, the sheath from one side of the loop overlaps with the other side for all of our experimental conditions, complicating the interpretation of the sheath calculation. Indeed, in order for this overlap to be avoided, the plasma density would need to be $1x10^{10}$ ions/cm^3 or greater. The next chapter uses the analytical results (Chapter 4) to interpret our data (Chapter 3) and determine the extent to which space charge limitations impact plasma potential measurements.

5 Summary and Recommendations

5.1 Summary of Experimental Results

The analytical model of the emissive probe and its environment developed in Chapter 4 provides an important tool with which to interpret the emissive probe data reported in Chapter 3. Recall that ξ_p is not a plasma potential measurement with respect to ground. Rather, it is the potential drop (in its non-dimensional form) through the sheath surrounding the probe, which is the difference between the plasma potential (to be measured) and probe bias potential.

Figure 4.3 is a powerful tool that summarizes the relationship between emission strength of the tungsten filament operating in a space charge limited regime, the potential fall through the sheath, and plasma density, including the density of our colloid plume (Table 4.1). Figure 4.3 helps us to determine if the measured plasma potential in each of the experiments is actually the plasma potential or if the probe is operating in a space charge limited regime.

To illustrate, we take the "plasma potential" measured in one of our experiments and determine the corresponding non-dimensional value, ξ_p (for our assumed $T_w=T_e=2500K$, $\xi_p = V_p / 0.215V$). We then find the corresponding emission strength (plotted as i/l) along the curve for the relevant density (e.g. $n_o = 10^6 ions/cm^3$ for case FP1A). This point is the maximum emission for this density before which SCL effects begin. If the emission strength in our experiment is less than this value, SCL effects begin to reduce the accuracy of the plasma potential measurement; if the observed emission strength is

greater than this value, then SCL effects are not affecting the measurement. We seek to estimate the magnitude of any uncertainty due to space charge limits by using the observed emission strength to find the associated ξ_p, as the corresponding potential drop provides an estimate of how close to the plasma potential the measurement is before space charge rounding impedes the measurement. The results for each of these tests cases are summarized in Table 5.1.

Table 5.1: Summary of test case criteria for determining space charge limitations in plasma potential measurements.

Test	I/L (μA/cm)	density	potential drop (nonD)	potential drop (V)	Vp (measured)
FP1A	5	3.45E+06	0.8	0.172	8.3
FP1B	5	5.15E+04	6.0	1.29	7.5
FP1C	5	1.34E+04	10.0	2.15	7.0
FP3	5	5.08E+04	6.0	1.29	5.0
VS3	5	5.01E+04	6.0	1.29	2.0

In the sweeping probe measurement, the filament emission was kept constant while the probe bias potential was varied. The colloid performance and probe current were monitored. In case VS3 (Figure 3.12), the knee in the emissive probe sweep cases gives an approximate value for the plasma potential. The measured emission strength of the probe is 5μA/cm. We locate the point in Figure 4.3 along the y-axis and move along the x-axis until we reach the appropriate set of solutions for the density of 10^4ions/cm^3. This point corresponds to a value for ξ_p=6.0. Recall ξ_p is the non-dimensional potential drop across the sheath due to space charge rounding, and this represents how close we can come to the plasma potential, or "knee" in the I-V curve of sweeping probe voltage. ξ_p=6.0 corresponds to 1.29V, meaning for the given measurement or knee at 2.0V, space

charge rounding in our experiment only allowed us to get within 1.29V of the plasma potential.

In the floating probe potential test, the probe emission strength was varied while the probe potential was allowed to float. The plasma potential is determined from the maximum value of the floating potential (e.g. Figure 1.2). Because it is strongly emitting, it is SCL by design; however, the probe should still float to within the sheath potential drop of the plasma potential (ξ_p in Figure 4.3). For the strongly emitting case, however, there will likely be a virtual cathode such that the values in Figure 4.3 do not necessarily represent the true sheath limits. Because of the sheath drop given by Figure 4.3 represents the limiting case where the SCL starts to become significant, Figure 4.3 is at best an approximation of how "close" one can get to the plasma potential for floating probe tests. In case FP1 (Figure 3.1), the presence of the colloid plume resulted in an increase in floating probe potential from approximately 4.4V to 8.3V. The current through the impedance to ground (e.g. 830nA in case FP1 through 10MΩ) doesn't account for current that is reflected back into the probe if the probe is space charge limited. Unlike the sweeping probe tests, there were no direct probe current measurements taken during the floating probe tests. We use the measured emission strength from the sweeping probe tests to estimate the emission strength for the floating probe. This is justified because the same probe was used for both types of tests, and the experimental conditions were very similar (e.g. heater power, plasma density, probe area). The observed emission strength is taken to be 5μA/cm (Table 5.1).

To estimate how close to the plasma potential our floating probe measurements are likely to be, we take our estimated value of emission strength (5μA/cm) and density ($3.45x10^6$ions/cm^3 in case FP1A) and find the corresponding value of the potential drop across the sheath, ξ_p=0.8 (which corresponds to 0.172V). According to this, we can get within 0.172V of the measured 8.3V plasma potential. Cases FP1B, FP1C and FP3 (Figure 3.7), are carried out in a similar way, and those results are listed in Table 5.1 . The measurements indicate the plasma potential to be 7.5V within 1.29V, 7.0V within 2.15 and 5.0V within 1.29V, respectively.

5.2 Conclusions and Recommendations

Before our analytical tool was developed, it was expected the floating probe measurements for case FP1A, FP1B and FP1C would be measurably different because the probe was located at varying distances (and plume densities) along the plume: the more diffuse the plume, the less probe current it could extract in order to reach the plasma potential. Instead, there seemed little difference in the emissive probe's I-V characteristic among the cases. It is likely the density variations, resulting from changes in the probe distance, were not sufficient to alter the plasma potential by a discernable amount despite predictions earlier in this report to the contrary.

As our analysis showed, probe sheath dimensions are determined primarily by surrounding plasma density (Table 4.2). For all the test cases the plumes were so diffuse that the sheath grew to result in each part of the filament would lie within the sheath of another part. It is not desirable to have the probe folded within its own sheath, as the plasma density and energy distribution within the sheath will not necessarily be

representative of the plasma outside the sheath. The numerical calculations for the Poisson equation, for a given plume density and sheath drop, determine the emission strength limit beyond which a probe is space charge limited. By comparing the observed emission with these limits we determined that in all the cases the probe is SCL (Table 5.1). Using this same model, we determine the limits with which we can approach the plasma potential (due to rounding in the I-V characteristic—Figure 1.3).

The plasma potential measurement accuracy can be improved by creating a colloid plume with increased droplet density. Using pure EMI-Im (instead of only 2.9% by weight in TBP) would increase the propellant electrical conductivity and therefore the amount of current that would be carried in the plume. The greater charge-to-mass ratio would also create a more densely charged environment, which is more conducive to probe electron extraction. Although the mixed regime is well understood and enables a stable Taylor emission, purely ionic emission regimes are gaining increased attention for propulsion due to increased Isp and overall efficiency. Comparing the plasma potential of mixed regimes, and studying the potential of other propellants such as EMI-BF_4 (purely ionic at room temperature) would be of great relevance.

Alternative PPU and signal conditioning designs could also improve the quality of these studies. Off-the-shelf DC-DC converters, for example, provide a vast array of options for power that could simplify the design of the signal conditioning electronics (e.g. the –9V from the MAX634 would be irrelevant). Also, additional measures could be taken to prevent leakage between the outputs (hi output and the reference lead) in the EMCO

converters. Physical separation among the channels (e.g. not sharing Thruster Common) would also eliminate the possibility of current overlap even at the nanoampere regime. The versatile OP97 op-amp, for example, can be used in high isolation schemes that isolate current within fractions of a nanoampere. Using Kapton-film tape is also critical to cover all high voltage surfaces. For example, the needle current losses due to the gator-style clip used to connect the needle to the PPU output could have been a result of the fact that high voltage surfaces can leak current at atmosphere (especially in humid conditions) when not properly isolated.

Another challenge in these tests was the fluctuating electrospray. This was due in part to the fact that the 304 stainless steel needle, exposed to high voltage and EMI-Im, was likely experiencing some level of propellant decomposition, possibly creating buildup inside the needle. The flowrate was not measured, although this would greatly reduce the uncertainty in some of the supporting analysis. Increasing the resolution of the known pressure drop across the needle (through use of a pressure transducer for example) would reduce the error in the estimates for mass flowrate. Using a micro-valve manifold (e.g. via Upchurch or Swagelok precision flow regulating valves) would also improve the control of the pressure and therefore the flowrate. Additional control could be attained using two off-the-shelf piezoelectric actuators which could be put into a feedback loop to maintain a particular pressure differential between the pressurized propellant reservoir and an external pump.

Once a steady flowrate is established, the needle-extractor voltage difference should be kept constant. We could connect a power supply's positive output to the needle and connect another power supply's negative output to the extractor. The needle output would be used for control. Once a particular voltage difference between the needle and extractor is found, adjustments of the needle voltage will result in a directly proportional change in the extractor voltage, so the needle voltage can be varied significantly while maintaining a stable electrospray.

Future work will extend these results to include the effect of the carbon nanotube field emission cathode. These studies will include the effects of neutralization on the electrospray, in particular the effectiveness of the pulsed neutralization approach[1], as well as the effect of different electron energies and current flux on the plasma potential profile. These tests would be able to take advantage of the PPU's built-in control electronics and isolated thruster common point for the cathode neutralizer.

Additional extended experiments should include those that would significantly improve the density estimates, such as measurements of the stopping potential and time-of-flight. These tests would provide enough additional data for the electrospray under study so that using comparable published data would be unnecessary. These tests would also enable a more precise characterization of the electrospray, which would provide much more information as to what variables influence the electrospray behavior and plume potential. Improved models of plume charging and energy distributions within colloid plumes

would better serve scientists and engineers who wish to take advantage of the versatile colloid thruster.

References

1. Gamero-Cataño, M. and Hruby, V., "Characterization of a Colloid Thruster Performing in the micro-Newton Thrust Range," IEPC-01-282, 27th International Electric Propulsion Conference, October 15-19, 2001, Pasadena, CA.

2. Gamero-Cataño, M. and Hruby, V., "Electrospray as a Source of Nanoparticles for Efficient Colloid Thrusters," AIAA 2000-3265, 36th AIAA Joint Propulsion Conference, July 16-19, 2000, Huntsville, AL.

3. Busek Co., "Colloid Thrusters for Micro and Nano Satellites", NASA/CR—2001 – 210758.

4. Gamero, M., "Slit Colloid Thrusters Using Ionic Liquid Propellants", DoD SBIR FY03.1 Topic OSD 03-008, Proposal No. O031-0146.

5. J.Fernández de la Mora & I.G.Loscertales., "The current emitted by highly conducting Taylor cones" J. Fluid Mech. 260, 155-184 (1994).

6. J. Rossel-Llompart & J. Fernandez de la Mora., "Generation of monodisperse droplets 0.3 to 4 μm in diameter from electrified cone-jets of highly conducting and viscous liquids", J. Aerosol Sci. 25, 1093-1119 (1994).

7. D.R. Chen & D. Pui., "Experimental Investigation of Scaling Laws for Electrospraying: Dielectric Constant Effect", Aerosol Science and Technology. 27, 367-380 (1997).

8. A.M.Gañán-Calvo, J. Dávila, & A. Barrero., "Current and droplet size in the electrospraying of liquids. Scaling laws", J. Aerosol Sci. 28, 249-275 (1997).

9. "Laser Interferometer Space Antenna for the Detection and Observation of Gravitational Waves: Pre-Phase A Report, 2nd edition," MPQ233, LISA Study Team, Max-Plank-Institute für Quantenoptik, pp. 151-157.

10. NASA's JPL website, accessed October 2003. http://lisa.jpl.nasa.gov

11. Marrese-Reading, C., Polk, J., Mueller, J. and Owens, A., "In-FEEP Thruster Ion Beam Neutralization with Thermionic and Field Emission Cathodes,", IEPC-01-290, 27th International Electric Propulsion Conference, October 15-19, 2001, Pasadena, CA.

12. Tajmar, M., "Survey on FEEP Neutralizer Options", AIAA 2002-4243, 38th AIAA Joint Propulsion Conference, July 7-10, 2002, Indianapolis, IN.

13. NASA's Goddards Space Flight Center website, accessed November 2003. http://maxim.gsfc.nasa.gov/

14. Davis, G., Estes, R., Glubke, S. "Micro-Arcsecond Xray Imaging Mission-Pathfinder (MAXIM-PF)-Propulsion", NASA's Goddards Space Flight Center website, accessed November 2003. http://maxim.gsfc.nasa.gov/documents/MAXIM-Documents.html

15. Hutchinson, I., Principles of Plasma Diagnostics, Cambridge University Press, 1987, pp. 78-79

16. Kemp, R. and Sellen, J., "Plasma Potential Measurements by Electron Emissive Probes," Rev. Scientific Instruments, Vol. 37, No. 4, April 1966, pp. 455 – 461.

17. Hershkowitz, N., "How Langmuir Probes Work", Plasma Diagnostics, Academic Press, Inc., 1989, pp. 113-183

18. Gamero-Cataño, M. and Hruby, V., "Electric Measurements of Charged Sprays Emitted by Cone Jets," *J. Fluid Mech*. Vol. 459, 2002, pp. 245-276

19. Schuss, J. and Parker R., "Behavior of electron-emitting plasma probes in the space-charge-limited regime", J. Applied Physics, Vol. 45, No. 11, 1974

20. Shea, M., Leland, M., Schrift,T.; "Development of a Time-of-Flight Spectrometer to Measure MicroNewton Thruster Performance"; MQP JB3-9486

21. Lozano, P., Martinez-Sanchez, M., "The Effect of Using Finite-Width Electrostatic Gates in Time-of-Flight Measurements for Colloid Thrusters", IEPC-01-286, 27th International Electric Propulsion Conference, October 15-19, 2001, Pasadena, CA.

22. Gamero-Cataño, M., Hruby, V., "Characterization of Electrosprays and Its Relevance to Colloid Thrusters" IEPC-01-283, 27th International Electric Propulsion Conference, October 15-19, 2001, Pasadena, CA.

23. Gamero-Cataño, M., Hruby, V., "Electrospray as a Source of Nanoparticles for Efficient Colloid Thrusters", J. Propulsion and Power, Vol. 17, No. 5, 2001

24. Martel, R., et al, "Single and multi-wall carbon nanotube field-effect transistors", Applied Physics Letters, Vol. 3, No. 26, 1998

25. Lee,S-B, et al, "Fabrication of Carbon Nanotube Lateral Field Emitters", Institute of Physics Publishing, Nanotechnology 14, 2003

26. Chen, F.F., Plasma Physics and Controlled Fusion Volume 1: Plasma Physics, Plenum Press, 1984.

27. Blandino, J., Roy, T., Sartorelli, R., and Gamero-Cataño,M., "Measurements of Plasma Potential in Colloid Thruster Plumes", AIAA 2003-4849, 39th AIAA Joint Propulsion Conference, July 21-23, 2003, Huntsville, AL.

28. Related by Manuel Gamero in a conversation at Busek Co, Inc in October 2003.

29. Hruby, V., Gamero-Cataño, M., Falkos, P., and Shenoy, S., "Micro Newton Colloid Thruster System Development," IEPC-01-281, 27th International Electric Propulsion Conference, October 15-19, 2001, Pasadena, CA.

30. Fox, R., McDonald, A., Introduction to Fluid Mechanics, 5th ed. John Wiley & Sons, Inc, 1998.

Appendices

Appendix A: Mechanical Drawings (Pro/E) of Delrin Adaptor assembly for Colloid Thurster and Neutralizer Housing

Appendix B: Electrical schematic of Power Processing Unit

Appendix C: Original equipment manufacturer's listing of factory-calibrated accuracies and resolutions for the Keithly 6514 electromer, the Fluke 83-III digital multimeter and the National Instruments 6025E data acquisition card.

Appendix D: Matlab code used to solve non-dimensional Poisson-based equation which calculates probe emission strength for a given density and plasma potential.

Appendix A

Mechanical drawings of adaptor flange hardware. All drawings made with Pro/E 2001.

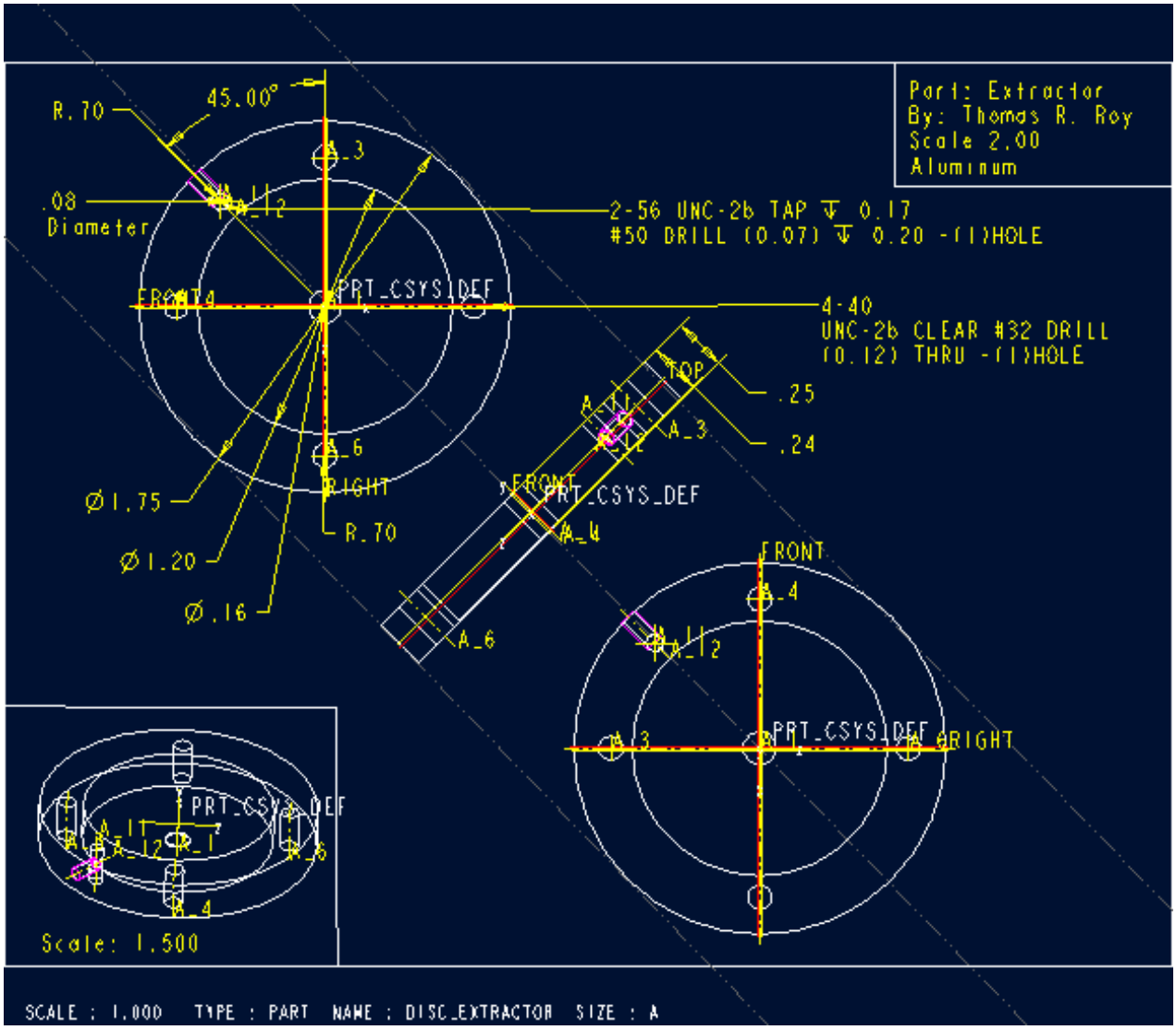

Figure A.1: The extractor was made of aluminum. This representation is not to the reported scale.

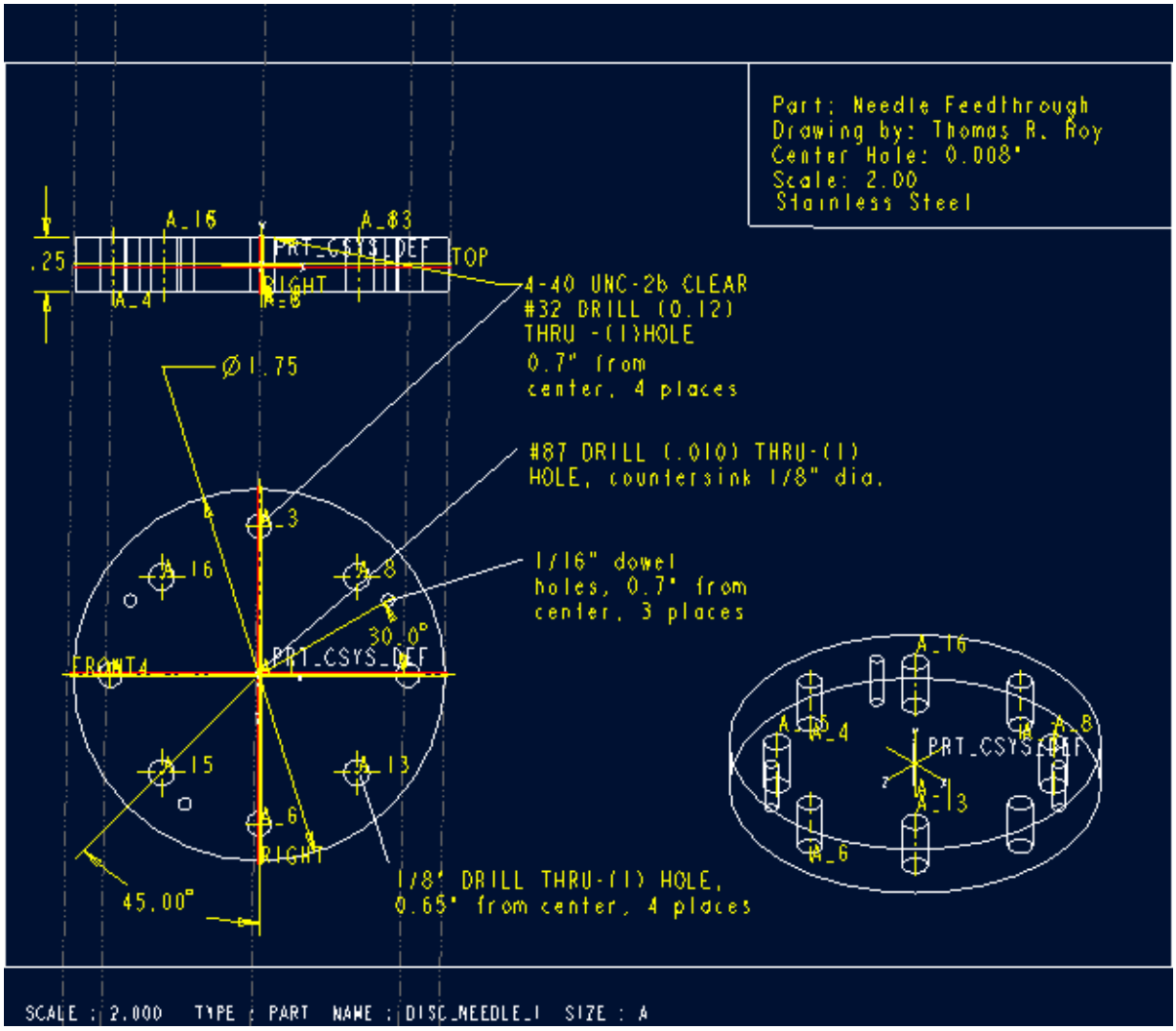

Figure A.2: This needle housing was originally going to be stainless steel for the purpose of conducting current to the needle tip, however it was later determined that Delrin plastic would isolate the needle while providing mechanical support: the current was applied externally to the needle. This representation is not to the reported scale.

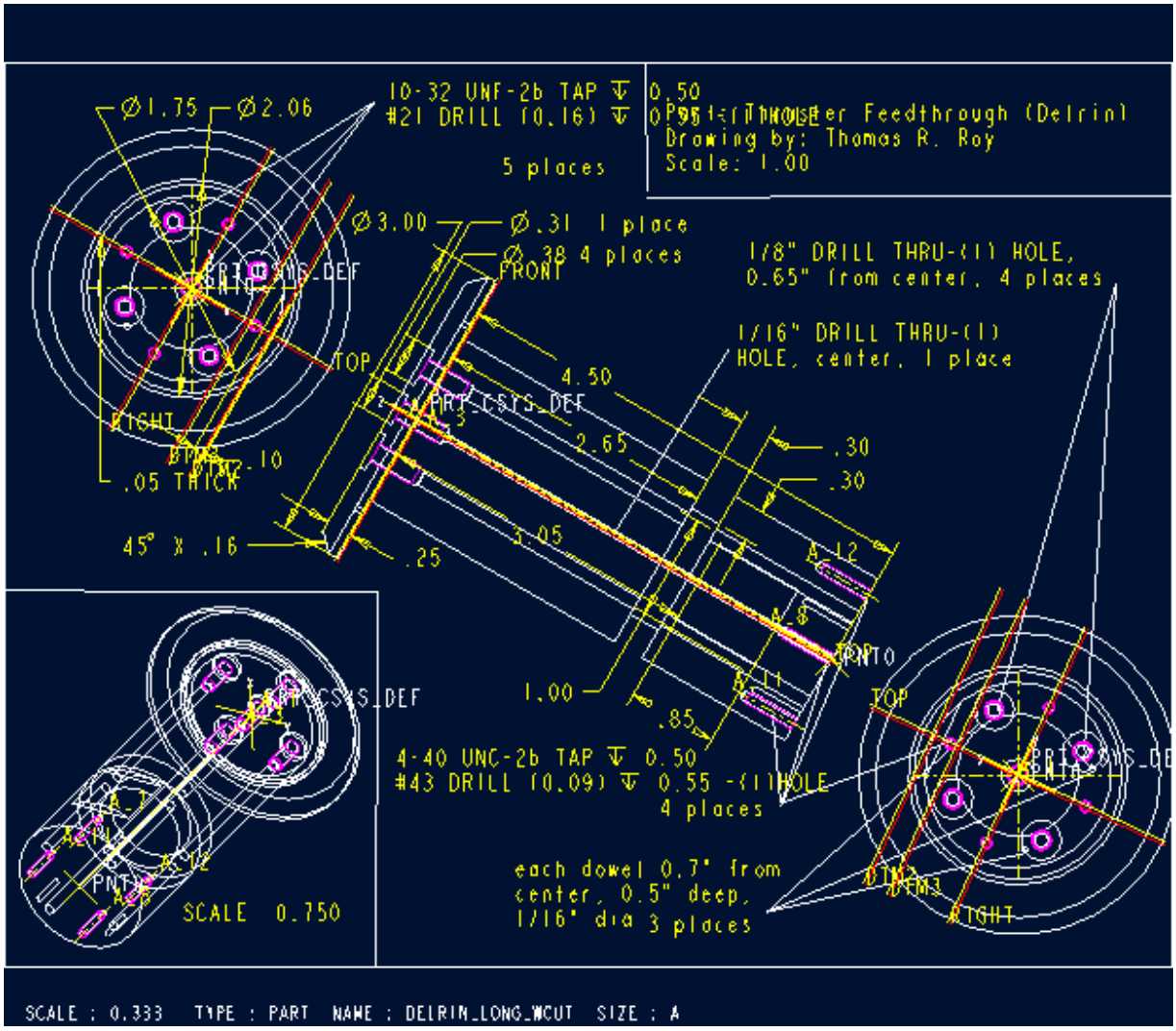

Figure A.3: This piece was machined from 3” dia. Delrin stock. It features a convenient mounting space for the cathode neutralizer, as well as external feedthroughs for the needle, CNT cathode, cathode gate, extractor and decelerator electrode. This representation is not to the reported scale.

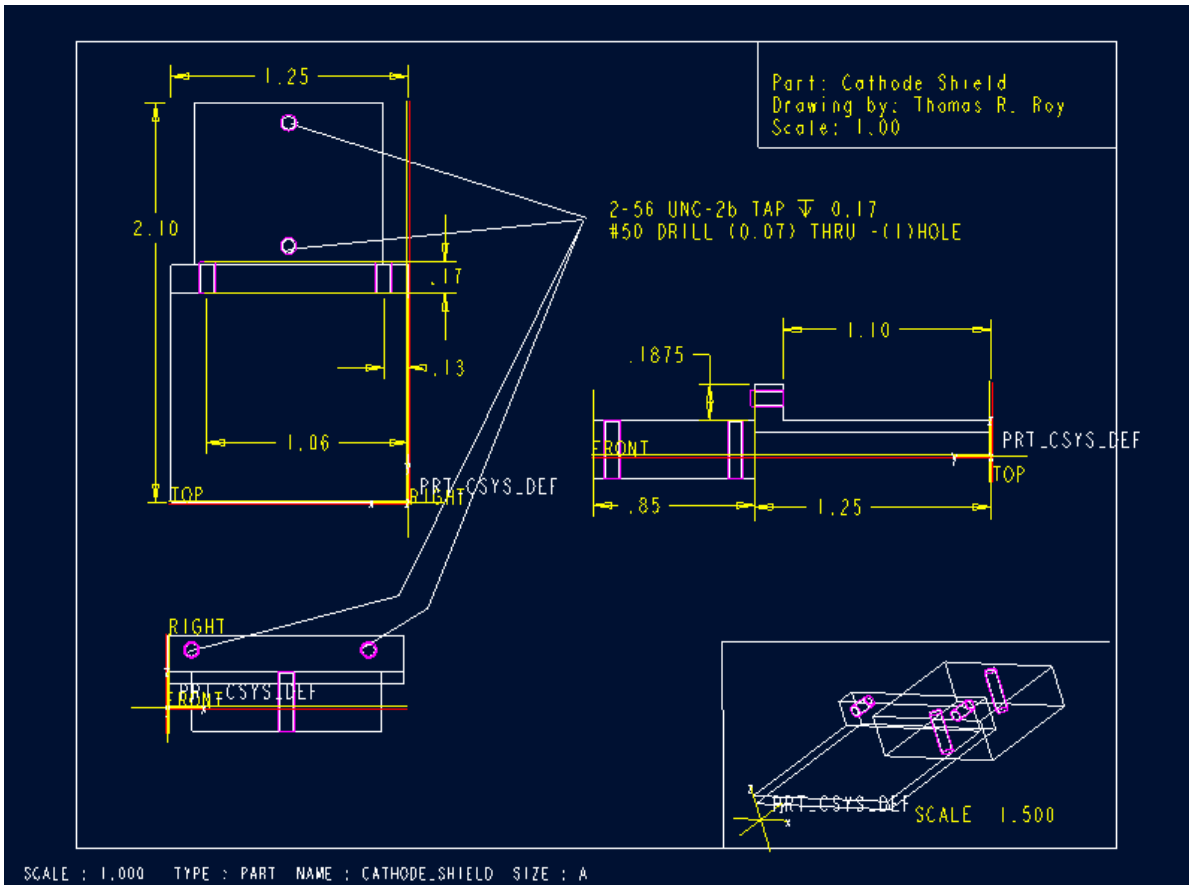

Figure A.4: The cathode shield fits into the end flat-plate of the long Delrin adaptor. The other end of the shield supports the cathode neutralizer, which uses 2 #2-56 screws to firmly affix the neutralizer. This representation is not to the reported scale.

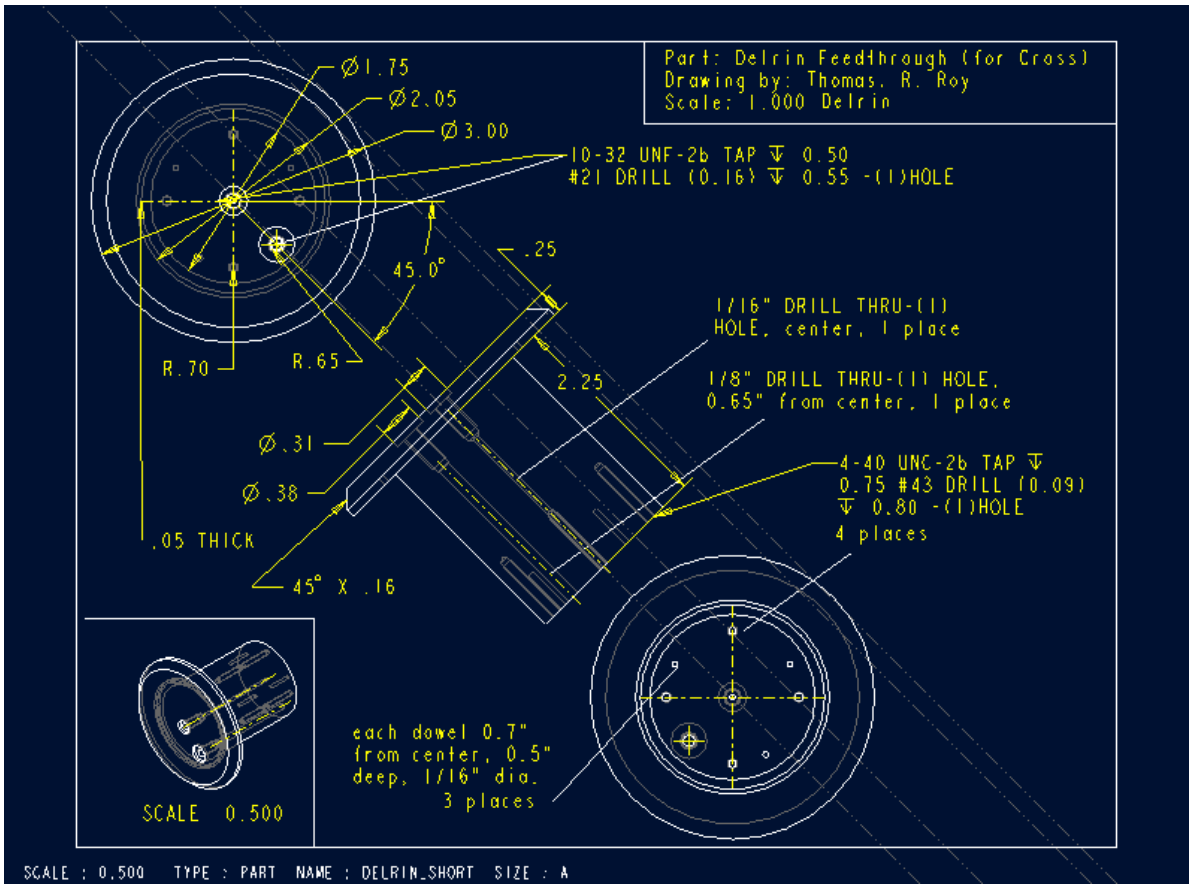

Figure A.5: For the purpose of learning to use the electrospray, and monitoring under what conditions the spray operates (via a camera). This representation is not to the reported scale.

Appendix B

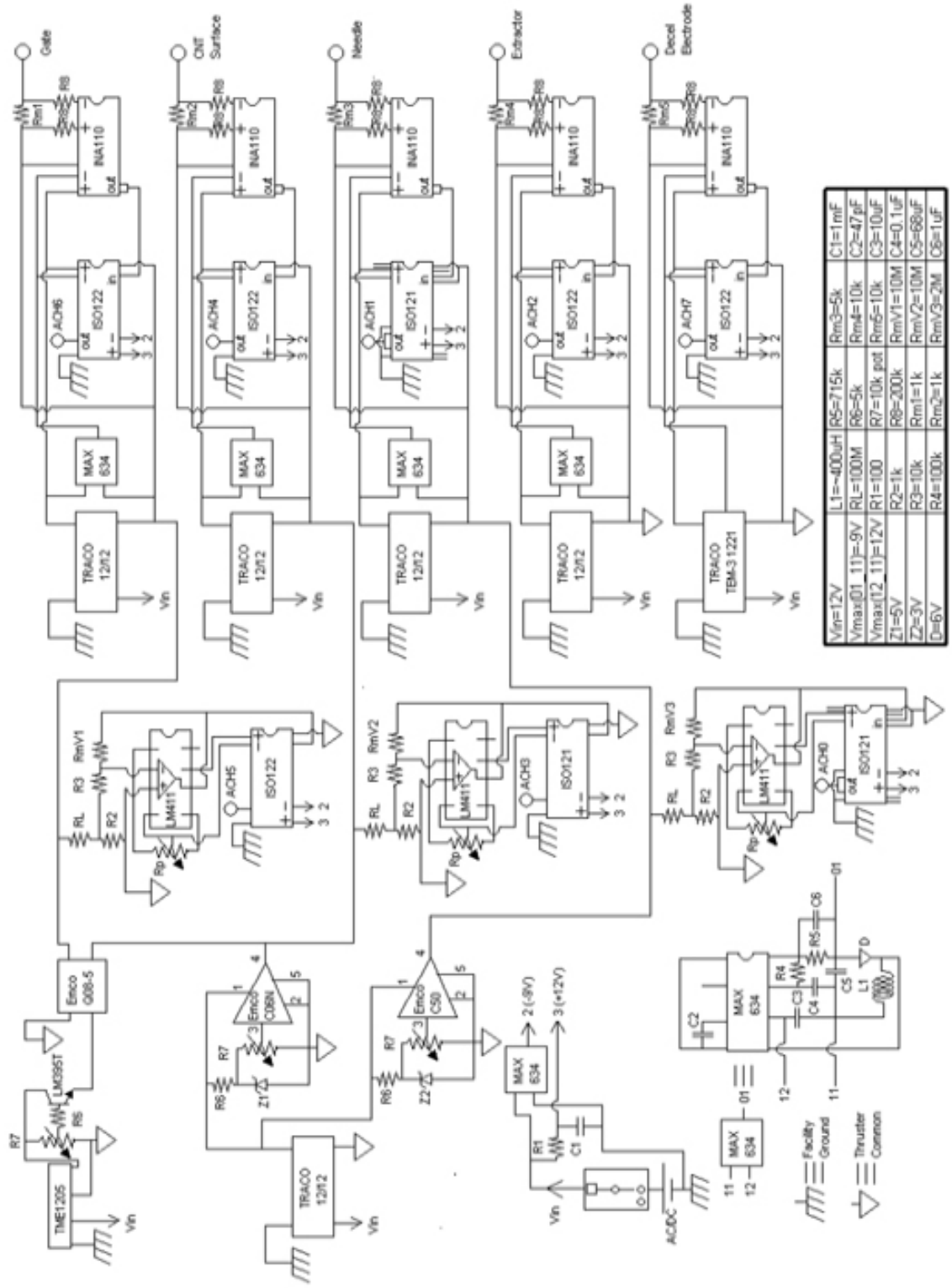

Figure B.1: PPU Electrical Diagram

Appendix C

Some voltage, current and resistance measurements were made by the NIST (National Institute of Standards and Technology)-Certified Fluke Digital Multimeter (Model 83III), as well as the Keithly Electrometer (Model 6514). The range, accuracy and resolution for each measurement of these two devices is summarized in Appendix C.1. This data has been taken directly from the manufacturer's specifications, and it is based on the factory calibration, as no additional calibrations were made on the equipment.

Table C.1: Range, Resolution and Accuracy of the Keithly 6514 Electrometer and Fluke 83III Digital Multimeter.

Measurement	Range	Resolution	Accuracy (±%display value + counts)
Keithly 6514-Volts	2V	10uV	0.025 + 4
Keithly 6514-Volts	20V	100uV	0.025 + 3
Keithly 6514-Volts	200V	1mV	0.06 + 3
Keithly 6514-Amps	20pA	100aA	1 + 30
Keithly 6514-Amps	200pA	1fA	1 + 5
Keithly 6514-Amps	2nA	10fA	0.2 + 30
Keithly 6514-Amps	20nA	100fA	0.2 + 5
Keithly 6514-Amps	200nA	1pA	0.2 + 5
Keithly 6514-Amps	2uA	10pA	0.1 + 5
Keithly 6514-Amps	20uA	100pA	0.1 + 5
Keithly 6514-Amps	200uA	1nA	0.1 + 5
Keithly 6514-Amps	2mA	10nA	0.1 + 10
Keithly 6514-Amps	20mA	100nA	0.1 + 5
Keithly 6514-Ohms	2k	10m	0.20 + 10
Keithly 6514-Ohms	20k	100m	0.15 + 3
Keithly 6514-Ohms	200k	1	0.25 + 3
Keithly 6514-Ohms	2M	10	0.25 + 4
Keithly 6514-Ohms	20M	100	0.25 + 3
Keithly 6514-Ohms	200M	1k	0.30 + 3
Keithly 6514-Ohms	2G	10k	1.5 + 4
Keithly 6514-Ohms	20G	100k	1.5 + 3
Keithly 6514-Ohms	200G	1M	1.5 + 3
Fluke 83III-Volts	4mV-1kV	0.1mV max	0.10%
Fluke 83III-Amps	40uA-10A	0.01uA max	0.40%
Fluke 83III-Ohms	40 - 400M	0.1 max	0.40%

The National Instruments Data Acquisition card (Model 6025E) was used to record analog input from each of the telemetry channels during most of the testing. Each of the channels was used in the RSE (Referenced Single Ended) mode. The accuracy of this device can be seen in Appendix C.2. All of the measurements made were in the +/-10V range. Also, the averaged numbers assume dithering and averaging of 100 single-channel readings. This data has been taken directly from the manufacturer's specifications.

Table C.2: Range and accuracy of National Instruments 12-bit E-Series Data Acquisition card.

Range (V)	Offset (mV)	Accuracy (mV)
±10	6.38	4.88
±5	3.20	2.33
±0.5	0.340	0.244
±0.05	0.054	0.024

Appendix D

Matlab code to numerically solve and plot Equation 4.12, authored by Professor J. Blandino.

Scl_onset5.m

```
%   SCL electron emission model (Ref: Kemp & Sellen, Rev. Sci. Inst.
Vol 37, No 4, April 1966)

clear all
global A B C x0 grad_limit
%   Physical and Numerical solution Constants
%note at 10^7, t_final=500, t_check=450
%when density decreases go out further.

k        =   1.381e-23   ;   % J/K
e        =   1.602e-19   ;   % C
me       =   9.109e-31   ;   % kg
eps0     =   8.85e-12    ;   % C/V/m
tstep    =   0.1         ;   % integration step (non-dim position)
t_final =   25000        ;    % max non-dim radial dist for integration
t_check =   24000       ;   % radial position used to check field
gradient
grad_limit  =  0.01     ;   % limit applied to electric field
iter_control = 1        ;   % = 1 for iteration on or = 0 for no
iteration
itermax =   50          ;   % max number of iterations
%   Probe and experiment parameters
n0_cm    =   1e4      ;   % ion density, cm^-3
Tw       =   2500     ;   % wire temperature,  K
Te       =   2500     ;   % electron Temp, K
r0_cm    =   3.81e-3 ;   % wire radius, cm
il       =   0.4      ;   % emission strength, A/m (used when iteration
loop is bypassed (iter_control =0)
x0       =   40       ;   % non-dim plasma potential
%
%   Derived parameters
%
r0       =   r0_cm/100                   ;   % wire radius, m
n0       =   n0_cm*1e6                   ;   % ion density, m^-3
ve       =   sqrt(k*Tw/me)               ;   % electron thermal
velocity, m/s
rho_0    =   e*n0                        ;   % ion charge density, C/m^3
A        =   il/(rho_0*2*pi*r0*ve)       ;   % non-dim emission strength
parameter
B        =   Tw/Te                       ;   % wire-electron temp ratio
C        =   e*rho_0*r0^2/(k*Tw*eps0)    ;   % non-dim ion density
parameter
%
    iter = 0 ;
    il_hi=0.01;
    il_lo=0.000001;
    event_time=0;
    stopflag=0;
%
while event_time < t_check & iter < itermax & stopflag == 0
%
```

```
    clear te ye ie
    iter=iter+1
    event_time
    if iter_control == 1
        ilguess=(il_hi+il_lo)/2
    else
        ilguess=il;
        iter=itermax;
    end
    A       =   ilguess/(rho_0*2*pi*r0*ve)       ;   % non-dim emission
strength parameter
%
%  Set-up the parameters for ode45 call
options=odeset('Events',@eventinfo);
tspan = [1 : tstep: t_final];
%  Integrate Poission Eq.
[t, Pot_dist,te,ye,ie] = ode45(@poisson_limit,tspan, [0,0] ,options);
%
    if size(ye) ~= 0
        if ye(1,2) > 0
           il_hi=ilguess;
        else
           il_lo=ilguess;
        end
        event_time=te;
    else
        stopflag=1
    end
end
%  Plotting nondimensional sheath profile
%
% Display Results at end of run:
%
event_time_at_completion=event_time
final_il=ilguess
%
figure(1)
plot(t,Pot_dist(:,1))
title('Non Dimensional Sheath Profile')
xlabel('Nondimensional Radial position');
ylabel('Nondimensional Potential');
grid on
%
figure(2)
plot(t,Pot_dist(:,2))
title('Non Dimensional Electric Field')
xlabel('Nondimensional Radial position');
ylabel('Nondimensional Potential Gradient');
grid on
```

EVENTIFO.M

```
%-----------------------------------------------------------
function [value, isterminal, direction]=eventinfo(time,y)
global A B C x0 grad_limit
%

value=abs(y(2,1))-grad_limit;
isterminal=1;
direction=0;
```

poisson_limit.m

```
%  OUTPUTS:
%  xdot  - the gradient of the state (a 2 x 1 vector)
function xdot=poisson_limit(t,x)
global A B C x0 grad_limit
%
%**************** Gradient of State Vector
*****************************************
    xdot =  [x(2);-(1/t)*x(2)-C*(1-exp(-B*(x0-x(1)))-
A/(t*sqrt(2*x(1)+1)))];
%
```

Appendix E

Maple v.6 code used to estimate electrospray density.

T.R.Roy, October 15, 2003

Reference: "Electric measurements of charged sprays emitted by cone-jets", *J.Fluid Mech (2002) vol. 459 pp. 245-276*

Calc03_TBP1.mws, flowrate of 1.16 x 10^(-12) **and I=54nA, which is the closest approximation to experimental values.**

```
> restart;
```

Determine mass flowrate of main (1) and satellite (2) droplets.

```
> In:=54*10^(-9):
> density:=976:
> q1m1:=43.8:
> q2m2:=228.3:
> mdt:=(1.16)*10^(-12)*density:
> f1:=(mdt-md2)*q1m1 + md2*q2m2=In:
> m2_d:=solve (f1, md2);
```

$$m2\_d := .2390998374\ 10^{-10}$$

```
> m1_d:=+mdt-m2_d;
```

$$m1\_d := .1108250016\ 10^{-8}$$

```
> mt_d:=m1_d+m2_d;
```

$$mt\_d := .1132160000\ 10^{-8}$$

Determine Velocities of main (1) and satellite (2) droplets.

```
> Vo:=1469:
> Vs1:=52:
> Vs2:=493:
> v1:=sqrt(q1m1*2*(Vo-Vs1));
```

$$v1 := 352.3197411$$

```
> v2:=sqrt(q2m2*2*(Vo-Vs2));
```

$$v2 := 667.5639295$$

Determine area

```
> Dist:=0.0525:
> theta:=30:
> rc:=Dist*tan(30*3.14159/180);
```

$$rc := .03031085817$$

```
> Area:=3.14159*rc^2;
```

$$Area := .002886329916$$

Determine particle mass

```
> surf_tension:=0.028:
> en:=8.85*10^(-12):
```

```
> Dd:=
((6*0.7*sqrt(8*surf_tension*en))/(q1m1*density))^(2/3);
```

$$Dd := .2674734448\ 10^{-6}$$

```
> qm:=0.7*3.14159*sqrt(8*surf_tension*en*Dd*Dd*Dd);
```

$$qm := .4283159002\ 10^{-15}$$

```
> q_m:=43.8:
> m:=qm/q_m;
```

$$m := .9778901831\ 10^{-17}$$

Calculate density of main droplet (note--value is per cubic meter)

```
> n1:=m1_d/(m*v1*Area);
```

$$n1 := .1114460579\ 10^{9}$$

Calculate characteristic length

```
> Lcn1:=n1^(-1/3);
```

$$Lcn1 := .002077997862$$

Calculate distance ("r_red") from charge where potential is reduced by "fract" of 90%

```
> fract:=(Vr - Vsurf)/(Vsurf)=rn/r - 1;
```

$$fract := \frac{Vr - Vsurf}{Vsurf} = \frac{rn}{r} - 1$$

```
> fract:=-0.9:
> rn:=Dd/2:
> r:=Lcn1:
> fract:=rn/r-1;
```

$$fract := -.9999356415$$

```
>
```